공학박사 학위논문

Evaluation of through-thickness distributing residual stress using instrumented indentation test

연속압입시험을 활용한 깊이에 따른 잔류응력 분포 평가

2022 년 2 월

서울대학교 대학원

재료공학부

이 준 상

Evaluation of through-thickness distributing residual stress using instrumented indentation test

연속압입시험을 활용한 깊이에 따른 잔류응력 분포 평가

지도 교수: 권 동 일

이 논문을 공학박사 학위논문으로 제출함

2022 년 2 월

서울대학교 대학원

재료공학부

이 준 상

이준상의 공학박사 학위논문을 인준함

2022 년 2 월

위 원 장 한 홍 남 (인)

부위원장 권 동 일 (인)

위 원 이 명 규 (인)

위 원 김 종 성 (인)

위 원 정 재 석 (인)

Evaluation of through-thickness distributing residual stress using instrumented indentation test

A DISSERTATION SUBMITTED TO
DEPARTMENT OF MATERIALS SCIENCE AND ENGINEERING
SEOUL NATIONAL UNIVERSITY

FOR THE DEGREE OF
DOCTOR OF PHILOSOPHY

JUNSANG LEE

February 2022

Abstract

Junsang Lee
Dept. Materials Science and Engineering
The Graduate School
Seoul National University

Residual stress, a locked-in stress in material, is generated through non-uniform plastic deformation, surface modification and changes in phase and microstructure of materials. The elastic range stress is critical factor influencing the structural integrity of component which can lead to unexpected deformation and cracking. The stress varies the field of stress and strain near the crack tip taking a role as additional loads widening the crack. Tensile residual stress decreases the crack resistance against fracture and fatigue, and the stress combined with corrosive environment can result in stress corrosion cracking for some materials. Various processing methods for applying compressive residual stress, which can beneficial to prevent the crack opening, have been researched including the process of surface modification and welding with special materials. However, limited number of stress measurement methods are applied for profiling the through-thickness residual stress based on stress relaxation or layer removing, which yields non-negligible

damages on testing components.

Instrumented indentation testing is technique specialized for measuring the local mechanical properties. Surface residual stress can be evaluated by analyzing the variation of indentation curves in terms of force difference at the maximum indentation displacement comparing to the indentation for the zero-stress state, remaining minimal imprints. Indentation researches regarding residual stress has been restricted to evaluate the magnitude, directionality and principal direction of residual stress, rather than stress profiling though the depth of material. Furthermore, few studies identifying the depth corresponding to the location of evaluated indentation residual stress have been carried out.

In this study, through-thickness residual stress evaluation model by using conical indentation was proposed. The stress sensing depth, the maximum depth of stress that is influential to the indentation curve, was estimated by finite element analysis. The contributions of stress at specific depth on total force difference, defined as calibration coefficients, were calculated from force differences with increasing the stressed depth. Theoretical model to profile the stress by depth was proposed based on the geometrical self-similarity of sharp indenter. The accuracy of evaluated stress was improved in consideration of the material dependency on the conventional indentation model. Stress

sensing depth of indentation, which varies with materials, was observed to correspond to the depth of plastic zone. Estimation of plastic zone depth with mechanical properties of material was carried out by dimensional analysis. Computational and experimental verifications were performed for various material properties for non-uniform stress distribution through the thickness. The verification results were matched well with reference stress distributions.

Keyword: Residual stress; Through-thickness residual stress; Instrumented indentation test; Conical indentation; Finite element analysis; Mechanical properties; Dimensional analysis

Student Number: 2015-20857

Table of Contents

Abstract .... **i**

Table of contents .... **iv**

List of tables .... **vii**

List of figures .... **ix**

Chapter 1. Introduction **1**

1.1 Objective of the Thesis 2

1.2 Organization of the Thesis 8

References 9

Chapter 2. Research Background **12**

2.1 Residual stress 13

2.1.1 Origins of residual stress 13

2.1.2 Effect of residual stress on materials 14

2.2 Residual stress evaluation methods 16

2.2.1 Destructive methods 16

2.2.2 Non-destructive methods 22

2.3 Indentation methods 25

2.4 Limitations of previous methods 35

References 49

Chapter 3. Theoritical modeling 57

3.1 Motivation and research flow 58

3.1.1 Introduction 58

3.1.2 FEA simulation approach 61

3.2 Phenomenological Modeling 64

3.2.1 Maximum stress sensing depth 64

3.2.2 Calibration coefficient 68

3.3 Evaluation of through-thickness residual stress 71

3.3.1 Theoretical modeling 71

3.3.2 Computational verifications 75

3.3.3 Discussion 76

References 101

Chapter 4. Improvement of theoretical model 103

4.1 Introduction 104

4.2 Modification of IIT stress evaluation model 108

4.1.1 Stress sensitivity of indentation curve 108

4.1.2 Dimensional analysis 110

4.3 Optimization of calibration coefficient 113

4.3.1 Stress sensing depth 113

4.3.2 Dimensional analysis 115

4.4 Computational verification 117

References 144

Chapter 5. Experimental vericiation 146

5.1 Materials and methods 147

5.2 Results and discussion 152

5.2.1 Applied stress by four-point bending 152

5.2.2 Peening residual stress 153

5.3 Issues and limitations 154

References 166

Chapter 6. Conclusion 167

Abstract (in Korean) 170

LIST OF TABLES

Table 3-1. Cumulative coefficient of reference material (E=200 GPa, σ_Y/E=0.003, n=0.3, υ=0.3)

Table 3-2. Calibration coefficient of reference material (E=200 GPa, σ_Y/E=0.003, n=0.3, υ=0.3)

Table 3-3. Applied stress profile for computational verification

Table 4-1. Mechanical properties of materials and stress level applied to FEA simulations

Table 4-2. Correction slopes (S_T) by mechanical properties

Table 4-3. Correction slopes (S_C) by mechanical properties

Table 4-4. Fitting coefficients for considering mechanical property effect

Table 4-5. Fitting coefficients for considering mechanical property effect

Table 4-6. Correction slopes (S_T) by mechanical properties

Table 4-7. Correction slopes (S_T) by mechanical properties

Table 4-8. Fitting coefficients for considering mechanical property effect

Table 4-9. Generalized cumulative coefficient of reference

Table 4-10. Generalized calibration coefficient

Table 5-1 Tensile properties of materials for verification test

LIST OF FIGURES

Chapter 2

Figure 2.1. Schematic diagram of the residual stress distribution of toughened glass sheet comparing with external load

Figure 2.2. Effect of residual stress on components

Figure 2.3. Residual stress measurement methods

Figure 2.4. Calibration coefficient of hole-drilling method

Figure 2.5. Sequential cutting process of sectioning method

Figure 2.6. Principle of stress evaluation using contour method

Figure 2.7. Schematic diagram of indentation force-displacement curve

Figure 2.8. Variation of indentation contact depth with estimation methods

Figure 2.9. Variation of indentation curve of API X65 with stress

Figure 2.10. Schematic loading curves of Knoop indentations for non-equibiaxial stress state

Figure 2.11. Conversion factors ratio with indentation displacement

Fig. 2.12. Directional in-plane displacements by the conical indentation

Chapter 3

Figure 3.1. 2-D conical indentation simulation using ABAQUS

Figure 3.2. Comparison of indentation curves obtained from experiment and FEA simulation for STS304 steel

Figure 3.3. Example of step-wise constant stress distribution by controlling boundary conditions and thermal expansion coefficient (a) stress applied by heating (b) stress applied by cooling (c) stress distribution of (a) and (b)

Figure 3.4. Comparison of indentation curves with variation of stress applied by mechanical and thermal methods (a) Full-loading curve (b) Enlarged image of (a) around the maximum indentation force

Figure 3.5. Schematic diagram of indentation simulations with increasing stressed depth at fixed maximum displacement

Figure 3.6. Expected variation of indentation curves with increasing stressed depth

Figure 3.7. Schematic diagram of cumulative $\Delta F - h_{stressed}$ curve

Figure 3.8. Saturation of force difference with increasing the depth of step-wise constant stress (a) Indentation with increasing stressed depth using FEA (b) $\Delta F - h_{stressed}$ obtained from FEA

Figure 3.9. Identical ratio of stress depth to indentation displacement based on geometrical self-similarity of sharp indenter

Figure 3.10. Identical layer contribution of force difference based on geometrical self-similarity of sharp indenter, when blue and gray indicate stressed and stress-free states

Figure 3.11. Schematic diagram of normalization process for cumulative ΔF - $h_{stressed}$ curve obtained at different indentation displacements

Figure 3.12. Normalization process for cumulative ΔF - $h_{stressed}$ curve obtained at ten different indentation displacements using FEA

Figure 3.13. Definition of the force differences generated by layer stress and cumulative stress when blue and gray indicate stressed and stress-free states

Figure 3.14. Schematic diagram of performed simulations to verify the force difference independency on the other layer stress

Figure 3.15. Comparison of stress contribution obtained from cumulative stressed depth and the contribution from single stressed depth indentation

Figure 3.16. Indentation test for non-uniform stress state (a) Force differences by indentation displacements (b) Contribution of layer stresses on the force differences

Figure 3.17. Computational verification results of reference material for (a) profile #1, (b) profile #2 (E=200 GPa, σ_Y/E=0.003, n=0.3, υ=0.3)

Figure 3.18. S Computational verification results of reference material for

(a) profile #1, (b) profile #2 (E=200 GPa, σ_Y/E=0.003, n=0.2, υ=0.3)

Figure 3.19. Computational verification results of C1220 for (a) profile #1, (b) profile #2 (E=105 GPa, σ_Y/E=0.002, n=0.06, υ=0.34)

Figure 3.20. Computational verification results of S420J2 for (a) profile #1, (b) profile #2 (E=209 GPa, σ_Y/E=0.0022, n=0.15, υ=0.275)

Chapter 4

Figure 4.1. Change in indentation hardness depending on the residual stress

Figure 4.2. Change in peak load of spherical indentation depending on residual stress

Figure 4.3. Mechanical property dependency of estimated IIT stress using Lee and Kwon's model

Figure 4.4. Indentation curves from FEA with different stress for the material of $\mathrm{E} = 200\,\mathrm{GPa}$, $\varepsilon_y = 0.0018$, $\nu = 0.3$, $n = 0.05$, inset is enlarged figure around the maximum indentation displacement

Figure 4.5. Transitional trend of estimated stress by Lee and Kwon's model with applied stress depending on the sign of stress

Figure 4.6. Comparison of stress sensitivity on estimated indentation stress with applied stress by change in yield strain

Figure 4.7. Comparison of stress sensitivity on estimated indentation stress with applied stress by change in strain hardening exponent

Figure 4.8. Comparison of stress sensitivity on estimated indentation stress with applied stress by change in Poisson's ratio

Figure 4.9. Comparison of estimated indentation stress normalized by yield strength with applied stress for the materials in Table 4.1

Figure 4.10. Linear relation between estimated indentation stress and applied stress normalized by yield strength for (a) tensile residual stress state (b) compressive residual stress state

Figure 4.11. Correction slope function of strain hardening exponent (a) tensile residual stress (b) compressive residual stress state

Figure 4.12. Fitting coefficients function of yield strain (a) coefficients a (b) coefficients b

Figure 4.13. Comparison of corrected indentation stress and applied stress normalized by yield strength

Figure 4.14. Variation of cumulative $\Delta F/\Delta F_{max}$-$h_{stressed}/h_{max}$ curve with (a) yield strain and (b)strain hardening exponent

Figure 4.15. Comparison of plastic zone depth and the maximum stress sensing depth when the indentation displacement is 100 μm

Figure 4.16. $\Delta F/\Delta F_{max}$-$h_{stressed}/h_{max}$ curves of various materials normalized by plastic zone depth

Figure 4.17. Plastic zone depth function of strain hardening exponent

Figure 4.18. Fitting coefficients function of yield strain for (a) a (b) b

Figure 4.19. Computational verification results of C1220 for (a) profile #1, (b) profile #2

Figure 4.20. Computational verification results of S420J2 for (a) profile #1, (b) profile #2

Chapter 5

Figure 5.1 Picture of four-point bending jig for generating through-thickness residual stress distribution

Figure 5.2 Simulated through-thickness stress distribution by four-point bending of 4 mm C1220

Figure 5.3 Through-thickness stress distribution with distance normalized by thickness of specimen

Figure 5.4 Flow chart of through-thickness residual stress evaluation

Figure 5.5 Comparison of bending stress measured by IIT and FEA for C1220 specimen with thickness of (a) 3 mm (b) 4 mm

Figure 5.6 Comparison of bending stress measured by IIT and FEA for S420J2 specimen with thickness of (a) 3 mm (b) 4 mm

Figure 5.7 SEM image of conical indenter tip used for verification test

Figure 5.8 Figure. 5.8 Comparison of peening stress distribution measured by hole-drilling, XRD and indentation methods for (a) SUS303 and (b) SUS316

Chapter 1

INTRODUCTION

Contents

1.1. Objective of the Thesis 2

1.2. Organization of the Thesis 8

References 9

1.1. Objective of the Thesis

Residual stresses are an internally locked-in stresses remaining in materials regardless of the external sources of load or stress [1]. The stresses existing in materials are developed to maintain the dimensional continuity in response to incompatible local strain, which is created by many different cause of formation [2]. Residual stress is an inevitable and can be critical for integrity of component issue regardless of scale, when manufacturing process involved. Estimation of structural integrity and reliability of components could be significantly distorted depending on the states of the residual stress. Materials with high level of tensile residual stress, such as welding zone, show degraded performances in terms of fracture toughness, fatigue life and stress corrosion cracking resistance [3-6]. Therefore, the novel manufacturing or surface modification process for reducing harmful tensile residual stress, by controlling the phase transformation temperature of materials [7, 8] or applying compressive residual stress through peening process [9-11], have been developed.

Many kinds of residual stress measurement methods have been developed with specialized characteristics and limitations, such as low damage to specimen, near surface/deep interior measurement, high field applicability and available for complex geometry [2, 6, 12]. Principles of the methods for evaluating residual stress could be broadly classified into three main categories; relaxation measurement methods, diffraction methods and the others. The first group is relaxation measurement methods based on the strain elastically recovered resulting from breaking the continuity by material removals, for examples, hole drilling method, sectioning method, slitting method and contour method [12-18]. The methods measure the strain by strain gauge, air probe or laser scanner, and convert the strain into stress in combination with elastic mechanical properties. The second group is diffraction methods measuring the distance between the atomic planes in crystal structure using X-ray, synchrotron X-ray, neutron diffraction method [19-21]. The relative changes in the atomic plane distance for the stress state comparing with zero stress state determines the strain, and the strain gives stress in the same way as relaxation measurement methods. Diffraction methods possibly utilized non-destructively, if appropriate datum of zero stress reference to compare with is obtainable. There are other methods not included in relaxation measurement nor diffraction methods, such as, methods using magnetic Barkhousen noise, ultrasonic wave and instrumented indentation test. Each method measures different factors; magnetic Barkhousen noise signal, wave velocity and force-displacement curve, respectively, and quantifies the residual stress by using the changes in the factors obtained from stressed state and zero-stress state.

Instrumented Indentation Testing (IIT) measures force and displacement continuously while metallic or diamond indenter penetrates into the material from the surface. The force-displacement curves are utilized as clues to estimate the local mechanical properties of materials by many researchers, such as tensile properties and fracture toughness. The indentation curve also varies with the stress state of materials. Tsui et al. experimentally showed the effect of applied stress on projected morphology and indentation properties such as stiffness, elastic modulus and hardness [22], and Bolshakov et al. provided the changes in indentation F-d curve, indentation properties and plastic zone with stress through finite element simulations [23]. Many researchers developed models evaluating the residual stress by analyzing the variation of indentation curve and projected area [24-28]. Lee and Kwon [28-32] proposed a model to estimate the biaxial stress using projected area of indentation and the force difference at the maximum indentation displacement measured by comparing indentation curves obtained from zero-stress and stressed state. The model related the stress, calculated from force difference divided by projected area, with the indenting directional component of deviatoric stress, when the surface residual is decomposed into hydrostatic and deviatoric stress in stress tensor notation.

Evaluation of through-thickness distributing residual stress with the relaxation measurement methods is performed by stepwise destructive procedure. For example, hole-drilling and slitting remove the materials from the surface of specimen incrementally and measures the intermediate strains continuously [13, 14, 18]. Accompanying the layer removal technique with X-ray diffraction method, which is originally restricted to measure the superficial stress due to the shallow penetration depth; tens of μm from the surface, facilitates the evaluation of through-thickness residual stress [33]. The stresses within the depth where the material is removed are not perfectly relaxed, partial amount of stress is released with sequential removing steps. The stress released more and more as the materials below the depth of stress are removed as the constraints hinder the elastic recovery is eliminated. Therefore, the calibration coefficient to correlate the measured strain at the surface and partially released stress with increasing removed depth shall be identified previously. These methods are inevitable to form a damage not less than the depth of profiled stress on the specimen, which could exceed the allowable flaw size for the in-operating component depending on industrial fields. Synchrotron [20] and neutron diffraction methods [34] having much deeper penetration depth using high beam intensity than X-ray, up to tens of mm from surface, are known as representative non-destructive stress profiling methods. However, the two methods are difficult to be utilized for field test due to the instruments are not portable, furthermore, accessibility for general users is extremely low because of relatively time-consuming and expensive process. In case of instrumented indentation testing, research for evaluating through-thickness residual stress has not been tried, even if it has many technical advantages comparing with other techniques, such as low damage to specimen, simple test procedure and high field applicability.

The objective of the current study is to develop a new method for evaluating the through-thickness distributing residual stress with instrumented indentation testing in macro-scale, taking advantages of the continuous responding and extensive interacting characteristics, which facilitates stress-profiling with low damage. Current study is based on the indentation stress evaluation model proposed by Lee and Kwon to evaluate the magnitude of residual stress. Conical indenter which has same geometrical penetration volume with Vickers indenter at the same indentation displacement, which is less sensitive to the directionality of non-equibiaxial stress state. Finite element analysis was used for accurate estimating the contribution of residual stress by depth on force difference based on thermal stress developing the stepwise-constant stress distribution. The residual stress depth-profiling methods with indentation test proposed by this thesis facilitates quick and easy field-applicable test with less damage on test specimen compared to the conventional stress-profiling methods.

1.2. Organization of the Thesis

This thesis consists of six chapters. Chapter 1 introduces the objective and the organization of this thesis. Previous researches related with the background of this thesis are introduced in Chapter 2. Characteristics of residual stress and the representative measurement methods are introduced in terms of the advantages and limitations. Chapter 3 contains the theoretical modeling for evaluating the through-thickness residual stress distribution using macro-scale instrumented indentation testing. Phenomenological determination of calibration coefficient, relating the force difference with stress by depth, by finite element analysis is described, and computational verifications for different materials shows the necessity of the consideration of material dependency. Chapter 4 provides the modification of model proposed in previous studies and optimization of calibration coefficient depending on mechanical properties of materials by performing dimensional analysis. Chapter 5 shows the experimental verification results with analysis of the experimental error, and points out the potential causes of error. Chapter 6 summarizes the conclusion of this thesis.

References

[1] I.C. Noyan, J.B. Cohen, Residual Stress, Springer-Verlag, New York, USA (1987).

[2] G.S. Schajer, Practical residual stress measurement methods, John Wiley & Sons2013.

[3] H.E. Coules, G.C.M. Horne, K. Abburi Venkata, T. Pirling, The effects of residual stress on elastic-plastic fracture propagation and stability, Materials & Design 143 (2018) 131-140.

[4] L. Li, X. Gu, S. Sun, W. Wang, Z. Wan, P. Qian, Effects of welding residual stresses on the vibration fatigue life of a ship's shock absorption support, Ocean Engineering 170 (2018) 237-245.

[5] W.-C. Chung, J.-Y. Huang, L.-W. Tsay, C. Chen, Stress corrosion cracking in the heat-affected zone of A508 steel welds under high-temperature water, Journal of Nuclear Materials 408(1) (2011) 125-128.

[6] P.J. Withers, Residual stress and its role in failure, Reports on Progress in Physics 70(12) (2007) 2211-2264.

[7] C. Sungki, L. Junsang, L. Jae-Yik, K. Seung-kyun, K. Young-cheon, L. Seung-joon, K. Dongil, Effect of Low Transformation Temperature Welding Consumable on Microstructure, Mechanical Properties and Residual Stress in Welded Joint of A516 Carbon Steel, 대한금속재료학회지 59(8) (2021) 524-532.

[8] Y. Mikami, Y. Morikage, M. Mochizuki, M. Toyoda, Angular distortion of fillet welded T joint using low transformation temperature welding wire, Science and Technology of Welding and Joining 14(2) (2009) 97-105.

[9] M.R. Hill, A.T. DeWald, A.G. Demma, L.A. Hackel, H.-L. Chen, C.B. Dane, R.C. Specht, F.B. Harris, Recent developments in laser peening technology, Advanced Materials and Processes (2003).

[10] A. Amanov, Y.-S. Pyun, S. Sasaki, Effects of ultrasonic nanocrystalline surface modification (UNSM) technique on the tribological behavior of sintered Cu-based alloy, Tribology International 72 (2014) 187-197.

[11] M. Kobayashi, T. Matsui, Y. Murakami, Mechanism of creation of compressive residual stress by shot peening, International Journal of Fatigue 20(5) (1998) 351-357.

[12] G.S. Schajer, Relaxation methods for measuring residual stresses:

techniques and opportunities, Experimental mechanics 50(8) (2010) 1117-1127.
[13] G.S. Schajer, Measurement of Non-Uniform Residual Stresses Using the Hole-Drilling Method. Part I—Stress Calculation Procedures, Journal of Engineering Materials and Technology 110(4) (1988) 338-343.
[14] G.S. Schajer, Measurement of Non-Uniform Residual Stresses Using the Hole-Drilling Method. Part II—Practical Application of the Integral Method, Journal of Engineering Materials and Technology 110(4) (1988) 344-349.
[15] M.B. Prime, M.R. Hill, Residual stress, stress relief, and inhomogeneity in aluminum plate, Scripta Materialia 46(1) (2002) 77-82.
[16] M.B. Prime, T. Gnäupel-Herold, J.A. Baumann, R.J. Lederich, D.M. Bowden, R.J. Sebring, Residual stress measurements in a thick, dissimilar aluminum alloy friction stir weld, Acta Materialia 54(15) (2006) 4013-4021.
[17] S.R. Prime MB, Edwards JM, Baumann JA, Lederich RJ. , CONTOUR-METHOD DETERMINATION OF PARENT-PART RESIDUAL STRESSES USING A PARTIALLY RELAXED FSW TEST SPECIMEN, SEM X (2004).
[18] M.R. Hill, The Slitting Method, Practical Residual Stress Measurement Methods (2013) 89-108.
[19] A.J. Allen, M.T. Hutchings, C.G. Windsor, C. Andreani, Neutron diffraction methods for the study of residual stress fields, Advances in Physics 34(4) (1985) 445-473.
[20] J.P. Oliveira, F.M.B. Fernandes, R.M. Miranda, N. Schell, J.L. Ocaña, Residual stress analysis in laser welded NiTi sheets using synchrotron X-ray diffraction, Materials & Design 100 (2016) 180-187.
[21] A. Umapathi, S. Swaroop, Measurement of residual stresses in titanium alloys using synchrotron radiation, Measurement 140 (2019) 518-525.
[22] T.Y. Tsui, W.C. Oliver, G.M. Pharr, Influences of stress on the measurement of mechanical properties using nanoindentation .1. Experimental studies in an aluminum alloy, J. Mater. Res. 11(3) (1996) 752-759.
[23] A. Bolshakov, W.C. Oliver, G.M. Pharr, Influences of stress on the measurement of mechanical properties using nanoindentation .2. Finite element simulations, J. Mater. Res. 11(3) (1996) 760-768.
[24] S. Suresh, A.E. Giannakopoulos, A new method for estimating residual stresses by instrumented sharp indentation, Acta Materialia

46(16) (1998) 5755-5767.
[25] E. Atar, C. Sarioglu, U. Demirler, E. Kayali, H. Cimenoglu, Residual stress estimation of ceramic thin film by X-ray diffraction and indentation techniques, Scripta Materialia 48 (2003) 1331-1336.
[26] Z. Wang, L. Deng, J. Zhao, Estimation of residual stress of metal material without plastic plateau by using continuous spherical indentation, International Journal of Pressure Vessels and Piping 172 (2019) 373-378.
[27] J.I. Jang, Estimation of residual stress by instrumented indentation: A review, Journal of Ceramic Processing Research 10(3) (2009) 391-400.
[28] Y.-H. Lee, D. Kwon, Estimation of biaxial surface stress by instrumented indentation with sharp indenters, Acta Materialia 52(6) (2004) 1555-1563.
[29] Y.-H. Lee, D. Kwon, Residual stresses in DLC/Si and Au/Si systems: Application of a stress-relaxation model to the nanoindentation technique, J. Mater. Res. 17(4) (2002) 901-906.
[30] Y.-H. Lee, D. Kwon, Measurement of residual-stress effect by nanoindentation on elastically strained (100) W, Scripta Materialia 49(5) (2003) 459-465.
[31] Y.H. Lee, W.j. Ji, D. Kwon, Stress measurement of SS400 steel beam using the continuous indentation technique, Experimental Mechanics 44(1) (2004) 55-61.
[32] Y.-H. Lee, K. Takashima, D. Kwon, Micromechanical analysis on residual stress-induced nanoindentation depth shifts in DLC films, Scripta Materialia 50(9) (2004) 1193-1198.
[33] M. Mahmoodi, M. Sedighi, D.A. Tanner, Investigation of through thickness residual stress distribution in equal channel angular rolled Al 5083 alloy by layer removal technique and X-ray diffraction, Materials & Design 40 (2012) 516-520.
[34] M.L. Martinez-Perez, F.J. Mompean, J. Ruiz-Hervias, C.R. Borlado, J.M. Atienza, M. Garcia-Hernandez, M. Elices, J. Gil-Sevillano, R.L. Peng, T. Buslaps, Residual stress profiling in the ferrite and cementite phases of cold-drawn steel rods by synchrotron X-ray and neutron diffraction, Acta Materialia 52(18) (2004) 5303-5313.

Chapter 2

RESEARCH BACKGROUND

Contents

2.1. Residual stress ········· 13

2.1.1. Origins of residual stress ········· 13

2.1.2. Effect of residual stress on materials ········· 14

2.2. Residual stress evaluation methods ········· 16

2.2.1. Destructive methods ········· 16

2.2.2. Non-destructive methods ········· 22

2.3 Indentation methods ········· 25

2.4 Limitations of previous methods ········· 35

References 49

2.1. Residual stress

2.1.1. Origin of residual stress

Residual stress is a “locked-in” stress remaining in materials and structures even after eliminating the sources of external load or stress [1]. Interactions among the process time, exposed temperature, non-uniform elastic-plastic deformation and microstructural transformation result in the residual stress of materials [2]. The interactions develop elastic stress in response to the local incompatible strains to preserve dimensional continuity [1]. The stress has self-equilibrating character to satisfy the force and moment equilibrium in whole volume of materials as shown in Figure 2.1

Most of manufacturing processes originate the residual stresses regardless of the scale and shape of components [1]. For example, forming process to change the shape of materials and surface modification process, involving non-uniform plastic deformation, including rolling, extruding and peening is main mechanism creating residual stress. Manufacturing process including heat treatment, such as welding, casting and induction hardening, is related to microstructural phase transformation of metals and ceramics which occurs the local changes in material density.

2.1.2. Effect of residual stress on materials

Existence of residual stress changes the performance of materials and distorts the residual life time prediction of components, furthermore, sometimes it causes dramatic deformation and crack formation as in Figure 2.2. High level of tensile residual stress, especially, influences hazardous effect on performances which shall be carefully considered to design the structural components. For example, welding residual stress, generally developing tensile residual stress comparable to yield strength in weld and heat-affected zone, causes harmful effect such as reduction in buckling strength, crack resistance and causes stress corrosion cracking and hydrogen cracking [3].

Tensile residual stress generally shortens the fatigue life of materials subjected to cyclic loading, otherwise, compressive residual stress increases the life [4]. Li. Li et al presented the modification of *S*-*N* curves considering the effect of welding residual stress for the high-nitrogen steel, utilized as support material, with yield strength of 470 MPa [5]. The tensile stress about 90% of yield strength shows fatigue life about 35 days, when the fatigue life of support with stress of 200 MPa was over 50 years [5], as the nucleation and propagation of the fatigue cracks altered by residual stress [6].

Surface residual stress around micro-cracks assists the crack opening and closure of depending the direction of stress changing the stress field around the crack tip. H.E. Coules et al. showed the effect of residual stress on crack propagation resistance by comparing as-manufactured Compact Tension specimen with tensile residual stress applied specimen by pre-loading [7]. Stress applied specimen showed accelerated the crack initiation and propagation at the first few millimeters of crack opening, and the more plastic deformation was observed at the lower load applied for making same extension than as-prepared specimen. Stress corrosion cracking is another critical issue, when tensile stress is combined with a corrosive environment, assisting the widening of cracks by taking a role as additional load [8]. Advanced manufacturing process by controlling key parameter for minimizing tensile residual stress and surface modification technique applying compressive stress on the surface of materials have been developed [9-14].

2.2. Residual stress evaluation methods

2.2.1. Destructive methods

2.2.1.1. Hole-drilling method

The hole-drilling method, the most commonly utilized measurement, evaluates the residual stress by measuring the relaxed strains, which are results of released stresses in drilling process eliminating the continuity of material [15-18]. Elastically recovered strain on surface of materials in three different directions can determine the unique plane stress tensor with elastic modulus and Poisson's ratio. Therefore, three strains with 45 degree intervals are generally measured, and Eq. (2-1) and Eq. (2-2) shows the stress components in the principal stress direction.

$$\sigma_{res}^{\max} = \frac{\varepsilon_1 + \varepsilon_3}{4A} + \frac{1}{4B}\sqrt{(\varepsilon_3 - \varepsilon_1)^2 + (\varepsilon_3 + \varepsilon_1 - 2\varepsilon_2)^2} \tag{2-1}$$

$$\sigma_{res}^{\min} = \frac{\varepsilon_1 + \varepsilon_3}{4A} - \frac{1}{4B}\sqrt{(\varepsilon_3 - \varepsilon_1)^2 + (\varepsilon_3 + \varepsilon_1 - 2\varepsilon_2)^2} \tag{2-2}$$

ε_1, ε_2 and ε_3 indicate the strain values when the angle between the direction of ε_1 and ε_3 is right angle, A and B are constants calculated from the elastic properties of the target material.

Conventional hole-drilling uses rosette type strain gauge made of patterned metal foil on polymer substrate and metallic drill cutter for the measurement as in shown Figure 2.3 (a) [18], which restrict the spatial resolution due to the size of rosette and cutter. Strain measurement using Moir´e Interferometry [19], holographic interferometry [20] or digital image correlation (DIC) methods [21-23] have been researched to overcome the obstacle. The replacement of conventional strain gauge facilitates the expansion of the measurement down to micro/nano-scale range, for example, by analyzing scanning electron microscope image of surface processed by focused ion beam [23, 24]

Hole-drilling method can be used for evaluating the non-uniform residual stress with depth by sequential drilling and strain measuring process [15, 16, 18]. Integral method is the most popular and well-calibrated calculation method for depth profiling of residual stress, comparing with others, such as incremental strain method and average strain method. The calibration process of integral method uses finite element analysis to investigate relation between the strain on the material's surface and stress released with drilling depth. The strain changes at the surface by the relaxed stress could be considered as equal to the strain when stress applied to the wall of hole. Figure 2.4 shows schematic interpretation for the procedure to obtain the calibration coefficient matrix, $\bar{a}$, indicating the relation between strain relaxation and the stresses at each unit increment, when the hole drilled by four increments. Strains occurred by each unit depth stress were analyzed respectively, due to the stresses from surface down to the hole depth generate the strain changes continuously with increasing hole depth. For example, $\bar{a}_{43}$ means the strain generated by the third unit stress when a hole depth is four increments deep. In matrix notation, equation relates the stress and strain as Eq. (2-3), Eq. (2-4) and Eq. (2-5),

$$\bar{a}\ \mathrm{P} = E/(1+\nu)\ \mathrm{p} \tag{2-3}$$

$$\bar{b}\ \mathrm{P} = E/(1+\nu)\ \mathrm{q} \tag{2-4}$$

$$\bar{b}\ \mathrm{T} = E/(1+\nu)\ \mathrm{t} \tag{2-5}$$

when P, Q, T, p, q and t are defined as following equations

$$\mathrm{P} = \frac{\sigma_x+\sigma_y}{2} \qquad \mathrm{Q} = \frac{\sigma_x-\sigma_y}{2} \qquad \mathrm{T} = \tau_{xy} \tag{2-6}$$

$$\mathrm{p} = \frac{\varepsilon_3+\varepsilon_1}{2} \qquad \mathrm{q} = \frac{\varepsilon_3-\varepsilon_1}{2} \qquad \mathrm{t} = \frac{\varepsilon_3-2\varepsilon_2+\varepsilon_1}{2} \tag{2-7}$$

The Eq. (2-3) is represented in full matrix notation as equation (2-8), when hole drilled with four increments deep.

$$\begin{bmatrix} \bar{a}_{11} & & & \\ \bar{a}_{21} & \bar{a}_{22} & & \\ \bar{a}_{31} & \bar{a}_{32} & \bar{a}_{33} & \\ \bar{a}_{41} & \bar{a}_{42} & \bar{a}_{43} & \bar{a}_{44} \end{bmatrix} \begin{bmatrix} P_1 \\ P_2 \\ P_3 \\ P_4 \end{bmatrix} = \frac{E}{1+\nu} \begin{bmatrix} p_1 \\ p_2 \\ p_3 \\ p_4 \end{bmatrix} \tag{2-8}$$

Ring-core method and deep hole-drilling are similar stress evaluation technique to hole-drilling method as presented in Figure 2.3. Ring-core method remove the materials surrounding the stacked tri-axial strain gauge rosette. Deep hole-drilling method drills the reference hole completely passing through the material and makes a cylinder of material containing the reference hole. The diameter changes of reference hole through the depth provides the strain by relaxed stress.

2.2.1.2. Slitting method

Slitting method is one of relaxation method capable of measurement for the through-thickness distributing residual stress making long slit by wire electrical discharge machining, sawing or milling. Generated strain by stress relaxation is measured on the front and/or back surfaces by attaching uniaxial strain gauges normal to machined plane as shown in Figure 2.3 (d). This method can provide stress profile over the entire thickness of specimen which is clear advantage comparing with hole-drilling, however, the evaluated stress component is restricted to measurement of the stress normal to the cut surface. Estimation of residual stress proceeds using compliance matrix determined by finite element analysis for each geometry of target component in a same way as hole-drilling methods for the determination of calibration coefficient.

2.2.1.3. Sectioning method

Sectioning method is a stress evaluation technique based on stress relaxation by through-depth plane cutting [25-27]. This method is generally combined with several other techniques, including strain measurement by strain gauge and image processing, and diffraction methods to evaluate the residual stress. The residual stresses, in general, can be calculated from the biaxial strain changes $(\varepsilon_x, \varepsilon_y)$ that occur during stress relaxation as Eqs. (2-9) and (2-10).

$$\sigma_{res}^{x} = \frac{E}{1-\nu^2}(\varepsilon_x + \nu\varepsilon_y) \tag{2-9}$$

$$\sigma_{res}^{y} = \frac{E}{1-\nu^2}(\varepsilon_y + \nu\varepsilon_x) \tag{2-10}$$

The attachment location of strain measurement shall be cautiously determined due to the magnitude of relaxed stresses is highly varied by the distance from cutting surface. The sequential cutting as shown in Figure 2.5 can be applied for complex shape of component which can be applied to profile the stress distribution of materials.

2.2.1.4. Contour method

The contour method, relatively recently developed technique, is stress mapping technique combining the sectioning method and finite element analysis for measuring the normal stress of cutting plane [28]. This method generally targeted on metallic material which can be machined by electrical discharge machining, minimizing the plasticity during the stress relaxation process. Outer-plane displacements are measured on the both sides of cut surface by surface scanning technique and filtered to remove the effect of surface roughness and noise. Stresses normal to cross-section are analyzed by returning the surface displaced as measured data to flat surface through finite element simulation. The schematic procedures are shown in Figure 2.6.

2.2.2. Non-destructive Methods

2.2.2.1. X-ray diffraction method

X-ray diffraction method is a representative diffraction method measuring lattice spacing of crystalline or polycrystalline materials. The angles where the strong emission generated are detected and the distance can be calculated by Bragg's law. The strain change caused by residual stress can be calculated by Eq. (2-6), when the measured distance from stressed state is d, and from the stress-free state is d_0.

$$\frac{d_{\psi,\phi} - d_0}{d_0} = \frac{1}{E}\left[\sigma_\phi (1+\nu) sin^2 \psi\right] \tag{2-6}$$

Diffraction methods are advantageous to be utilized non-destructively, which means planned or in operating components can be evaluated without damage [29]. However, the penetration depth of the X-ray diffraction methods is generally restricted up to tens of micrometers and varies with target material and surface condition. The stress profiling can be made by combining layer removing method with X-ray diffraction [30] forgiving the advantage of non-destructivity. Synchrotron X-ray [31] and neutron diffraction [32] can penetrate deeper depth using high energy intensity of electron or neutron beam than X-ray diffraction; over tens of millimeters ranges.

2.2.2.2. Ultrasonic method

The ultrasonic method involves the speed of acoustic wave altered linearly by the stress within a material. The velocity of ultrasonic wave varying with residual stress is represented as Eq. (2-7),

$$V_T = V_{T0} + K_{ae}\sigma_{res} \qquad (2-6)$$

when the acoustoelastic constant is K_{ae} and residual stress is σ_{res}. The direction of ultrasonic output and receiving devices simply determines the direction of measured residual stress, however, complicate shaped or minimal sized components are difficult to be measured due to size of devices. Additionally, the evaluated stress is averaged stress along the path of ultrasonic wave; local stress cannot be measured. The physical factors that changes the ultrasonic wave speed can distort the result from ultrasonic method, such as microstructure and temperature. Downsizing of ultrasound equipment shall be preceded to apply the method for evaluating the local stress distribution.

2.2.2.3. Barkhausen noise method

Barkhousen noise method measures the number and magnitude of magnetic re-orientation of material. Ferromagnetic materials including steels and some of ceramics can apply this method for stress evaluation by exposed in AC magnetic field. The magnetic response of material is non-linear showing small jump in magnetic flux density-magnetic field strength curve. The irregular jumps, noise-like signal, are changed by elastic stress distribution in materials which can be empirically calibrated. However, the Barkhause noise is highly influenced by microstructure of material, therefore, stress evaluation for the materials with gradient in microstructure is difficult.

2.3. Indentation methods

Instrumented indentation testing (IIT) is a mechanical test measuring the continuous response of material by penetrating the indenter on the surface of material. Applied force with penetrated displacement is monitored during the loading-unloading test cycle as introduced in ASMT E2546-15 [33] as shown in Figure 2.7. Analysis of an indentation force-displacement curve were mainly used to evaluate the hardness and elastic modulus of materials. Nowadays, IIT technique have been expanded to estimate local mechanical responses in terms of tensile properties [34-41], fracture toughness [42, 43] and residual stress [44-51], semi-destructively. IIT is advantageous technique to selectively determine the measuring depth and area controlling the maximum indentation displacement and shape of indenter.

IIT technique, unlike conventional hardness testing, information about contact area can be obtained directly using the parameters from the indentation force-displacement curves without optical observations. The accurate evaluation of indentation contact depth (h_c) from the indentation force-displacement curves has been studied by many researchers. Elastic deflection and/or plastic pileup/sink-in of material surrounding the indenter were considered to estimate the accurate indentation contact depth (h_c). Figure 2.8 shows the difference in h_c depending on estimation methods. The contact depth can be expressed as Eq. (2-7) when the elastic deflection is h_d, pileup height is h_{pileup} and the maximum indentation depth is h_{max}.

$$h_c = h_{max} - h_d + h_{pileup} \tag{2-7}$$

$$h_d = \varepsilon \frac{F_{max}}{S} \tag{2-8}$$

The calculation of elastic deflection is suggested by Oliver and Pharr [52] as represented in Eq. (2-8), when the ε is a geometric constant, S is indentation stiffness at the maximum force (F_{max}). The geometric constant involves with the shape of the indenter; 0.75 for a spherical indenter and 0.72 for conical indenter. S is slope of the early part of unloading curve, which can be calculated in form of Eq. (2-9)

$$S = \frac{dF}{dh} \text{ (at } h = h_c\text{)} \tag{2-9}$$

Contact depth equation proposed by Oliver and Phaar didn't consider the pileup depth, therefore, the h_c in Eq. (2-7) eleminating h_{pileup} combining the Eqs. (2-8) and (2-9) can be calculated from loading-unloading indentation curve. Studies for estimation of accurate h_c considering h_{pileup} have been performed [53-66]. Elastoplastic mechanical properties of material, such as strain-hardening exponent (n) and yield strain ($\varepsilon_y = \sigma_y/E$), influences the h_{pileup}, when ε_y and σ_y are strain and strength at yield point and E is the elastic modulus. S.H Kim et al. investigated the h_{pileup} is inversely proportional to ε_y and negligible relation with n for the sharp indenters such as Vickers, Berkovich and conical shape, which maintains the geometrical self-similarity with indentation displacement resulting the constrain stain [57]. Spherical indenter inducing the strain changes with increasing indentation displacement shows an inverse relation between the h_{pileup} and n [60].

The lateral displacement of material, which consequently results in pileup, around indenter occurs small for the materials with high n due to the hardening zone press down easily to the lower region toward the direction of indenter axis, resulting in lower h_{pileup}. On the other hand, large lateral displacement is generated for the materials with low n due to the downward movement of hardening zone is difficult, resulting in higher

h_{pileup}. Many different models for estimating the h_c considering the effect of h_{pileup} based on mechanical properties [53-55, 60, 61, 64].

The real contact area, A_c, can be calculated from geometric shape using h_c as Eqs. (2-10) and (2-11) for a spherical shaped and sharp indenter (Vickers indenter and Berkovich indenter), respectively.

$$A_c = \pi(2Rh_c - {h_c}^2) \tag{2-10}$$

$$A_c = 24.5 \cdot {h_c}^2 \tag{2-11}$$

The hardness (H)and the reduced elastic modulus (E_r) can be evaluated following Eqs. (2-12) and (2-13) using A_c from Eqs. (2-10) and (2-11).

$$H = \frac{F_{max}}{A_c} \tag{2-12}$$

$$E_r = \frac{\sqrt{\pi}}{2}\frac{S}{\sqrt{A_c}} \tag{2-13}$$

2.3.1. Residual stress effect on indentation curve

The indentation force-displacement curve shifts depending on the sign and the magnitude of residual stress. Tensile residual stress decreases the indentation force comparing with the force of reference state (zero stress state) at the same indentation displacement, and reverse change occurs at the compressive stress state as shown in Figure 2.9 [51]. Bolshakov et al. showed the same variation of the indentation curve using finite element analysis [67]. Tsui et al. investigated experimentally the effect of residual stress on variation of the indentation parameters including the hardness, stiffness and elastic modulus, however, projected area measured optically was invariant with the stress [68].

2.3.2. Residual stress assessment using Vickers indenter

Lee and Kwon developed residual stress evaluation model applicable to biaxial stress state based on the change in indentation curve. They relate the difference in indentation force from stress-free state at the same indentation displacement with residual stress [51]. The surface residual stress can be decomposed into hydrostatic and deviatoric stress as in Eq. (2-14), when the stress in direction of indenter axis is assumed to be zero due to free-surface

$$\begin{pmatrix} \sigma_{res}^{x} & 0 & 0 \\ 0 & \sigma_{res}^{y} & 0 \\ 0 & 0 & 0 \end{pmatrix} =$$

$$\begin{pmatrix} \sigma_{hyd} & 0 & 0 \\ 0 & \sigma_{hyd} & 0 \\ 0 & 0 & \sigma_{hyd} \end{pmatrix} + \begin{pmatrix} \frac{(2\sigma_{res}^{x}-\sigma_{res}^{y})}{3} & 0 & 0 \\ 0 & \frac{(-\sigma_{res}^{x}+2\sigma_{res}^{y})}{3} & 0 \\ 0 & 0 & \frac{-(\sigma_{res}^{x}+\sigma_{res}^{y})}{3} \end{pmatrix} \tag{2-14}$$

where, σ_{res}^{x} and σ_{res}^{y} are stress components normal to each other and parallel to the testing surface, and σ_{hyd} is hydrostatic stress equal to ($\sigma_{res}^{x} + \sigma_{res}^{y}$)/3. They correlated the z-direction deviatoric stress component (indenter axis) with the force difference divided by contact area and verified experimentally [51]. The residual stress can be expressed as Eqs. (2-18) and (2-19)

$$\sigma_{res}^{x} = \frac{3}{1+p}\frac{\Delta L}{A_c} \tag{2-18}$$

$$\sigma_{res}^{y} = \frac{3p}{1+p}\frac{\Delta L}{A_c} \tag{2-19}$$

when the in plane principal stresses are σ_{res}^{x} and σ_{res}^{y}, and p is the ratio of the stresses (=$\sigma_{res}^{y}/\sigma_{res}^{x}$), and ΔL is load difference between stress-free and stressed curve.

2.3.3. Stress directionality assessment

2.3.3.1. Knoop indentation

Lee et al. proposed a method to evaluate the ratio of principal stresses, *p*, by measuring the pile-up height of indentation imprints [69]. Han and Choi [70] suggested a model using a Knoop indenter, anisotropic indenter with a diagonal length ratio of 7.11, for measuring the stress directionality. The rotated indentations with Knoop indenter for non-equibiaxial stress states show the different load differences due to different stress sensitivity with direction. Conversion factors, $\alpha_{\perp}$ and $\alpha_{//}$, were introduced to correlate directional indentation force differences with residual stresses normal to each other for a biaxial stress state. The relation between the stresses and load differences of Figure 2.10 can be represented as Eqs.20 and 21.

$$\Delta L_1 = \alpha_{//}\sigma_{res}^{y} + \alpha_{\perp}\sigma_{res}^{x} \quad (2\text{-}20)$$

$$\Delta L_2 = \alpha_{//}\sigma_{res}^{x} + \alpha_{\perp}\sigma_{res}^{y} \quad (2\text{-}21)$$

The ratio of conversion factors $(\frac{\alpha_{//}}{\alpha_{\perp}})$ is revealed to constant at 0.34

regardless of indentation displacement and stressed state as represented in Figure 2.11 [70]. Additionally, the ratio of load differences from normal Knoop indentation can be represented with the ratio of conversion factor and directional stress components.

$$\frac{\Delta L_x}{\Delta L_y} = \frac{\alpha_{//}\sigma_{res}^{x}+\alpha_{\perp}\sigma_{res}^{y}}{\alpha_{\perp}\sigma_{res}^{x}+\alpha_{//}\sigma_{res}^{y}} = \frac{\frac{\alpha_{//}}{\alpha_{\perp}}+\frac{\sigma_{res}^{y}}{\sigma_{res}^{x}}}{1+\frac{\alpha_{//}\sigma_{res}^{y}}{\alpha_{\perp}\sigma_{res}^{x}}} = \frac{\frac{\alpha_{//}}{\alpha_{\perp}}+p}{1+\frac{\alpha_{//}}{\alpha_{\perp}}p} \tag{2-22}$$

Therefore, two load differences and pre-known conversion factor ratio can define the ratio of principal stresses as Eq. 2-23, when the principal direction is known.

$$p = \frac{\sigma_{res}^{y}}{\sigma_{res}^{x}} = \frac{\frac{\Delta L_x}{\Delta L_y}-\frac{\alpha_{//}}{\alpha_{\perp}}}{1-\frac{\alpha_{//}\Delta L_x}{\alpha_{\perp}\Delta L_y}} \tag{2-23}$$

Using Eqs. (2-18), (2-19) and (2-23) σ_{res}^{x} and σ_{res}^{y} can be evaluated. Kim et al. developed extended Knoop indenter model to estimate the principal direction of residual stress (θ_p) and *p* with four rotated Knoop indentation curves [71]. Two sets of Knoop indentations with angle intervals of 45 degrees can obtain the two ratios of stresses as Eqs. (2-24)

$$p' = \frac{\sigma_{res}^{90}}{\sigma_{res}^{0}} = \frac{\frac{\Delta L_0}{\Delta L_{90}}-\frac{\alpha_{//}}{\alpha_{\perp}}}{1-\frac{\alpha_{//}\Delta L_0}{\alpha_{\perp}\Delta L_{90}}},\ p'' = \frac{\sigma_{res}^{135}}{\sigma_{res}^{45}} = \frac{\frac{\Delta L_{45}}{\Delta L_{135}}-\frac{\alpha_{//}}{\alpha_{\perp}}}{1-\frac{\alpha_{//}\Delta L_{45}}{\alpha_{\perp}\Delta L_{135}}} \tag{2-24}$$

Using the equations of plane stress transformation represented in

Eqs. (2-25) and (2-26),

$$\sigma_\theta = \frac{\sigma_{res}^0+\sigma_{res}^{90}}{2} + \frac{\sigma_{res}^0+\sigma_{res}^{90}}{2}\cos(2\theta) + \tau_{xy}\sin(2\theta) \qquad (2\text{-}25)$$

$$\tan(2\theta_p) = \frac{2\tau_{xy}}{\sigma_{res}^0-\sigma_{res}^{90}} \qquad (2\text{-}26)$$

θ_p, and p can be expressed using Eqs. from (2-24) to (2-26) as Eq.s (2-26) and (2-27), where σ_1 and σ_2 are the maximum and the minimum principal stresses.

$$\tan(2\theta_p) = \frac{(1-p')(1+p")}{(1-p')(1+p")} \qquad (2\text{-}26)$$

$$\frac{\sigma_2}{\sigma_1} = \frac{(1+p')\cos(2\theta_p)-(1-p')}{(1+p')\cos(2\theta_p)+(1-p')} \qquad (2\text{-}27)$$

Kim[72] and Xu[73] proposed a new shape indenter by extending the conventional Berkovich indenter in one direction and named it as modified Berkovich indenter (Fig. 2.13). These studies are based on the assumption of isotropic mechanical properties.

2.3.3.2. Modified Berkovich indentation

Modified Berkovich indentation was proposed to evaluate the directionality and the principal direction of residual stress in nano-scale indentation due to the difficulty in fabrication of Knoop indenter [72, 73]. Modified Berkovich indenter has diagonal length ratio of 3 and contains three surfaces, which provide unique intersecting points unlike Knoop indenter. The characteristic enables the Modified Berkovich to yield small indenter bluntness appropriate to be utilized for nano-scale indentation.

2.3.3.3. Indentation with digital image correlation

Kim proposed a method to evaluate the directionality and principal direction of residual stress using IIT with digital image correlation as shown in Figure 2.12 [74]. Conical indentation generates the isotropic in-plane displacement around the indented area, if the material shows isotropic mechanical properties. The presence of residual stress varies the magnitude of the displacements by directions. Principal directions of residual stress and the stress ratio of principal stresses can be evaluated by analyzing the radial displacements, if the displacement data for stress-free state is measured.

2.4. Limitations of previous method

Residual stress evaluation generally performed with two or more measurement method as complementary due to the limitations of each measurement method. Relaxation method may cause large plastic deformation around the stress relieved area, which yields overestimation of residual stress [75, 76]. If the residual stress level around the hole is similar to the yield strength of the material, material removal process induces deformation, rather than mitigating them, resulting in the additional strain, which interferes with accurate residual stress evaluations. X-ray diffraction method for the through-thickness residual stress evaluation requires the combination with layer removing by chemical etching. Therefore, it is time-consuming process and volume with depth corresponding to the depth of stress need to be eliminated. Furthermore, the measured stresses by X-ray diffraction highly depend on the microstructure and grain size of material due to diffraction data does not obtained at specific orientation. Therefore, appropriate determination of X-ray elastic constant shall be required [77, 78] Neutron and synchrotron diffraction methods are capable to measure the through-thickness residual stress non-destructively, however, accessibility for the methods are extremely low.

Instrumented indentation testing has merits on semi-destructive method to evaluate local mechanical response, and the continuous force-displacement curve are potential to be utilized for profiling of stress through the depth. Furthermore, the indentation displacement can be controlled as test condition, which is advantageous to satisfy the requirements for permissible flaw or damage on target component. However, stress evaluation using indentation test has been restricted to measure the magnitude, directionality and principal direction with assumption of uniform stress distribution through the thickness of material. Furthermore, there is few researches that discuss about the depth where the measured stress by indentation really exists. Stress profiling using indentation test was performed by measurements on the cross-section, not by single indentation test on surface. Therefore, method for measuring through-thickness residual stress using indentation, taking advantages of size controllable and field applicable characteristics, is strongly demanded.

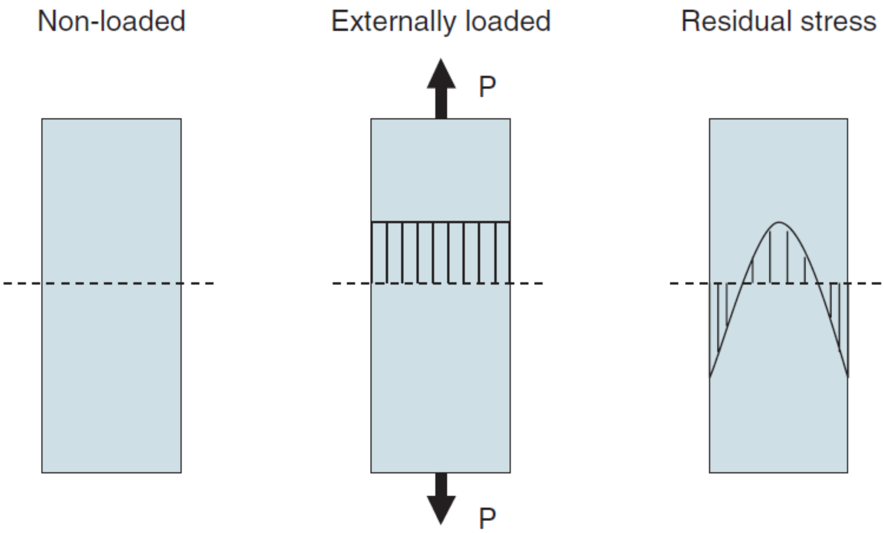

Figure 2.1. Schematic diagram of the residual stress distribution of toughened glass sheet comparing with external load [1]

(a) Warped cargo ramp (b) Cracking in a cast aluminum ingot

Figure 2.2. Effect of residual stress on components [1]

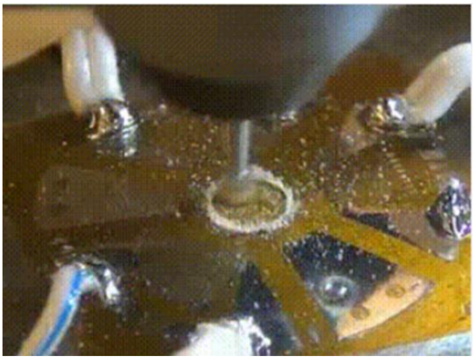

(a) Hole-drilling method

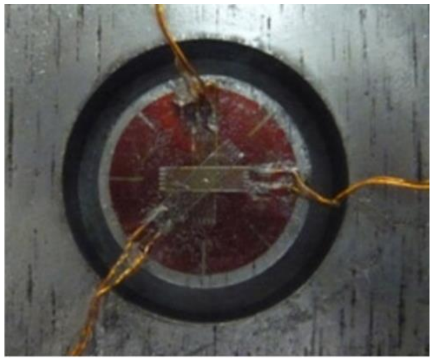

(b) Ring-core method

(c) Deep hole-drilling method

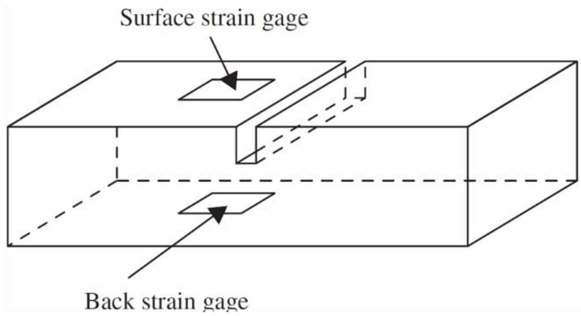

(d) slitting method

Figure 2.3. Residual stress measurement methods

(pictured by VEQTER. Ltd)

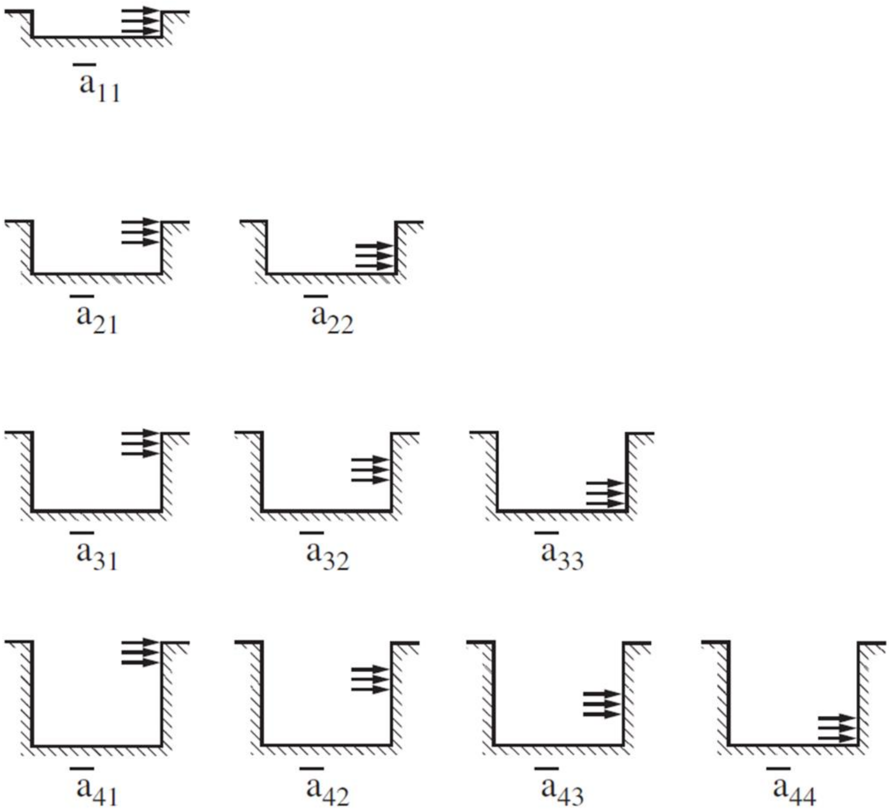

Figure 2.4. Calibration coefficient of hole-drilling method

(Figure adapted from [79])

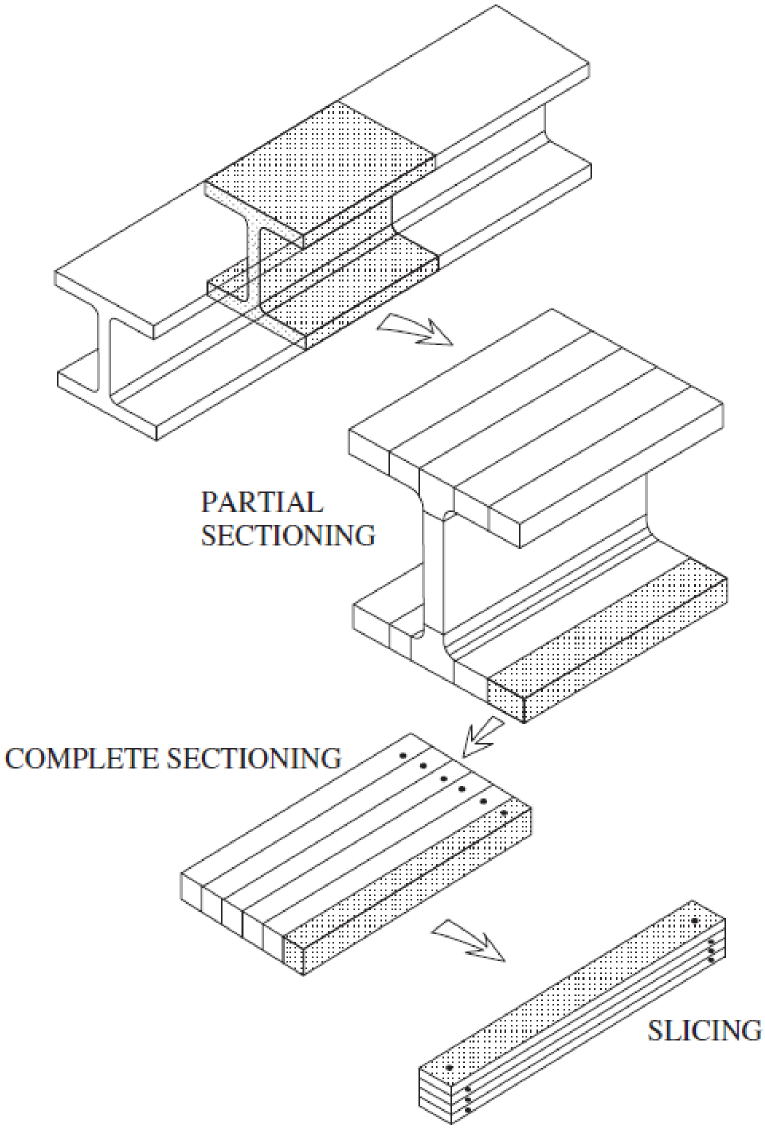

Figure 2.5. Sequential cutting process of sectioning method

(Figure adapted from [26])

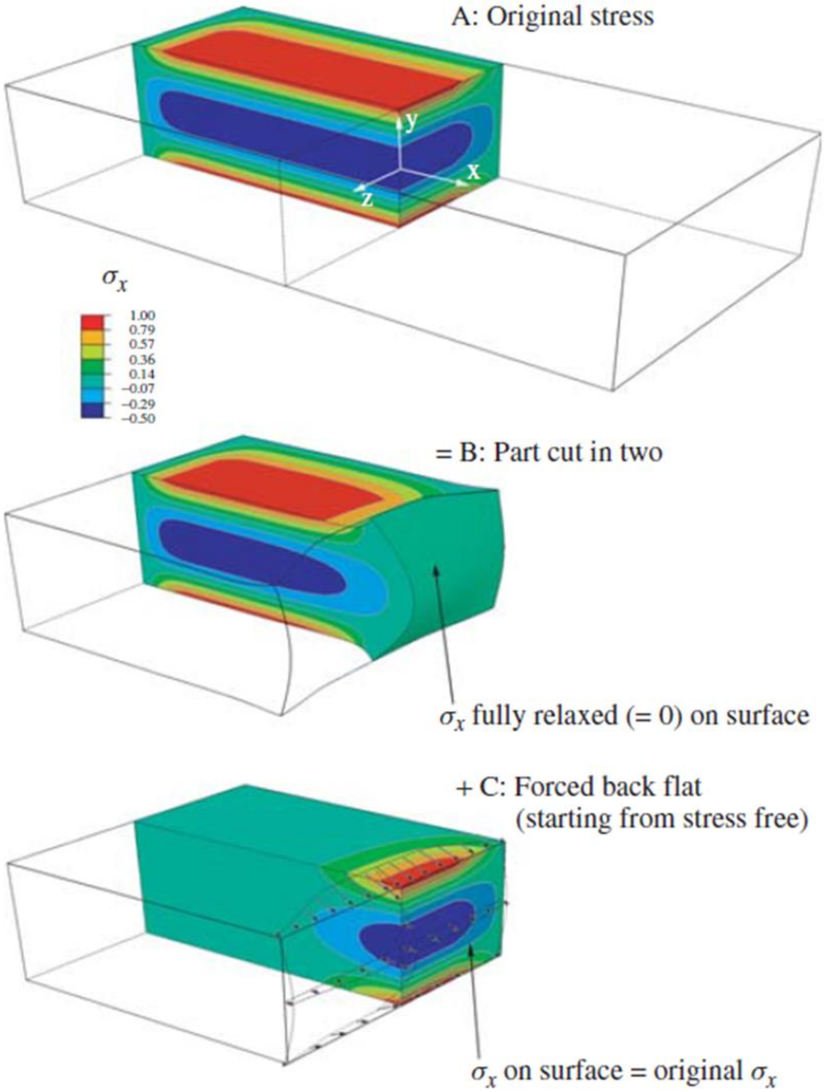

Figure 2.6. Principle of stress evaluation using contour method [1]

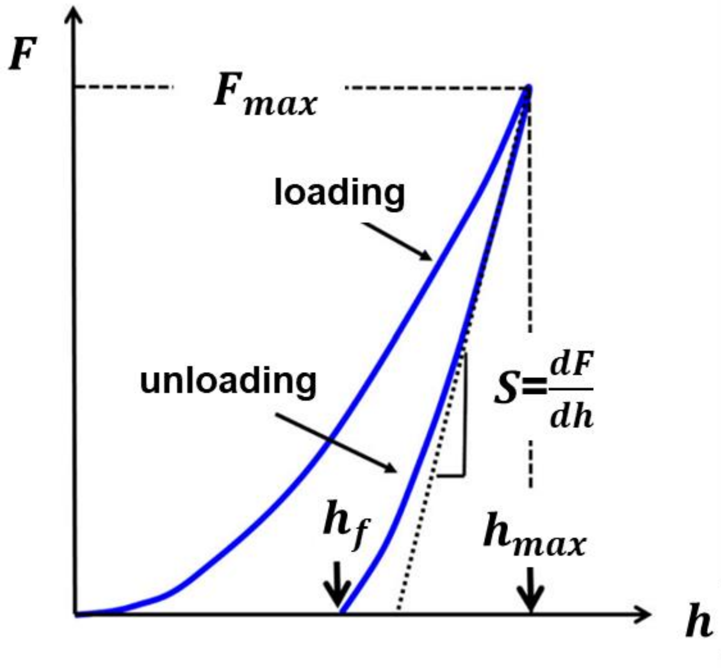

Figure 2.7. Schematic diagram of indentation force-displacement curve

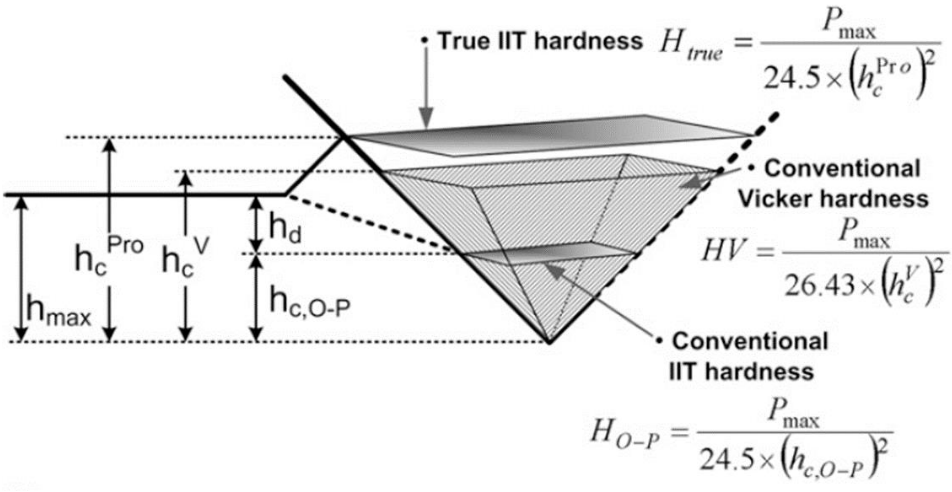

Figure 2.8. Variation of indentation contact depth with estimation methods [80]

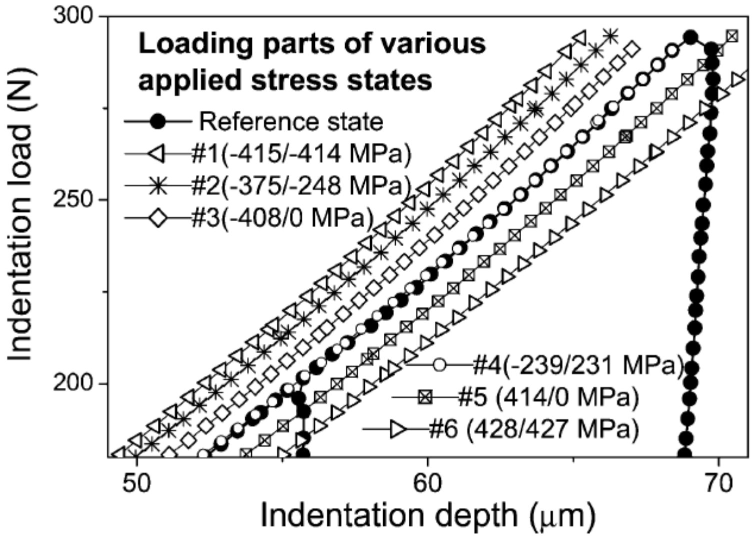

Figure 2.9. Variation of indentation curve of API X65 with stress [51]

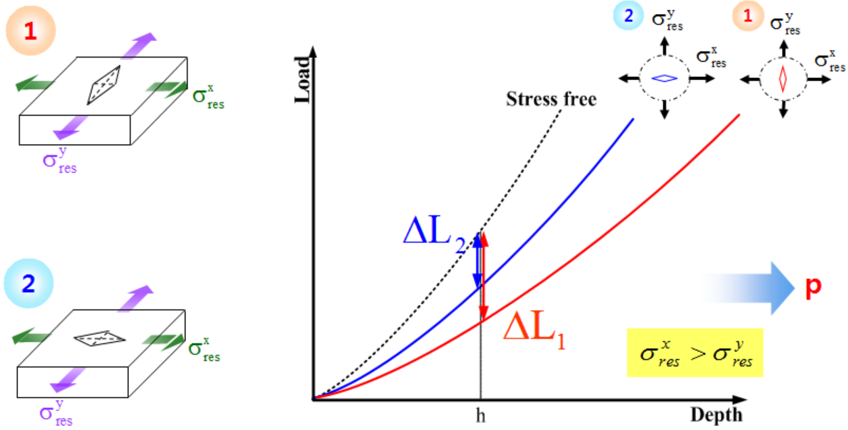

Figure 2.10. Schematic loading curves of Knoop indentations for non-equibiaxial stress state

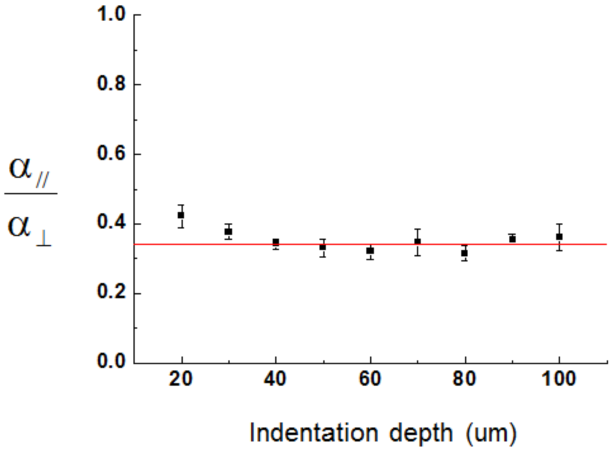

Figure 2.11. Conversion factors ratio with indentation displacement [70]

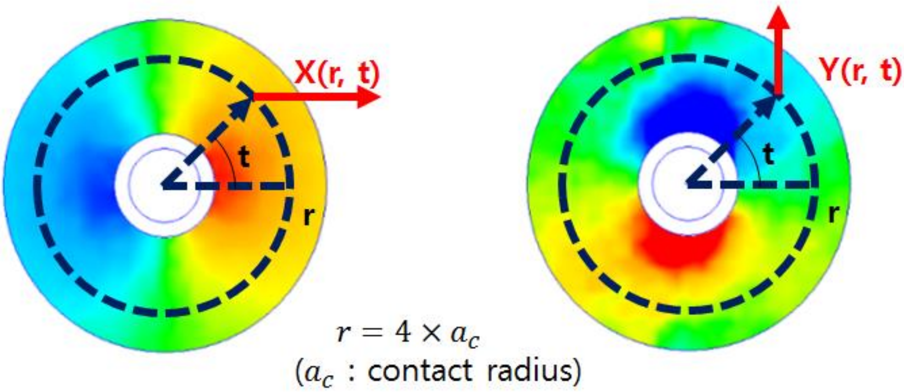

Figure 2.12. Directional in-plane displacements by the conical indentation [74]

References

[1] G.S. Schajer, Practical residual stress measurement methods, John Wiley & Sons2013.

[2] G.E. Totten, Handbook of residual stress and deformation of steel, ASM international2002.

[3] N.S.M. Nasir, M.K.A.A. Razab, S. Mamat, M. Iqbal, Review on welding residual stress, stress 2(5) (2006) 8-10.

[4] X.P. Jiang, X.Y. Wang, J.X. Li, D.Y. Li, C.S. Man, M.J. Shepard, T. Zhai, Enhancement of fatigue and corrosion properties of pure Ti by sandblasting, Materials Science and Engineering: A 429(1) (2006) 30-35.

[5] L. Li, X. Gu, S. Sun, W. Wang, Z. Wan, P. Qian, Effects of welding residual stresses on the vibration fatigue life of a ship's shock absorption support, Ocean Engineering 170 (2018) 237-245.

[6] P.J. Withers, Residual stress and its role in failure, Reports on Progress in Physics 70(12) (2007) 2211-2264.

[7] H.E. Coules, G.C.M. Horne, K. Abburi Venkata, T. Pirling, The effects of residual stress on elastic-plastic fracture propagation and stability, Materials & Design 143 (2018) 131-140.

[8] W. Wang, Rupture and Fracture of Fastener by Embrittlement-Stress Corrosion Cracking (SCC), 2020.

[9] C. Sungki, L. Junsang, L. Jae-Yik, K. Seung-kyun, K. Young-cheon, L. Seung-joon, K. Dongil, Effect of Low Transformation Temperature Welding Consumable on Microstructure, Mechanical Properties and Residual Stress in Welded Joint of A516 Carbon Steel, 대한금속재료학회지 59(8) (2021) 524-532.

[10] Y. Mikami, Y. Morikage, M. Mochizuki, M. Toyoda, Angular distortion of fillet welded T joint using low transformation temperature welding wire, Science and Technology of Welding and Joining 14(2) (2009) 97-105.

[11] M.R. Hill, A.T. DeWald, A.G. Demma, L.A. Hackel, H.-L. Chen, C.B. Dane, R.C. Specht, F.B. Harris, Recent developments in laser peening technology,

Advanced Materials and Processes (2003).
[12] A. Amanov, Y.-S. Pyun, S. Sasaki, Effects of ultrasonic nanocrystalline surface modification (UNSM) technique on the tribological behavior of sintered Cu-based alloy, Tribology International 72 (2014) 187-197.
[13] M. Kobayashi, T. Matsui, Y. Murakami, Mechanism of creation of compressive residual stress by shot peening, International Journal of Fatigue 20(5) (1998) 351-357.
[14] W.-C. Chung, J.-Y. Huang, L.-W. Tsay, C. Chen, Stress corrosion cracking in the heat-affected zone of A508 steel welds under high-temperature water, Journal of Nuclear Materials 408(1) (2011) 125-128.
[15] G.S. Schajer, Measurement of Non-Uniform Residual Stresses Using the Hole-Drilling Method. Part I—Stress Calculation Procedures, Journal of Engineering Materials and Technology 110(4) (1988) 338-343.
[16] G.S. Schajer, Measurement of Non-Uniform Residual Stresses Using the Hole-Drilling Method. Part II—Practical Application of the Integral Method, Journal of Engineering Materials and Technology 110(4) (1988) 344-349.
[17] G.S. Schajer, M. Steinzig, Full-field calculation of hole drilling residual stresses from electronic speckle pattern interferometry data, Experimental Mechanics 45(6) (2005) 526.
[18] A. E837—13a, Standard Test Method for Determining Residual Stresses by the Hole-Drilling Strain-Gage Method, E837-20, West Conshohocken, PA, 2020.
[19] Z. Wu, J. Lu, B. Han, Study of residual stress distribution by a combined method of Moire interferometry and incremental hole drilling, Part I: Theory, (1998).
[20] D. Nelson, J. McCrickerd, Residual-stress determination through combined use of holographic interferometry and blind-hole drilling, Experimental Mechanics 26(4) (1986) 371-378.
[21] A. Baldi, Residual Stress Measurement Using Hole Drilling and Integrated Digital Image Correlation Techniques, Experimental Mechanics 54(3) (2014) 379-391.
[22] J.D. Lord, D. Penn, P. Whitehead, The Application of Digital Image

Correlation for Measuring Residual Stress by Incremental Hole Drilling, Applied Mechanics and Materials 13-14 (2008) 65-73.

[23] B. Winiarski, P.J. Withers, Micron-Scale Residual Stress Measurement by Micro-Hole Drilling and Digital Image Correlation, Experimental Mechanics 52(4) (2012) 417-428.

[24] B. Winiarski, P.J. Withers, Mapping residual stress profiles at the micron scale using FIB micro-hole drilling, Applied Mechanics and Materials, Trans Tech Publ, 2010, pp. 267-272.

[25] B. Young, W.-M. Lui, Behavior of Cold-Formed High Strength Stainless Steel Sections, Journal of Structural Engineering 131(11) (2005) 1738-1745.

[26] N. Tebedge, G. Alpsten, L. Tall, Residual-stress measurement by the sectioning method, Experimental Mechanics 13(2) (1973) 88-96.

[27] J.R. Shadley, E.F. Rybicki, W.S. Shealy, Application guidelines for the parting out step in a through thickness residual stress measurement procedure, Strain 23(4) (1987) 157-166.

[28] M.B. Prime, T. Gnäupel-Herold, J.A. Baumann, R.J. Lederich, D.M. Bowden, R.J. Sebring, Residual stress measurements in a thick, dissimilar aluminum alloy friction stir weld, Acta Materialia 54(15) (2006) 4013-4021.

[29] C.E. Murray, I. Cevdet Noyan, Applied and Residual Stress Determination Using X-ray Diffraction, Practical Residual Stress Measurement Methods (2013) 139-161.

[30] M. Mahmoodi, M. Sedighi, D.A. Tanner, Investigation of through thickness residual stress distribution in equal channel angular rolled Al 5083 alloy by layer removal technique and X-ray diffraction, Materials & Design 40 (2012) 516-520.

[31] J.P. Oliveira, F.M.B. Fernandes, R.M. Miranda, N. Schell, J.L. Ocaña, Residual stress analysis in laser welded NiTi sheets using synchrotron X-ray diffraction, Materials & Design 100 (2016) 180-187.

[32] M.L. Martinez-Perez, F.J. Mompean, J. Ruiz-Hervias, C.R. Borlado, J.M. Atienza, M. Garcia-Hernandez, M. Elices, J. Gil-Sevillano, R.L. Peng, T. Buslaps, Residual stress profiling in the ferrite and cementite phases of cold-drawn steel

rods by synchrotron X-ray and neutron diffraction, Acta Materialia 52(18) (2004) 5303-5313.
[33] G. Acharya, K. Park, Adv. Drug Delivery Rev. 58 (2006) 387.
[34] K.-H. Kim, Y.-C. Kim, E.-c. Jeon, D. Kwon, Evaluation of indentation tensile properties of Ti alloys by considering plastic constraint effect, Materials Science and Engineering: A 528(15) (2011) 5259-5263.
[35] D.K. Patel, S.R. Kalidindi, Correlation of spherical nanoindentation stress-strain curves to simple compression stress-strain curves for elastic-plastic isotropic materials using finite element models, Acta Mater. 112 (2016) 295-302.
[36] S.-K. Kang, J.-H. Kim, Y.-H. Lee, J.-Y. Kim, D. Kwon, Correlation between the plastic strain and the plastic pileup of the instrumented indentation by utilizing the interrupted tensile test, Materials Science and Engineering: A 535 (2012) 197-201.
[37] Y.-C. Kim, S.-K. Kang, J.-Y. Kim, D. Kwon, Contact morphology and constitutive equation in evaluating tensile properties of austenitic stainless steels through instrumented spherical indentation, Journal of Materials Science 48(1) (2013) 232-239.
[38] S. Pathak, S.R. Kalidindi, Spherical nanoindentation stress–strain curves, Materials Science and Engineering: R: Reports 91 (2015) 1-36.
[39] B. Taljat, T. Zacharia, F. Kosel, New analytical procedure to determine stress-strain curve from spherical indentation data, International Journal of Solids and Structures 35(33) (1998) 4411-4426.
[40] J.-Y. Kim, K.-W. Lee, J.-S. Lee, D. Kwon, Determination of tensile properties by instrumented indentation technique: Representative stress and strain approach, Surface and Coatings Technology 201(7) (2006) 4278-4283.
[41] O.M. Kwon, J. Won, J.-h. Kim, C. Cho, E.-c. Jeon, D. Kwon, Effects of the Surface Contact on the Uncertainty in Indentation Yield Strength: Surface Roughness and Angular Misalignment, Metals and Materials International 25(6) (2019) 1500-1510.
[42] S.W. Jeon, K.W. Lee, J.Y. Kim, W.J. Kim, C.P. Park, D. Kwon, Estimation of

Fracture Toughness of Metallic Materials Using Instrumented Indentation: Critical Indentation Stress and Strain Model, Experimental Mechanics 57(7) (2017) 1013-1025.
[43] Y. Feng, T. Zhang, Determination of fracture toughness of brittle materials by indentation, Acta Mechanica Solida Sinica 28(3) (2015) 221-234.
[44] S. Carlsson, P.L. Larsson, On the determination of residual stress and strain fields by sharp indentation testing.: Part II: experimental investigation, Acta Materialia 49(12) (2001) 2193-2203.
[45] S. Carlsson, P.L. Larsson, On the determination of residual stress and strain fields by sharp indentation testing.: Part I: theoretical and numerical analysis, Acta Materialia 49(12) (2001) 2179-2191.
[46] S. Suresh, A.E. Giannakopoulos, A new method for estimating residual stresses by instrumented sharp indentation, Acta Materialia 46(16) (1998) 5755-5767.
[47] J.G. Swadener, B. Taljat, G.M. Pharr, Measurement of residual stress by load and depth sensing indentation with spherical indenters, Journal of Materials Research 16(7) (2001) 2091-2102.
[48] Q. Wang, K. Ozaki, H. Ishikawa, S. Nakano, H. Ogiso, Indentation method to measure the residual stress induced by ion implantation, Nuclear Instruments and Methods in Physics Research Section B: Beam Interactions with Materials and Atoms 242(1) (2006) 88-92.
[49] L. Xiao, D. Ye, C. Chen, A further study on representative models for calculating the residual stress based on the instrumented indentation technique, Computational Materials Science 82 (2014) 476-482.
[50] Z. Lu, Y. Feng, G. Peng, R. Yang, Y. Huan, T. Zhang, Estimation of surface equi-biaxial residual stress by using instrumented sharp indentation, Materials Science and Engineering: A 614 (2014) 264-272.
[51] Y.-H. Lee, D. Kwon, Estimation of biaxial surface stress by instrumented indentation with sharp indenters, Acta Materialia 52(6) (2004) 1555-1563.
[52] W.C. Oliver, G.M. Pharr, An improved technique for determining hardness and elastic modulus using load and displacement sensing indentation

experiments, Journal of Materials Research 7(6) (1992) 1564-1583.
[53] J. Alcalá, A.C. Barone, M. Anglada, The influence of plastic hardening on surface deformation modes around Vickers and spherical indents, Acta Materialia 48(13) (2000) 3451-3464.
[54] J. Alcalá, D. Esqué-de los Ojos, Reassessing spherical indentation: Contact regimes and mechanical property extractions, International Journal of Solids and Structures 47(20) (2010) 2714-2732.
[55] O. Bartier, X. Hernot, G. Mauvoisin, Theoretical and experimental analysis of contact radius for spherical indentation, Mechanics of Materials 42(6) (2010) 640-656.
[56] Y. Choi, H.-S. Lee, D. Kwon, Analysis of sharp-tip-indentation load–depth curve for contact area determination taking into account pile-up and sink-in effects, J. Mater. Res. 19(11) (2004) 3307-3315.
[57] S.-K. Kang, J.-Y. Kim, C.-P. Park, H.-U. Kim, D. Kwon, Conventional Vickers and true instrumented indentation hardness determined by instrumented indentation tests, J. Mater. Res. 25(2) (2010) 337-343.
[58] S.-K. Kang, Y.-C. Kim, J.-W. Lee, D. Kwon, J.-Y. Kim, Effect of contact angle on contact morphology and Vickers hardness measurement in instrumented indentation testing, International Journal of Mechanical Sciences 85 (2014) 104-109.
[59] V. Karthik, P. Visweswaran, A. Bhushan, D.N. Pawaskar, K.V. Kasiviswanathan, T. Jayakumar, B. Raj, Finite element analysis of spherical indentation to study pile-up/sink-in phenomena in steels and experimental validation, International Journal of Mechanical Sciences 54(1) (2012) 74-83.
[60] S.H. Kim, B.W. Lee, Y. Choi, D. Kwon, Quantitative determination of contact depth during spherical indentation of metallic materials—A FEM study, Materials Science and Engineering: A 415(1) (2006) 59-65.
[61] S.-H. Kim, E.-c. Jeon, D. Kwon, Determining Brinell Hardness From Analysis of Indentation Load-Depth Curve Without Optical Measurement, Journal of Engineering Materials and Technology 127(1) (2005) 154-158.
[62] S. Kucharski, Z. Mróz, Identification of plastic hardening parameters of

metals from spherical indentation tests, Materials Science and Engineering: A 318(1) (2001) 65-76.
[63] J. Malzbender, G. de With, Indentation load–displacement curve, plastic deformation, and energy, J. Mater. Res. 17(2) (2002) 502-511.
[64] F.R.S. R. Hill, B. Storakers, A. B. Zdunek, A theoretical study of the Brinell hardness test, Proceedings of the Royal Society of London. A. Mathematical and Physical Sciences 423(1865) (1989) 301.
[65] B. Taljat, G.M. Pharr, Development of pile-up during spherical indentation of elastic–plastic solids, International Journal of Solids and Structures 41(14) (2004) 3891-3904.
[66] M. Wang, J. Wu, Y. Hui, Z. Zhang, X. Zhan, R. Guo, Identification of elastic-plastic properties of metal materials by using the residual imprint of spherical indentation, Materials Science and Engineering: A 679 (2017) 143-154.
[67] A. Bolshakov, W.C. Oliver, G.M. Pharr, Influences of stress on the measurement of mechanical properties using nanoindentation .2. Finite element simulations, J. Mater. Res. 11(3) (1996) 760-768.
[68] T.Y. Tsui, W.C. Oliver, G.M. Pharr, Influences of stress on the measurement of mechanical properties using nanoindentation .1. Experimental studies in an aluminum alloy, J. Mater. Res. 11(3) (1996) 752-759.
[69] Y.-H. Lee, K. Takashima, Y. Higo, D. Kwon, Prediction of stress directionality from pile-up morphology around remnant indentation, Scripta Materialia 51(9) (2004) 887-891.
[70] M.-J. Choi, S.-K. Kang, I. Kang, D. Kwon, Evaluation of nonequibiaxial residual stress using Knoop indenter, Journal of Materials Research 27(1) (2012) 121-125.
[71] Y.-C. Kim, M.-J. Choi, D. Kwon, J.-Y. Kim, Estimation of principal directions of Bi-axial residual stress using instrumented Knoop indentation testing, Metals and Materials International 21(5) (2015) 850-856.
[72] J.-h. Kim, H. Xu, M.-J. Choi, E. Heo, Y.-C. Kim, D. Kwon, Determination of directionality of nonequibiaxial residual stress by nanoindentation testing using a modified Berkovich indenter, J. Mater. Res. 1-8.

[73] H. Xu, Evaluation of Non-equal Biaxial Residual Stress Using Modified Berkovich Indenter in Nano Scale, Seoul National University, Seoul, Republic of Korea, 2017.
[74] J.-H. Kim, Assessment of residual stress based on indentation surface displacement and evaluation of integrity for weldment considering residual stress, 압입표면 변위 분석 기반의 잔류응력 평가 및 잔류응력을 고려한 용접부 건전성 평가, 서울 : 서울대학교 대학원, 서울, 2019.
[75] D. Vangi, M. Ermini, Plasticity Effects in Residual Stress Measurement by the Hole Drilling Method, Strain 36(2) (2000) 55-59.
[76] A.H. Mahmoudi, C.E. Truman, D.J. Smith, M.J. Pavier, The effect of plasticity on the ability of the deep hole drilling technique to measure axisymmetric residual stress, International Journal of Mechanical Sciences 53(11) (2011) 978-988.
[77] C.E. Murray, Invariant x-ray elastic constants and their use in determining hydrostatic stress, Journal of Applied Physics 110(12) (2011) 123501.
[78] T. Gnäupel-Herold, A.A. Creuziger, M. Iadicola, A model for calculating diffraction elastic constants, Journal of Applied Crystallography 45(2) (2012) 197-206.
[79] G.S. Schajer, M.B. Prime, Use of Inverse Solutions for Residual Stress Measurements, Journal of Engineering Materials and Technology 128(3) (2006) 375-382.
[80] S.-K. Kang, J.-Y. Kim, C.-P. Park, H.-U. Kim, D. Kwon, Conventional Vickers and true instrumented indentation hardness determined by instrumented indentation tests, Journal of Materials Research 25 (2010).

Chapter 3

THEORITICAL MODELING

Contents

3.1. Motivation and Research Flow 58

3.1.1. Introduction 58

3.1.2. FEA simulation approach 61

3.2. Phenomenological Modeling 64

3.2.1 Maximum stress sensing depth 64

3.2.2. Calibration coefficient 68

3.3 Evaluation of through-thickness residual stress 71

3.3.1. Theoretical modeling 71

3.3.2. Computational verification 75

3.3.3. Discussion 76

References 101

3.1. Motivation and Research Flow

3.1.1. Introduction

The indentation force-displacement curve shifted with the presence of residual stress, indentation force at the same indentation displacement varies depending on the sign and the magnitude of residual stress within the materials [1-6]. The average of plane residual stress can be calculated from the changes in indentation curve, force difference, using sharp indenter [3-6]. Introduction of two-fold rotational symmetric and mirror symmetric indenter or combination with digital image correlation makes the decomposition of plane stress component. However, the stress estimated by using the models proposed previously assume the uniform stress distribution through the thickness of materials.

Most of all components underwent processing has non-uniform stress distribution through the thickness of materials. The slope of indentation loading curve changes with the through-thickness stress state, which may result in the variation of force differences with increasing indentation displacement. The force difference at the uniform stress state may increase proportionally with contact area and square of the indentation displacement. Therefore, the evaluated stress using indentation at uniform stress distribution is almost constant excepting the beginning stage of the loading curve, where the effect of indenter bluntness is dominant. However, indentation stress at non-uniform stress state varies with the stress through the thickness. The obtained stress is not the stress at the maximum indentation displacement, nor the average of stress down to the maximum indentation displacement due to geometry of sharp indenter. The indentation stress involves with the stress distribution down the maximum sensing depth of indentation. The contributions of stresses at the surface and at the maximum sensing depth are reasonably inferred to be different due to the contact of sharp indenter increases proportional to the square of indentation displacement. Based on continuous force-displacement curve, instrumented indentation testing is advantageous technique to evaluate through-thickness residual stress, however, estimation of through-thickness stress has not been carried out.

In this study, the effect of stress through the thickness on the indentation force-displacement curve was investigated. Stepwise-constant stress distribution is desirable to identify the accurate contribution of the stress by depth. Experimental known stress distribution is usually applied for verification or comparison of stress measurement methods, for example, stress by applying elastic or elastoplastic stress [7, 8]. However, stress distribution of mechanically applied stress cannot develop the step-wise constant stress distribution, which is improper to be utilized when the measuring depth and the contribution of stress are both unknown. The stress distribution developed by mechanical way is difficult to be controlled freely due to self-equilibrium character of residual stress. Therefore, this study used the step-wise constant thermal stress distribution through the finite element analysis, which is efficient to determine the maximum stress sensing depth and contribution of stress at each depth to indentation force-displacement curve. Conical indenter with apex angle of 70.3° as shown in Fig. 3.1 was modeled which have same geometrical contact area with Vickers indenter at the same maximum indentation displacement. Conical indenter, rotational symmetric sharp indenter, was used taking advantage of negligible sensitivity on rotation of indenting axis, unlike Vickers or Berkovich indenter, for non-equibiaxial stress state. This study is based on Lee and Kwon's model for evaluation of the residual stress magnitude.

3.1.2. FEA simulation approach

Finite element analysis (FEA) was performed using the general purpose commercial software ABAQUS. 2-D axisymmetric model was used. Conical indenter was modeled as discrete rigid body assuming the perfectly rigid solid. Interaction between rigid conical indenter and deformable specimen was modeled as “Surface-to-surface contact” and the friction coefficient was applied. The power-law hardening solid was modeled using 14653 of 4-node bilinear axisymmetric quadrilateral elements for deformable specimen with minimum mesh size of 0.0005. Specimen was partitioned by the 20 datum planes with intervals of 80 from the surface as shown in Figure 3.1. FEA conical indentations at the maximum indentation displacement of 100 μm was compared with experimental indentation force displacement curve for the 304 austenitic stainless steel and the curve is well matched as shown in Figure 3.2. The mechanical properties including elastic modulus, Poisson's ratio, plastic stress-strain points were input obtained from uniaxial tension test of the materials.

Predefined temperature field and boundary condition were applied for developing the step-wise constant stress distribution. Controlling the thermal expansion coefficient (α) for the sections of materials makes the thermal strain resulting from the predefined temperature constantly applied for the all sections; set the α as zero for the zero-stress region and set the α of non-zero value for the stress applying region. Boundary conditions was given to constraint the lateral expansion of material resulting in the equi-biaxial thermal stress σ_T as Eq. (3-1), when the applied temperature is T.

$$\sigma_T = -\frac{T \cdot \alpha \cdot E}{(1-\upsilon)} \tag{3-1}$$

Compressive stress applied, when a positive temperature condition applied for the material with positive α, due to thermal expansion was suppressed. Tensile stress can be applied, reversely, by changing the sign of α or temperature. The Figure 3.3 shows simple examples of thermal stress distribution using introduced predefined condition and boundary conditions. Y-displacement constraint boundary condition was applied for top surface at the step to apply thermal stress to maintain the distance from indenter and surface of material. The boundary condition was deactivated and same constraint applied for the bottom surface of specimen at the indenter moving step. The verification of thermally induced stress model was conducted by comparing the indentation curve ($h_{max} = 100$) at the stressed state applied by mechanical pressure as in Figure 3.4. The force-displacement curves obtained by two different stress applying methods were perfectly matched in all stress state. This approach can be expanded to non-equibiaxial through-thickness stress distribution by controlling the boundary constraint and the anisotropy of thermal expansion coefficient.

3.2. Phenomenological modeling

3.2.1. Maximum stress sensing depth

The maximum depth of stress influencing the indentation force-displacement curve was studied by Zhao et al, by analyzing the loading curvature of indentation loading curve (C) with assumption that force is displacement to the power of two, called Kick's law ($\mathrm{F} = C\mathrm{h}^2$) [9]. The approach investigated the critical thickness of residual stress, which were investigated to be varied with various mechanical properties. However, the loading curvature represents the average changes of loading curve, therefore, there is limitation to separate the stress effect on indentation curve by displacement accurately. Moreover, indentation curves of real materials do not follow the Kick’s law, the value of power is also unknown for the measurement by test.

In this current study, effect of stress through the thickness on indentation curve, specifically on force difference at unit indentation displacement comparing with zero-stress state, was investigated by indentation simulations on the specimen with increasing the stressed depth.

Figure 3.5. shows schematic diagrams of indentation simulations for step-wise constant stress distributed specimen performed with the method introduced in 3.1.2. The schematic diagram of expected variation in indentation curve is represented in Figure 3.6, for the cases of stress depth increases down to 1000 μm, ten times of h_{max}. If the tensile residual stress is applied, the indentation curve may be shifted down comparing with stress-free state curve. The force difference at the h_{max} will be increased, however, the amount of force difference changes by additional stressed increment can be reasonably inferred to decrease as the distance from the indentation increases. The cumulative force difference comparing with stress-free curve (ΔF) with stressed depth from surface ($h_{stressed}$) is schematically represented as in Figure 3.7. The stress state far beneath the region deformed by indentation, over ten times of (h_{max}) would rarely affect the ΔF, therefore, the cumulative ΔF-$h_{stressed}$ will be saturated as in Figure 3.7. Indentation simulations by FEA were performed for the materials with artificial mechanical properties of E=200 GPa, $\varepsilon_y = 0.003$, $\nu = 0.3$, n=0.3 with increasing stress depth at intervals of 80 μm down to 1600 μm. The 300 MPa tensile stress, 50% of yield strength calculated from Eq. (3-1), was applied for the stressed region. Figure 3.8. shows the

thermal stressed specimen for indentation simulations and $\Delta\mathrm{F}$-$h_{stressed}$ curve. The $\Delta\mathrm{F}$ for the full depth stressed specimen was 129 N and the specimen with stressed depth of about 1000 μm was 125 N, 97 % of saturated $\Delta\mathrm{F}$.

Sharp indenter has geometrically self-similarity, the aspect ratio is maintained as the indenting displacement increases, therefore, the contribution of stress through the thickness of material is reasonably inferred to be same regardless the magnitude of indentation displacement unlike the incremental hole-drilling. For the case of incremental hole-drilling stress measurement the hole diameter is fixed while the hole depth increases as in Figure 2.3. However, sharp indenter including conical, Vickers and Berkovich indenters maintains the geometric congruence in the ratio between the indentation displacement and stress sensing depth independent with indentation displacement as in Figure 3.9. The contribution of stress through the thickness on indentation force-displacement curve can be normalized by indentation force and displacement based on the advantage of geometrical self-similarity. For example, ΔF - $h_{stressed}$ curves can be obtained differently from the indentation simulations at double scaled condition as in Figure 3.10. Two different ΔF-$h_{stressed}$ obtained from double-scaled h_{max} and stressed depth can be normalized as one normalized $\Delta \mathrm{F}$-$h_{stressed}$ curve by normalizing the ΔF by the maximum force of stress-free state or by ΔF_{max}, which is the saturated value of ΔF, and the $h_{stressed}$ by h_{max}. The schematic diagram of procedure is represented in Figure 11. The curves of indentation cumulative ΔF with increasing stressed depth at different indentation displacement are represented in Figure 3.12, showing the different saturation depth of ΔF. The maximum stress sensing depth, which indicates the maximum depth of stress that affects the indentation force at each indentation displacement, increases as the h_{max} increases. Figure 3.12. shows that the ΔF-$h_{stressed}$ curve at ten different indentation displacement are normalized as a single curve. The value of $\Delta F/F_{max,0}$, when $h_{stressed}/h_{max}$ is 10, was 0.163, 97% of saturated value. The maximum stress sensing depth of indentation was assumed as ten times of indentation displacement based on the FEA results; most of ΔF is generated by the stress within the depth of ten times of h_{max}.

3.2.2. Calibration coefficient

Effect of stress through the thickness of materials can be estimated by analyzing the $\Delta F\,/\Delta F_{max}$ - $h_{stressed}/h_{max}$ curve. The differences between the cumulative force differences obtained from indentation results with increasing stressed depth represents the contribution of additional applied stress. For example, red points in Figure 3.7 show the $\Delta F/\Delta F_{max}$-$h_{stressed}/h_{max}$ points when the maximum stress sensing depth divided into four layers. The contribution of stress at each layer on ΔF can be represented as Figure 3.13, when the $\Delta F_{i/4}$ represents the cumulative force difference from specimen stress applied from surface to i^{th} layer. Total number of layers can be determined with larger value if the $\Delta F\,/\Delta F_{max}$ - $h_{stressed}/h_{max}$ curve is obtained precisely. Therefore, the contribution of i^{th} layer on ΔF among n layers dividing the maximum stress sensing depth can be calculated by the difference between $\Delta F_{i/n}$ and $\Delta F_{i-1/n}$, when $\Delta F_{i/n}$ is defined as cumulative force difference of specimen stress applied down to i^{th} layer from surface among n layers dividing the maximum stress sensing depth. This approach is based on the assumption that the increment of force difference generated by the stress of i^{th} layer, $\Delta F_{n,i}$, is independent on the stress at other layers.

The independency of $\Delta F_{n,i}$ on the stress at other layers excepting i^{th} layer can be verified by comparing the $\Delta F_{n,i}$ obtained from the difference between cumulative $\Delta F_{i/n}$ and $\Delta F_{i-1i/n}$ with ΔF measured at the specimen stressed at just i^{th} layer as shown in schematic diagram of Figure 3.14. The contribution of the stress at i^{th} layer on the force difference, calculated from cumulative $\Delta F_{i/n}$ and $\Delta F_{i-1/n}$, is indicated in red points and $\Delta F_{n,i}$ measured on the specimen stressed at just i^{th} layer is indicated in blue points in Figure 3.15. Each calculated and measured line is perfectly overlapped, which means the force difference generated by the layer stress is not changed by the presence of stress at other layers. The independency of the layer stress contribution on force difference, $\Delta F_{n,i}/\Delta F_{max}$, yields the applicability of indentation for evaluating the non-uniform residual stress distribution.

Calibration coefficient ($\beta_{n,i}$) of i^{th} layer to calibrate the indentation force difference, the contribution of layer stress on total force difference, can be represented as Eq. (3-2), when the maximum stress sensing depth is divided into n layers.

$$\beta_{n,i} = \frac{\Delta F_{i/n} - \Delta F_{i-1/n}}{\Delta F_{max}} = \frac{\Delta F_{n,i}}{\Delta F_{max}} \tag{3-2}$$

The calibration coefficient represents the ratio of force difference generated by the stress applied to full sensing depth and by the stress applied to i^{th} layer. Cumulative coefficient and calibration coefficient for the materials with mechanical properties of $\varepsilon_y = 0.003$, $\mathrm{n} = 0.3$, $\upsilon = 0.3$ are summarized in Tables 3.1 and 3.2.

3.3. Evaluation of through-thickness residual stress

3.3.1. Theoretical modeling

Stress of i^{th} layer can be calculated by multiplying $\beta_{n,i}$ to the $\Delta F_{n,i}$, and dividing by A_c as Eq. (3-3), which become identical form with sum of Eqs. (2-18) and (2-19).

$$\frac{\Delta F_{n,i}}{\beta_{n,i}} \cdot \frac{3}{A_c} = \frac{3 \cdot \Delta F_{max,i}}{A_c} = \sigma_i \tag{3-3}$$

Consequently, the stress of i^{th} layer can be evaluated, if the $\Delta F_{n,i}$ is separated from total ΔF and A_c is estimated.

Evaluation of non-uniform residual stress through the thickness with an indentation force-displacement curve is proceeded with sequential process. The sequence of through-thickness stress evaluation will be explained with an example of situation with four layers dividing the stress sensing depth developed at the maximum indentation displacement. The schematic diagram of indentation at four displacements by step and the indentation curve are represented in Figure 3.16. The force difference at intermediate h_i, can be expressed by the summation of the force differences generated by each layer stress within the maximum stress sensing depth as Eqs. from (3-4) to (3-7) based on the independency of layer stress contribution.

$$\Delta F_1 \ = \Delta F_{1,1} \tag{3-4}$$

$$\Delta F_2 \ = \Delta F_{2,\,1} + \Delta F_{2,\,2} \tag{3-5}$$

$$\Delta F_3 \ = \Delta F_{3,\,1} + \Delta F_{3,\,2} + \Delta F_{3,\,3} \tag{3-6}$$

$$\Delta F_4 \ = \Delta F_{4,\,1} + \Delta F_{4,\,2} + \Delta F_{4,\,3} + \Delta F_{4,\,4} \tag{3-7}$$

The force difference at h_1, the displacement developing the sensing depth equal to the unit layer thickness, is entirely the effect of the first layer stress (σ_1). Therefore, the stress can be evaluated directly by the ΔF_1 assuming the uniform stress condition. On the other hands, evaluation of the following layer stresses, excepting the first layer, requires the separation of contribution by the stress at previous layers. For example, the total force difference at h_2, ΔF_2, is generated by the layer stresses at the first and second unit depth. Extraction of $\Delta F_{2,2}$, the contribution of the second layer stress, in ΔF_2 is required for evaluation of σ_2.

The ratio of force difference and the maximum force is constant when the stress is fixed independent with indentation displacement due to geometrical self-similarity of sharp indenter. Contact area and maximum indentation force are linear relation for indentation displacement range that the indentation size effect disappeared due to bulk hardness of material is constant [10]. The hardness calculated from maximum indentation force and real contact area is also invariant with residual stress [11]. The force difference between uniform-stressed curve and stress-free curve is proportional to contact area regardless indentation displacement based on the proposed formula of indentation stress [1, 6]. It can be also be inferred from the experimental results in previous studies that the exponents of loading curves are almost constant regardless of stress state [4, 5]. Therefore, force difference and indentation force at the same displacement has proportional relation, in other words, ratio of force difference and indentation force is constant. The constant ratio can be applied at non-uniform stress distribution with calibration coefficient and the $\Delta F_{\mathrm{max,i}}$ representing the maximum force difference generated when the i^{th} layer stress is uniformly distributed over the entire depth. The force ratio can be expressed by the Eqs. from (3-4) to (3-7).

$$\frac{\Delta F_{max,1}}{F_{max}} = \frac{\Delta F_{1,1}}{F_1} = \frac{\Delta F_{2,1}}{F_2}\frac{1}{\beta_{2,1}} = \frac{\Delta F_{3,1}}{F_3}\frac{1}{\beta_{3,1}} = \frac{\Delta F_{4,1}}{F_4}\frac{1}{\beta_{4,1}} \tag{3-8}$$

$$\frac{\Delta F_{max,2}}{F_{max}} = \frac{\Delta F_{2,2}}{F_2}\frac{1}{\beta_{2,2}} = \frac{\Delta F_{3,2}}{F_3}\frac{1}{\beta_{3,2}} = \frac{\Delta F_{4,2}}{F_4}\frac{1}{\beta_{4,2}} \tag{3-9}$$

$$\frac{\Delta F_{max,3}}{F_{max}} = \frac{\Delta F_{3,3}}{F_3}\frac{1}{\beta_{3,3}} = \frac{\Delta F_{4,3}}{F_4}\frac{1}{\beta_{4,3}} \tag{3-10}$$

$$\frac{\Delta F_{max,4}}{F_{max}} = \frac{\Delta F_{4,4}}{F_4}\frac{1}{\beta_{4,4}} \tag{3-11}$$

Dividing $\Delta F_{n,i}$ by calibration coefficient ($\beta_{n,i}$) represents $\Delta F_{max,i}$ at h_n. The force difference resulting from σ_1 at each indentation displacement can be calculated using Eq. (3-8) with $\Delta F_{1,1}$ ($= \Delta F_1$). Substituting the calculated $\Delta F_{2,1}$ into Eq. (3-5) enables the calculation of $\Delta F_{2,2}$. In the same way as the first layer, force difference resulting from σ_2 at each indentation displacement can be obtained using Eq. (3-9) followed by substitution $\Delta F_{3,2}$ and $\Delta F_{4,2}$ in Eqs. (3-6) and (3-7). From $\Delta F_{2,2}$ to $\Delta F_{4,4}$ can be obtained as Eqs. from (3-12) to (3-14), and generalized form of $\Delta F_{i,i}$ can be expressed as in Eq. (3-15).

$$\Delta F_{2,2} = \Delta F_2 - \frac{F_2}{F_1} \cdot \beta_{2,1} \cdot \Delta F_1 \tag{3-12}$$

$$\Delta F_{3,3} = \Delta F_3 - \left(\frac{F_3}{F_1} \cdot \beta_{3,1} \cdot \Delta F_1 + \frac{F_3}{F_2} \cdot \frac{\beta_{3,2}}{\beta_{2,2}} \cdot \Delta F_{2,2}\right) \tag{3-13}$$

$$\Delta F_{4,4} = \Delta F_4 - \left(\frac{F_4}{F_1} \cdot \beta_{4,1} \cdot \Delta F_1 + \frac{F_4}{F_2} \cdot \frac{\beta_{4,2}}{\beta_{2,2}} \cdot \Delta F_{2,2} + \frac{F_4}{F_3} \cdot \frac{\beta_{4,3}}{\beta_{3,3}} \cdot \Delta F_{3,3}\right) \tag{3-14}$$

$$\Delta F_{i,i} = \Delta F_i - \left(\sum_{k=1}^{i-1} \frac{F_i}{F_k} \cdot \frac{\beta_{i,k}}{\beta_{k,k}} \cdot \Delta F_{k,k} \right) \tag{3-15}$$

The stress through the thickness can be calculated as Eq. (3-16)

$$\sigma_i = \frac{3 \cdot \Delta F_{i,i}}{\beta_{i,i} \cdot A_i} = \frac{3}{\beta_{i,i} \cdot A_i} \left(\Delta F_i - \left(\sum_{k=1}^{i-1} \frac{F_i}{F_k} \cdot \frac{\beta_{i,k}}{\beta_{k,k}} \cdot \Delta F_{k,k} \right) \right) \tag{3-16}$$

Consequently, the non-uniform stress can be simplified as matrix notation as in Eq. (3-17) with indentation force difference at each indentation displacement.

$$[\boldsymbol{\sigma}] = \mathbf{3} \cdot [\boldsymbol{\beta}]^{-\mathbf{1}} \cdot [\boldsymbol{A}] \cdot [\Delta \boldsymbol{F}] \tag{3-17}$$

3.3.2. Computational verification

Computational evaluations were performed to verify the availability of the proposed method for evaluating the arbitrary stress distribution. Non-uniform stress distribution was made by the method introduced in 3.1.2. Two applied stress distribution, stress normalized by yield strength and applied depth, were utilized for the verification, and the profiles are summarized in Table 3.3. The maximum sensing depth (=1 mm) was divided into eight layers. Figure 3.17 shows the stress depth-profiling results of material with artificial mechanical properties of $\varepsilon_y = 0.003$, $n = 0.3$, $\upsilon = 0.3$. The trends of stress through the thickness matched well with applied distribution in all depth. However, the initial data for the second stress profile with $n = 0.2$ shows large error over 150 MPa (Figure 3.18). Figures 3.19 and 3.20 are evaluated results for the materials which were used for experimental verification test, C1220 and S420J2. For the both cases of profile, the values are significantly underestimated and trends are not matched.

3.3.3. Discussion

The error analysis of evaluated results from FEA was performed in terms of (1) conventional stress evaluation model and (2) stress sensing depth. Error for the early stage estimated data, points less than 0.2 mm deep, is rarely influenced by stress profiling procedure. It is the error resulted from the model proposed by Lee and Kwon [4, 6]. The model estimates good tendency of stress distribution of material, however, it has limitation for accurate evaluation of magnitude due to the different stress sensitivity depending on mechanical properties and sign of stress [12, 13]. The only factor regarding the material dependency in the model is contact area, on the other hand, the stress sensitivity varies with mechanical properties such as elastic modulus, yield strength, Poisson's ratio and strain hardening exponent.

The stress sensing depth was assumed as ten times of the indentation displacement in this chapter of thesis based on FEA results for the reference material ($\mathrm{E} = 200$ GPa, $\varepsilon_y = 0.003,\ \nu = 0.3,\ n = 0.3$). The proportion of force difference by the stress within the sensing depth was 97% comparing to the difference of full-depth stressed case. However, the approximation of sensing depth may generate error when the depth is far deeper or shallower than ten times of indentation displacement. Furthermore, the location of estimated stress through the thickness shall be corrected if the depth varies with mechanical properties of material.

The proposed method in this chapter of thesis can evaluate the trend of through-thickness residual stress well for some materials. However, correction of stress sensitivity for conventional stress evaluation model and stress sensing depth in consideration of material dependency shall be performed for accurate estimation of magnitude and depth of stress through the thickness.

Table 3.1. Cumulative coefficient of reference material (E=200 GPa, $\sigma_Y/E=0.003$, n=0.3, υ=0.3)

n \ i	1st	2nd	3rd	4th	5th	6th	7th	8th	9th	10th
1	1.000									
2	0.590	1.000								
3	0.385	0.775	1.000							
4	0.284	0.590	0.854	1.000						
5	0.225	0.468	0.704	0.896	1.000					
6	0.186	0.385	0.590	0.775	0.921	1.000				
7	0.159	0.327	0.503	0.673	0.822	0.937	1.000			
8	0.139	0.284	0.437	0.590	0.732	0.854	0.948	1.000		
9	0.124	0.251	0.385	0.522	0.654	0.775	0.878	0.956	1.000	
10	0.112	0.225	0.344	0.468	0.590	0.704	0.808	0.896	0.962	1.000

Table 3.2. Calibration coefficient of reference material (E=200 GPa, σ_Y/E=0.003, n=0.3, υ=0.3)

n \ *i*	1st	2nd	3rd	4th	5th	6th	7th	8th	9th	10th
1	1.000									
2	0.590	0.410								
3	0.385	0.390	0.225							
4	0.284	0.306	0.265	0.146						
5	0.225	0.243	0.237	0.192	0.104					
6	0.186	0.199	0.204	0.186	0.146	0.079				
7	0.159	0.167	0.176	0.170	0.149	0.115	0.063			
8	0.139	0.144	0.153	0.153	0.142	0.123	0.093	0.052		
9	0.124	0.127	0.135	0.137	0.132	0.121	0.103	0.078	0.044	
10	0.112	0.113	0.120	0.123	0.122	0.115	0.104	0.088	0.066	0.038

Table 3.3. Applied stress profile for computational verification

Depth (mm)	σ_{RS}/σ_{YS}	
	Profile #1	Profile #2
0.04	0.75	-0.75
0.12	0.8	-0.8
0.2	0.75	-0.85
0.28	0.65	-0.75
0.36	0.55	-0.55
0.44	0.45	-0.45
0.52	0.25	-0.25
0.6	0.05	-0.05
0.68	0	0
0.76	-0.05	0
0.84	-0.1	0.05
0.92	-0.45	0.2
1	-0.5	0.25

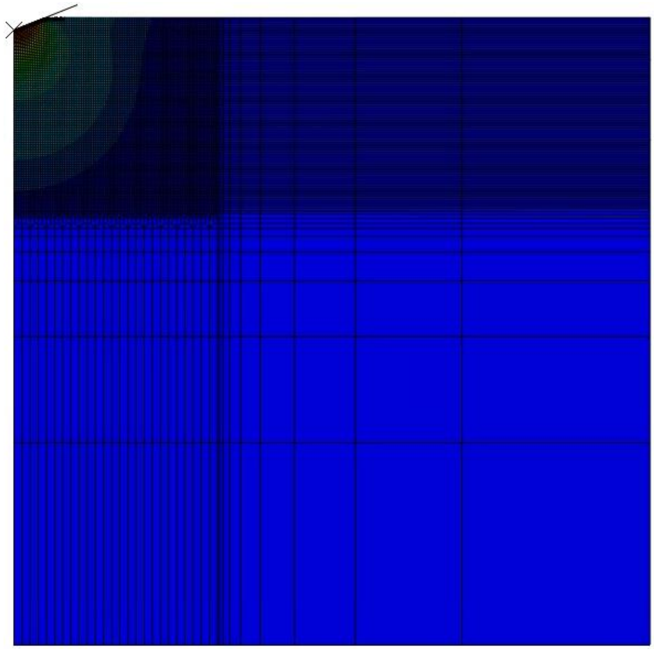

Figure 3.1. 2-D conical indentation simulation using ABAQUS

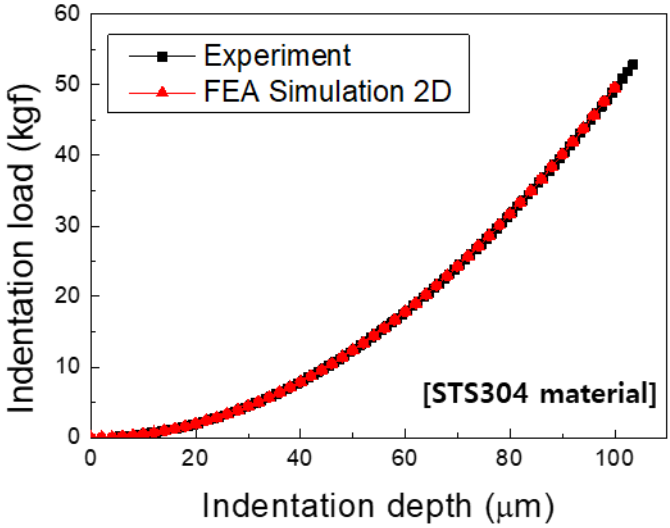

Figure 3.2. Comparison of indentation curves obtained from experiment and FEA simulation for STS304 steel

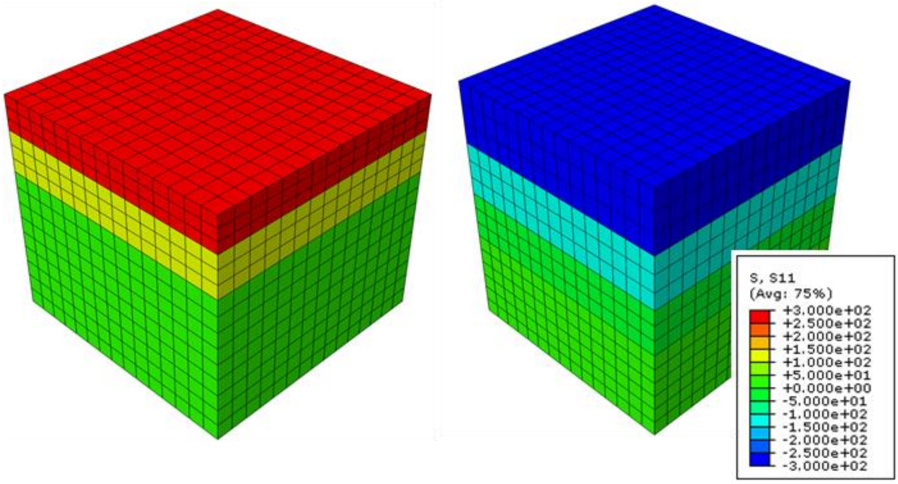

(a) stress applied by heating (b) stress applied by cooling

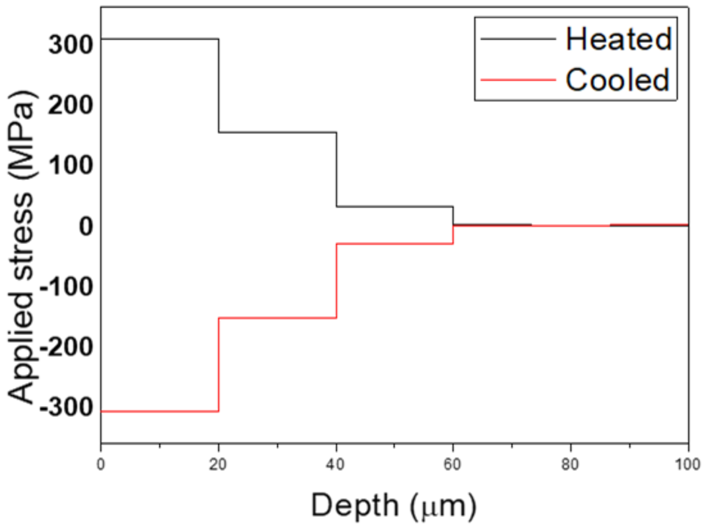

(c) Stress distribution of (a) and (b)

Figure 3.3. Example of step-wise constant stress distribution by controlling boundary conditions and thermal expansion coefficient

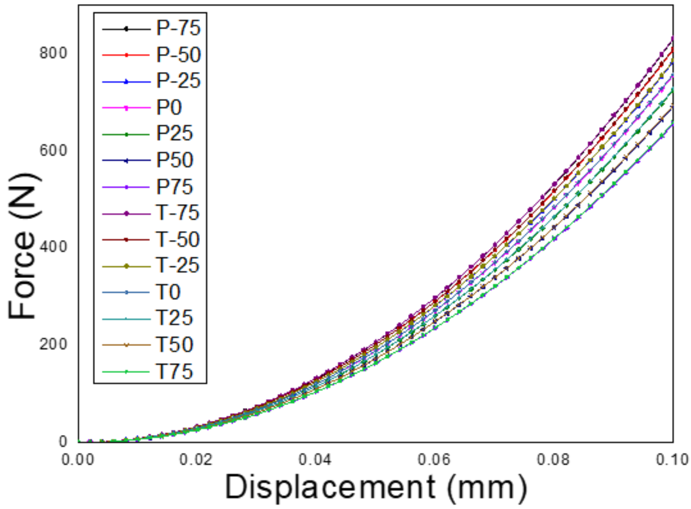

(a) Full-loading curve

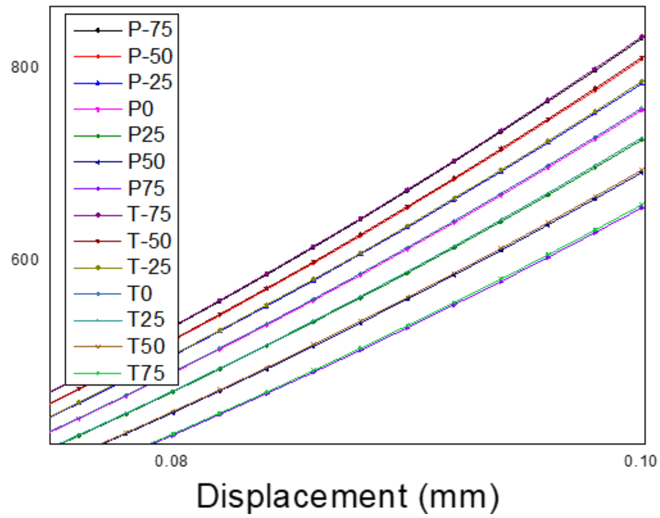

(b) Enlarged image of (a) around the maximum indentation force

Figure 3.4. Comparison of indentation curves with variation of stress applied by mechanical and thermal methods

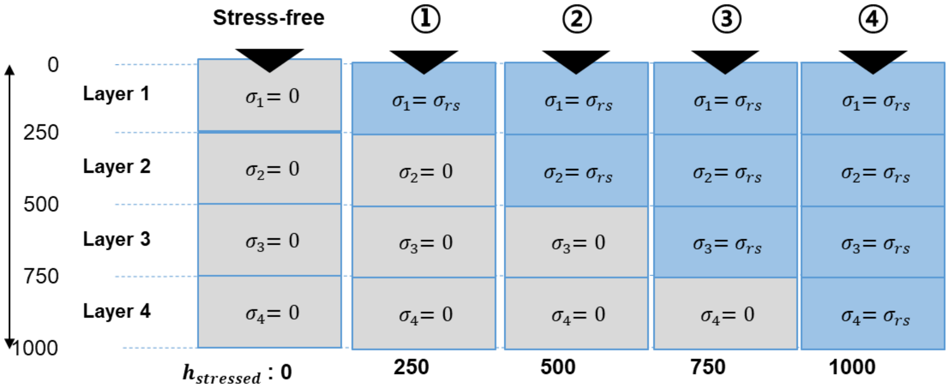

Figure 3.5. Schematic diagram of indentation simulations with increasing stressed depth at fixed maximum displacement

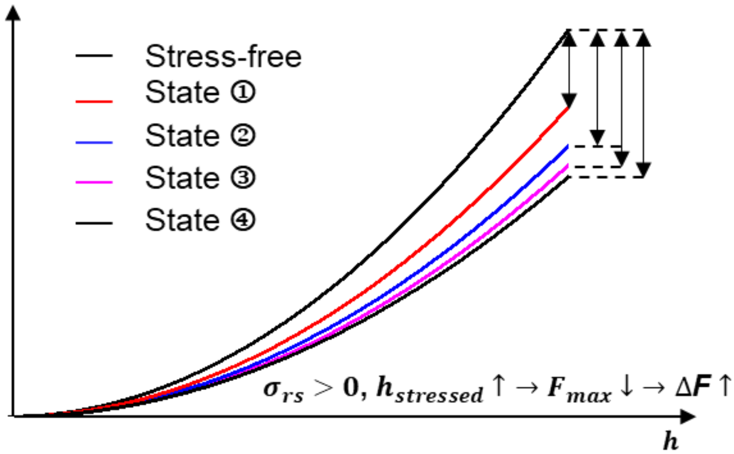

Figure 3.6. Expected variation of indentation curves with increasing stressed depth

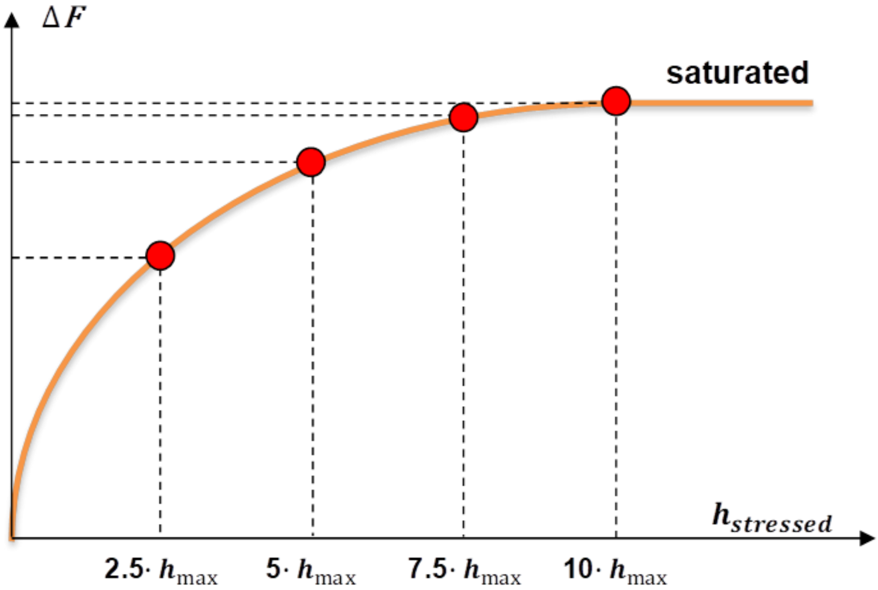

Figure 3.7. Schematic diagram of cumulative ΔF - $h_{stressed}$ curve

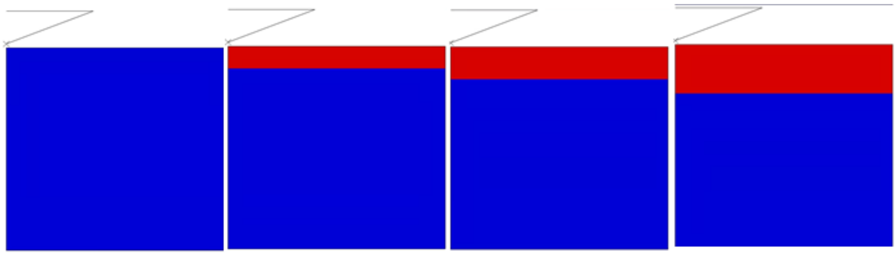

(a) Indentation with increasing stressed depth using FEA

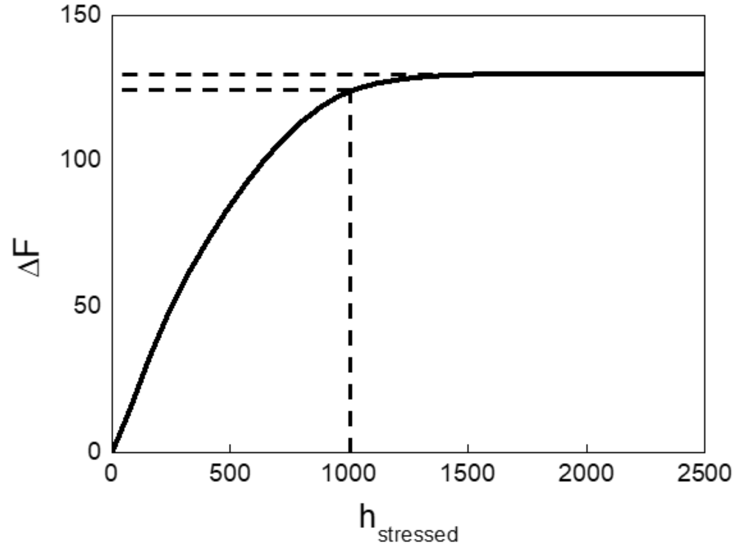

(b) ΔF - $h_{stressed}$ curve obtained from FEA

Figure 3.8. Saturation of force difference with increasing the depth of step-wise constant stress

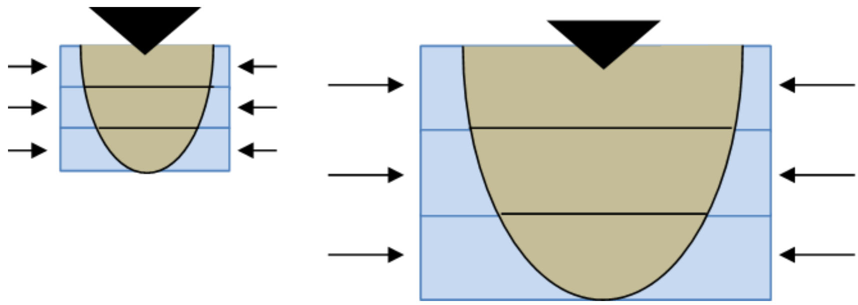

Figure 3.9. Identical ratio of stress depth to indentation displacement based on geometrical self-similarity of sharp indenter

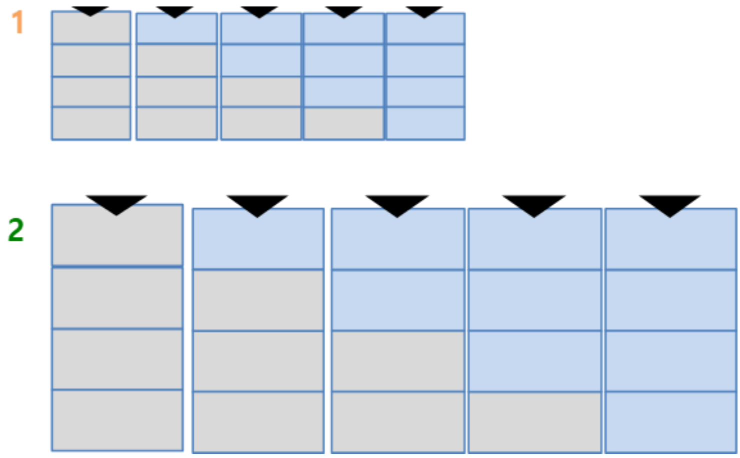

Figure 3.10. Identical layer contribution of force difference based on geometrical self-similarity of sharp indenter, when blue and gray indicate stressed and stress-free states

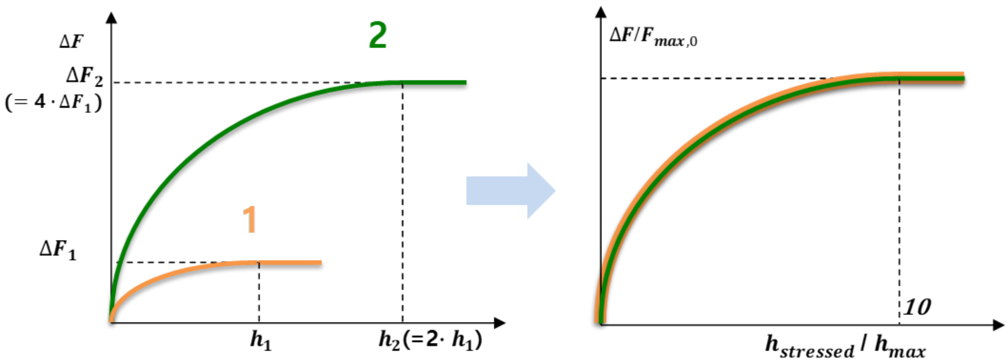

Figure 3.11. Schematic diagram of normalization process for cumulative ΔF - $h_{stressed}$ curve obtained at different indentation displacements

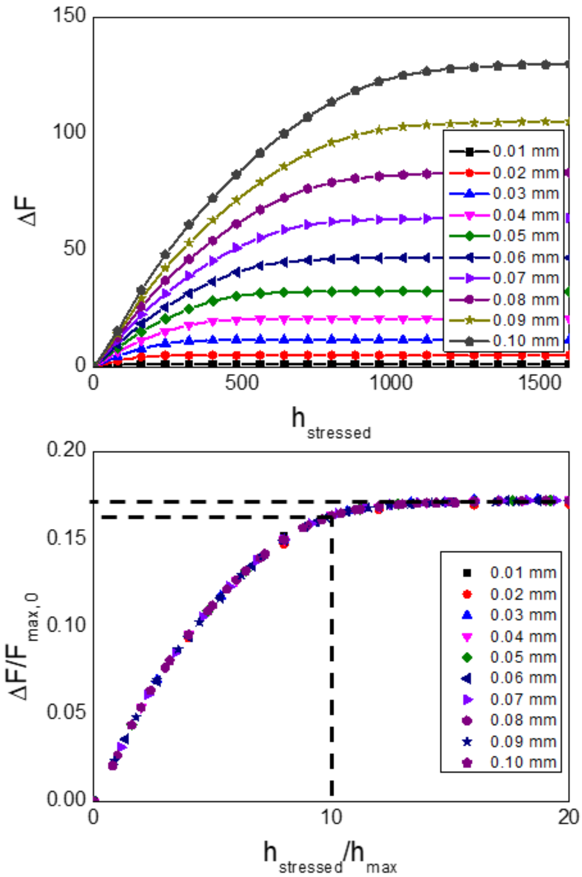

Figure 3.12. Normalization process for cumulative ΔF - $h_{stressed}$ curve obtained at ten different indentation displacements using FEA

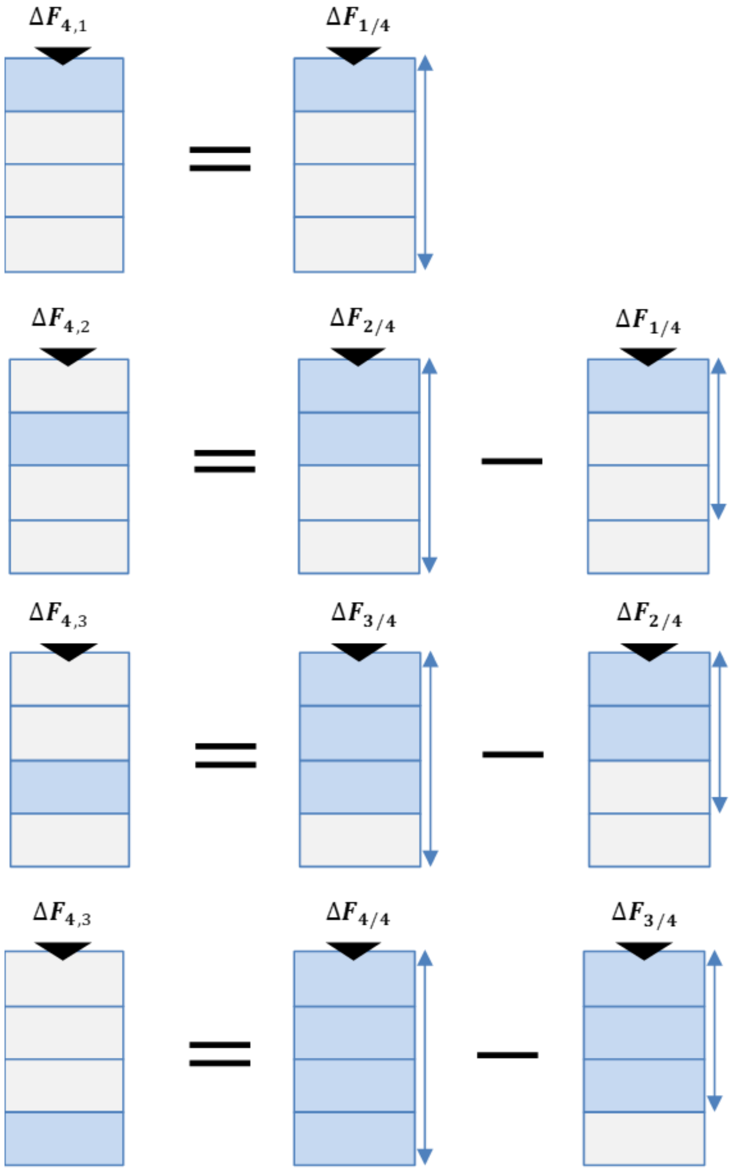

Figure 3.13. Definition of the force differences generated by layer stress and cumulative stress when blue and gray indicate stressed and stress-free states

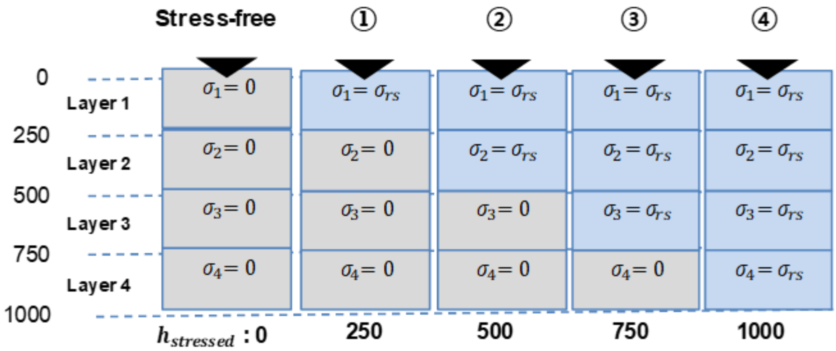

(a) Indentation on cumulative stressed specimen

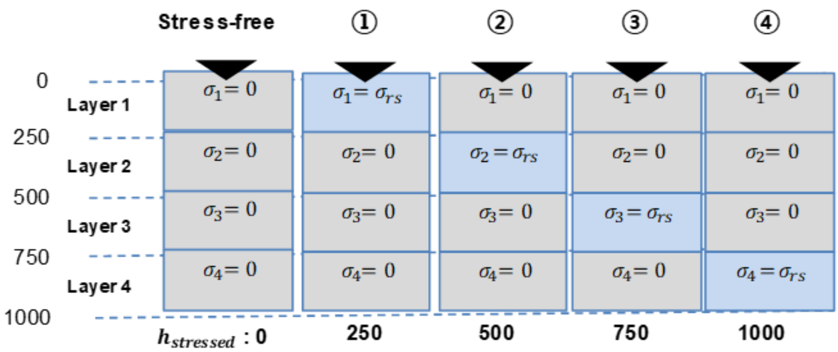

(b) Indentation on single stressed specimen

Figure 3.14. Schematic diagram of performed simulations to verify the force difference independency on the other layer stress

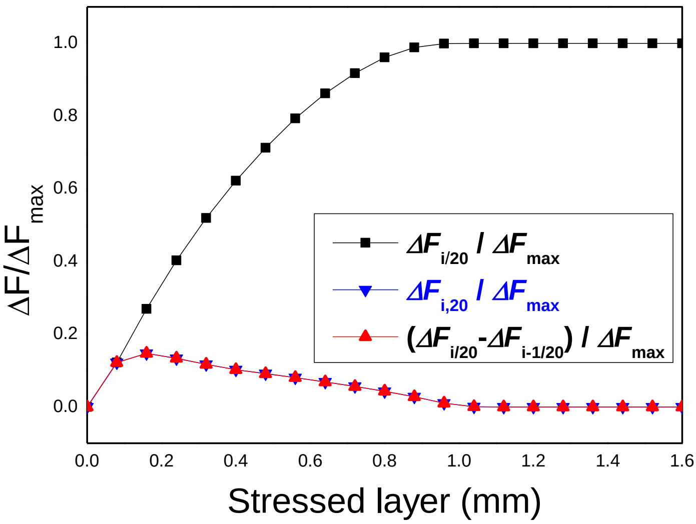

Figure 3.15. Comparison of stress contribution obtained from cumulative stressed depth and the contribution from single stressed depth indentation

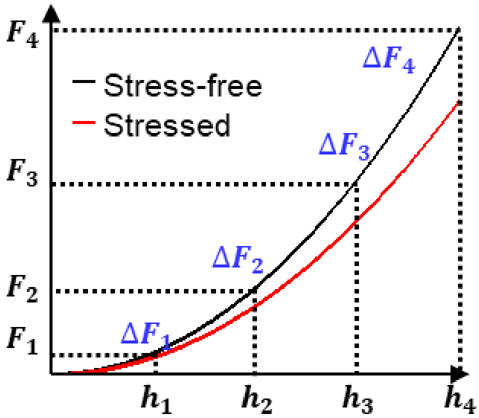

(a) Force differences by indentation displacements

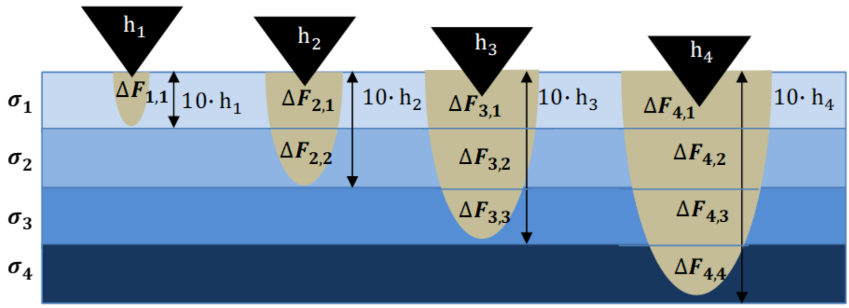

(b) Contribution of layer stresses on the force differences

Figure 3.16. Indentation test for non-uniform stress state

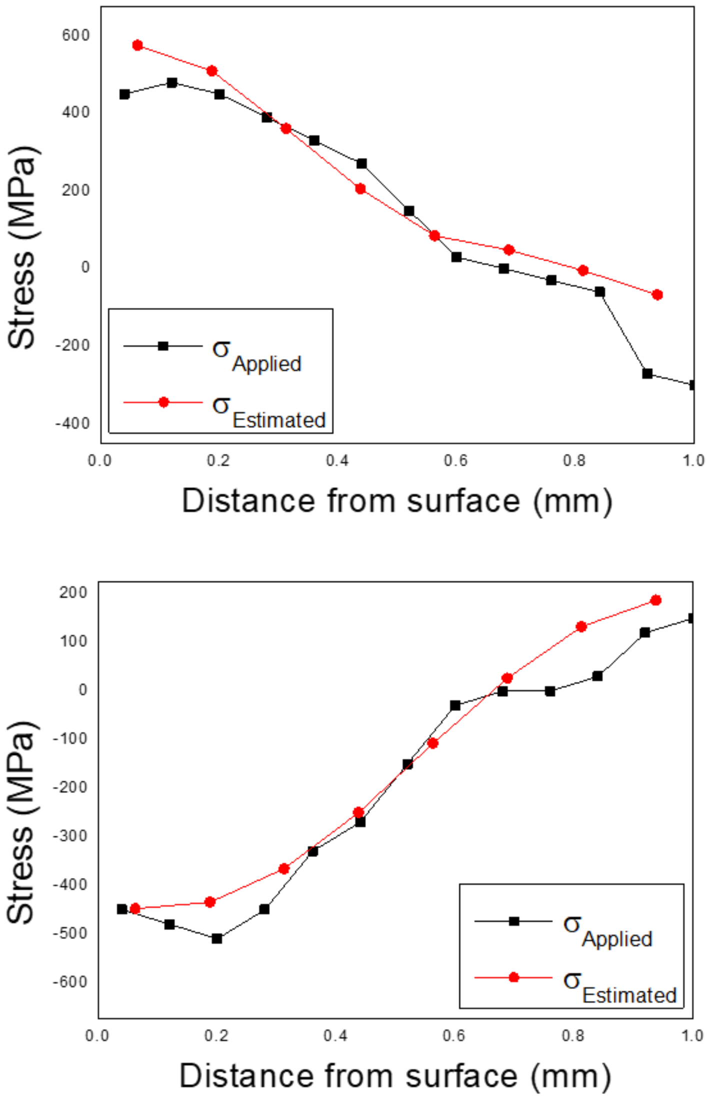

Figure 3.17. Computational verification results of reference material for (a) profile #1, (b) profile #2 (E=200 GPa, σ_Y/E=0.003, n=0.3, υ=0.3)

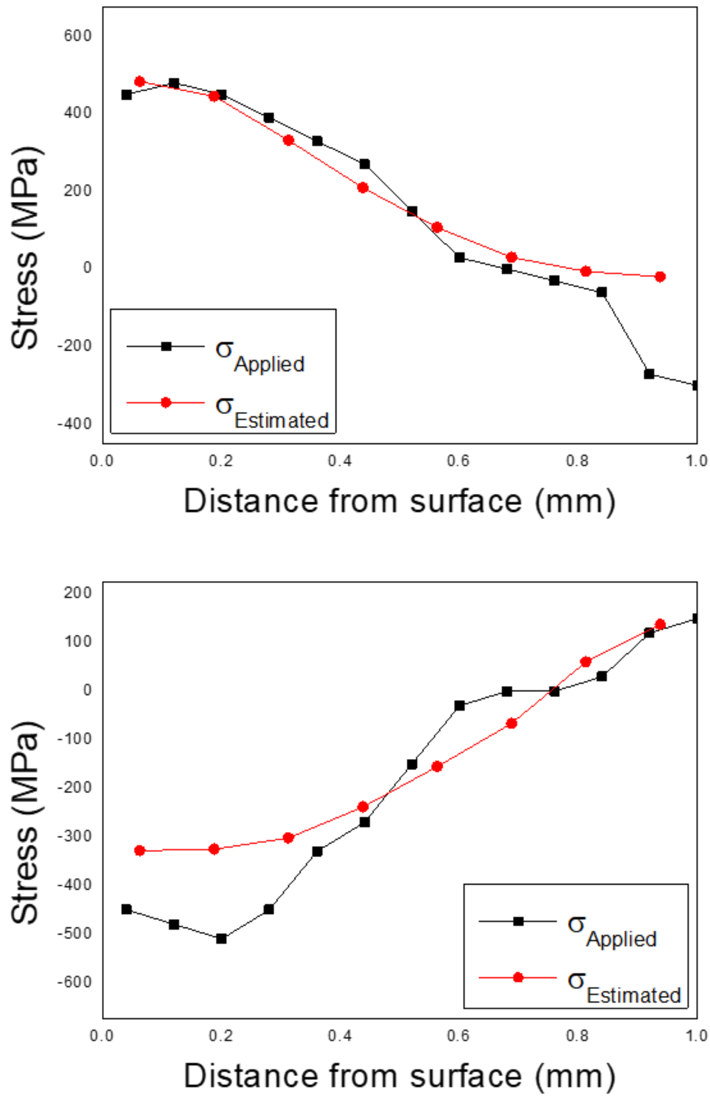

Figure 3.18. Computational verification results of reference material for (a) profile #1, (b) profile #2 (E=200 GPa, $\sigma_Y/E=0.003$, n=0.2, υ=0.3)

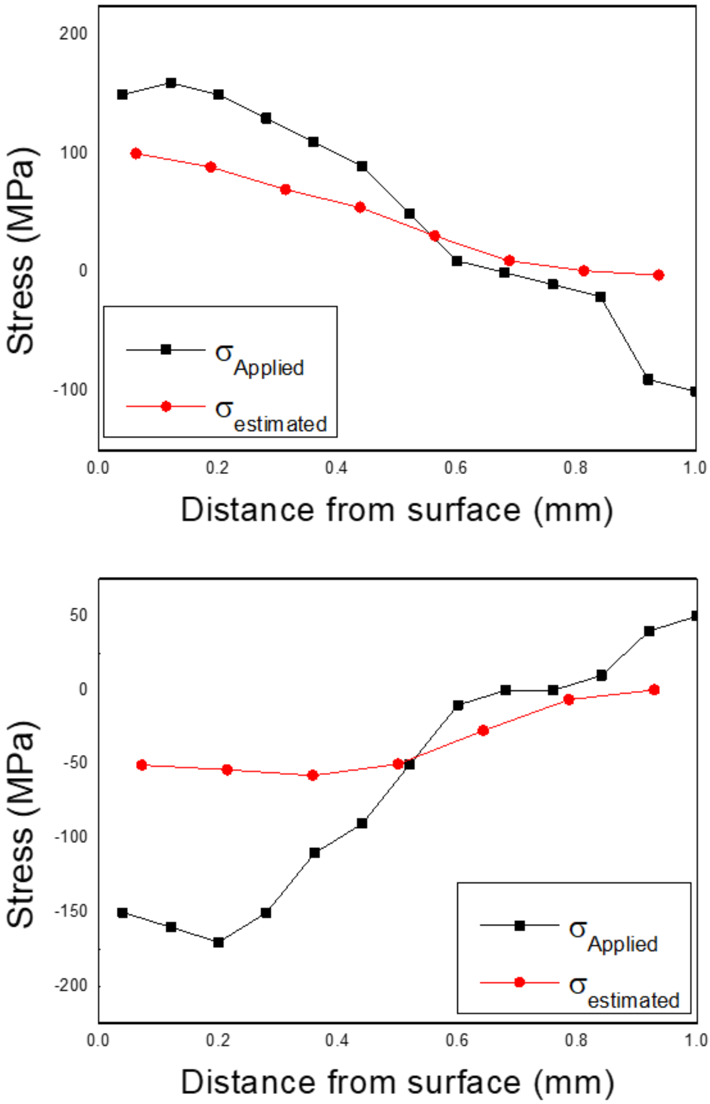

Figure 3.19. Computational verification results of C1220 for

(a) profile #1, (b) profile #2 (E=105 GPa, σ_Y/E=0.002, n=0.06, υ=0.34)

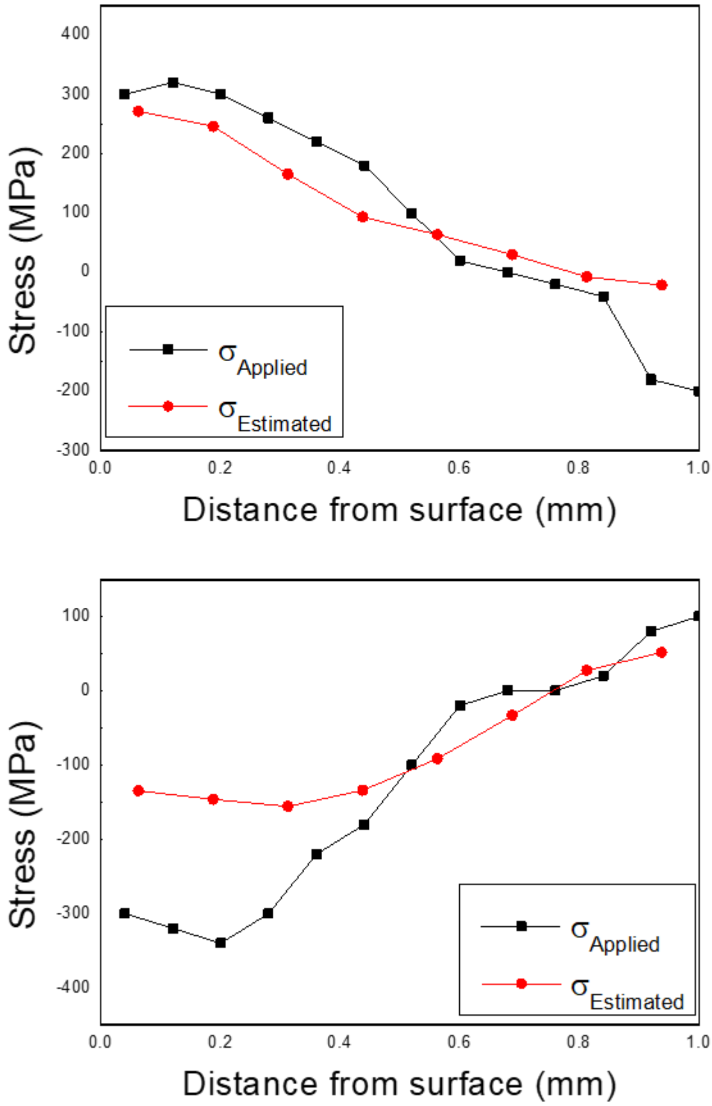

Figure 3.20. Computational verification results of S420J2 for

(a) profile #1, (b) profile #2 (E=209 GPa, σ_Y/E=0.0022, n=0.15, υ=0.275)

References

[1] S. Suresh, A.E. Giannakopoulos, A new method for estimating residual stresses by instrumented sharp indentation, Acta Materialia 46(16) (1998) 5755-5767.

[2] J.G. Swadener, B. Taljat, G.M. Pharr, Measurement of residual stress by load and depth sensing indentation with spherical indenters, Journal of Materials Research 16(7) (2001) 2091-2102.

[3] Y.-H. Lee, D. Kwon, Residual stresses in DLC/Si and Au/Si systems: Application of a stress-relaxation model to the nanoindentation technique, J. Mater. Res. 17(4) (2002) 901-906.

[4] Y.-H. Lee, D. Kwon, Measurement of residual-stress effect by nanoindentation on elastically strained (100) W, Scripta Materialia 49(5) (2003) 459-465.

[5] Y.H. Lee, W.j. Ji, D. Kwon, Stress measurement of SS400 steel beam using the continuous indentation technique, Experimental Mechanics 44(1) (2004) 55-61.

[6] Y.-H. Lee, D. Kwon, Estimation of biaxial surface stress by instrumented indentation with sharp indenters, Acta Materialia 52(6) (2004) 1555-1563.

[7] D. Goudar, D. Smith, Validation of mechanical strain relaxation methods for stress measurement, Experimental Mechanics 53(2) (2013) 267-286.

[8] P. Pagliaro, M. Prime, M. Lovato, B. Zuccarello, Known Residual Stress Specimens Using Opposed Indentation, Journal of Engineering Materials and Technology 131 (2009) 031002.

[9] M. Zhao, X. Xu, S. Liang, J. Zhang, Characterization method of the layer thickness of surface residual stress based on instrumented indentation testing, AIP Advances 9(9) (2019) 095024.

[10] A. Iost, R. Bigot, Indentation size effect: reality or artefact?, Journal of Materials Science 31(13) (1996) 3573-3577.

[11] T.Y. Tsui, W.C. Oliver, G.M. Pharr, Influences of stress on the measurement

of mechanical properties using nanoindentation: Part I. Experimental studies in an aluminum alloy, Journal of Materials Research 11(3) (1996) 752-759.
[12] R. Moharrami, M. Sanayei, Improvement of indentation technique for measuring general biaxial residual stresses in austenitic steels, Precision Engineering 64 (2020) 220-227.
[13] M.K. Khan, M.E. Fitzpatrick, S.V. Hainsworth, L. Edwards, Effect of residual stress on the nanoindentation response of aerospace aluminium alloys, Computational Materials Science 50(10) (2011) 2967-2976.

Chapter 4

IMPROVEMENT OF THEORETICAL MODEL

Contents

4.1. Introduction ········· 104

4.2. Modification of IIT stress evaluation model ········· 108

4.1.1 Stress sensitivity of indentation curve ········· 108

4.1.2 Dimensional analysis ········· 110

4.3. Optimization of calibration coefficient ········· 113

4.3.1. Stress sensing depth ········· 113

4.3.2 Dimensional analysis ········· 112

4.4 Computational verification ········· 117

References ········· 144

4.1. Introduction

Residual stress within materials varies the indentation force-displacement curve depending on the magnitude and sign of the stress state [1, 2]. Various residual stress evaluation models based on indentation testing were proposed by many researchers with different parameters obtained from indentation curve. Contact area, work of indentation and force difference, which are varied by the residual stress, were used to quantify the residual stress [3-9]. The accuracy of representative models was compared by using the finite element analysis for various mechanical properties [10-12]. Every stress evaluation models based on indentation technique showed dependency on mechanical properties with strain hardening exponent (n) and yield strain (ε_y). Lee and Kwon's model generally showed good correlation for the materials with low or medium strain hardening exponent and yield strain ranges.

The estimated stress from the indentation models shows changing transitional trend with applied stress, especially, at around the zero-stress state. Tsui et al. verified the transition in trend of hardness by indentation testing at fixed load condition on the aluminum alloy as shown in Figure 4.1 [1]. The change in hardness results from the miscalculation of contact area using the formula proposed by Oliver-Pharr[13]. The slope of hardness variation with applied stress is differed with the sign of stress state. The different slopes are resulted from the different stress sensitivity in the indentation displacement depending on the sign of stress when the maximum load is fixed. Peak load of indentation, the maximum force, also shows different stress sensitivity on compressive stress and tensile stress as in Figure 4.2 [14]. The different stress sensitivity of indentation parameters is reflected to the stress values estimated through various indentation stress evaluation models. Figure 4.3 shows the comparison of estimated stress and applied stress for five materials with different strain hardening exponents and yield strains [11]. The sensitivity of evaluated stress for the compressive stress state is smaller than that for the tensile stress state in all materials. Stress sensitivity differences with sign of stress are significantly different depending on mechanical properties of materials.

Model proposed by Suresh et al. involves the mechanical properties of material including the elastic modulus, yield strength and ultimate strength [3]. Other models by Wang et al. [4] and Lee and Kwon [5] involve indentation parameters and contact area. All three representative models are showing the different stress sensitivity by the sign of stress and mechanical properties [10-12]. Xu et al. optimized elastic recovery displacement based model by reflecting mechanical property dependency using finite element analysis [15]. Similarly, Lu et al. performed a dimensional analysis to correct the stress sensitivity by the mechanical properties for the loading curve based model [16]. However, the model is based on the assumption of uniform-stress through the depth of material. Therefore, the model for profiling through-thickness residual stress considering the effect of mechanical properties on stress sensitivity is highly required.

Hole-drilling residual stress evaluation methods is based on the assumption that the stress relaxed down to the hole depth by the drilled hole. The stress distributing beneath the hole depth rarely influences the surface strain due to the continuity of material is maintained. In other words, the depth of stress measured by the hole drilling is determined by test conditions with the size of strain gauge and maximum hole depth. On the other hands, stress sensing depth of indentation has correlation depending on mechanical properties, like the stress sensitivity. The depth influencing the indentation curve with the presence of stress is, consequently, related with the plastic zone size developed by indentation. The stress and strain field developed by indentation was analyzed with the concept of expanding cavity assuming that the displaced volume of material with increasing indentation displacement related with the radial expansion of cavity [17, 18]. The plastic zone size determined by the various models relies on the elastoplastic mechanical properties such as elastic modulus, yield strength and hardness as well as geometrical shape of indenter [19-21]. Therefore, the stress sensing depth, related with plastic zone size, varies with the mechanical properties of materials, which means the correction of calibration coefficient in consideration of material properties is required.

4.2. Modification of IIT stress evaluation model

4.2.1. Modification of IIT stress evaluation model

FEA simulations of indentation were performed to investigate the different stress sensitivity of indentation curve. Figure 4.4 shows the change in indentation loading curve for the material with yield strength of 360 MPa stressed from compressive to tensile by the interval of 50 MPa. The change in maximum force shows different stress sensitivity by the sign of stress as shown in the enlarged graph. The estimated stress by Lee and Kwon's model showed transitional trend with applied stress (Figure 4.5), comparable in tensile residual stress state, however, underestimated in compressive stress state.

Indentation using FEA simulations for different material properties were performed to identify the mechanical property dependency of stress sensitivity approximately at uniform stressed state using model explained in 3.1. Elastic modulus was fixed as 200 GPa, and one of yield strain, strain hardening exponent and Poisson's ratio was altered based on the combination of mechanical properties; $\varepsilon_y = 0.0018,\ \ \nu = 0.3, n = 0.05$. Stress evaluated by Lee and Kwon's model showed mechanical property dependency dominantly by the variation of yield strain and strain hardening exponent as in Figures from 4.6 to 4.8. Effect of the change in Poisson's ratio is minimal comparing with the other properties.

Error between the applied stress and evaluated stress can be easily corrected by multiplying the ratio between two stresses to as-evaluated value, if the ratio can be determined by the information of mechanical properties. However, the ratio significantly differs by the sign of stress as well as by mechanical properties as explained in 4.1, therefore, the relation between the residual stress (σ_{RS}) and evaluated stress (σ_{IIT}) is difficult to be simply defined as one value for each material. The stress sensitivity of Lee and Kwon's model in the range of stress with fixed sign (positive or negative) can be assumed as linear relation passing through the origin point. Therefore, the ratio can be defined separately to the tensile and compressive state as represented in Eqs. from (4-1) to (4-2) with an linear assumption for each sign, where the S_T and S_C are the ratio for tensile and compressive stress state.

$$\sigma_{RS} = S_T \cdot \sigma_{IIT} \ \ (\Delta\mathrm{F} > 0) \tag{4-1}$$

$$\sigma_{RS} = S_C \cdot \sigma_{IIT} \ (\Delta\mathrm{F} < 0) \tag{4-2}$$

One of the ratios can be determined by the sign of force difference, which can be obtained by comparing the indentation curves measured from stressed and stress-free state for the case of uniform stress evaluation. The sign of force difference by increment layer stress, $\Delta F_{i,i}$ determines proper correction ratio for each layer stress.

4.2.2. Dimensional analysis

FEA simulations with adjustment of two mechanical properties, the yield strain and strain hardness exponent, were performed for dimensional analysis, ignoring the minimal effect of Poisson's ratio. The indentation simulations for 42 kinds of materials at 27 stress state including stress-free state were performed. Stress intervals were adjusted as 10% within 60% of yield strength and as 5% for the stress magnitude above 60% of yield strength due to the linearity relatively drops as stress magnitude increases. The mechanical properties of materials and stress level applied to FEA simulations are summarized in Table 4-1.

Comparisons of the estimated stress with applied stress normalized by yield strength of the materials are represented in Figure 4.9, showing wide range of variation depending on the mechanical properties. As mentioned, the relation between normalized applied stress and estimated stress is difficult to be assumed to straight line in whole stress level. Estimated stresses for compressive states are smaller than the stresses for tensile states regardless of materials. Therefore, compressive and tensile stress state were separated to obtain the correction slopes (σ_{RS}/σ_{IIT}) with linear assumption as in Figure 4.10.

Dimensional analysis is a technique to correlate the independent and dependent variables by reducing the related variables mathematically [22]. Dimensional analysis for describing the correlation between the correction slope, strain hardening exponent and yield strain were performed for tensile and compressive stress states, respectively. Firstly, the correlation between correction slope and n was formulated as in Eqs. (4-3) and (4-4),

$$S_T = a_T \times {b_T}^n \ (\sigma_{RS} > 0) \tag{4-3}$$

$$S_C = a_C \times {b_C}^n \ (\sigma_{RS} < 0) \tag{4-4}$$

in exponential form based on the form of graph represented Figure 4.11.

Secondly, the correlation of intermediate fitting coefficients (a,b) and ε_y was formulated as in Eqs. (4-5) and (4-6), in power law form based on the shape of graph represented Figure 4.12. The equation reflecting the effect of mechanical property to Lee and Kwon's model is represented as

Eq.(4-7).

$$a = \mathrm{p} \times (\varepsilon_y)^q \tag{4-5}$$

$$b = \mathrm{r} \times (\varepsilon_y)^s \tag{4-6}$$

$$\sigma_{RS} = \sigma_{RS} \cdot (\mathrm{p} \cdot (\varepsilon_y)^q) \cdot ((\mathrm{r} \cdot (\varepsilon_y)^s))^n \tag{4-7}$$

The correction slopes and fitting coefficients with material properties and sign of stress obtained from FEA simulations and the dimensional analysis are summarized in Tables from (4.2) to (4.5). Figure 4.13 shows the corrected results by applying Eq. (4-7) to indentation stress evaluation results. For some materials, the deviation from applied stress is 20% of yield strength depending on the material type when the stress magnitude is increased up to yield strength level. For more accurate estimation, correction optimized to specific mechanical property would be required as Barkhausen method requires the sensitivity of Barkhasen magnetic nose with stress. However, the correction by applying Eq. (4-7) generally reduces the error efficiently with simple formulation.

4.3 Optimization of calibration coefficient

4.3.1 Stress sensing depth

Stress sensing depth of indentation was assumed based on the proportion of force difference generated by the layer stress in depth of ten times of indentation displacement. Layer stress beneath the depth minimally affect the force difference, less than 3 %, therefore, the assumption ignoring the layer stress over the depth is suitable for profiling the stress through the thickness for reference material as shown in Figure 3.17. However, the applying the same calibration coefficient regardless of mechanical property of material may result in the wrong profile, due to the stress sensing depth can be quite different. Therefore, correlation between the maximum stress sensing depth and mechanical properties need to be investigated for the general application for various materials.

FEA simulations with increasing stressed depth by the method introduced in 3.1 were performed by changing mechanical properties as in Table 4.1. The variation of normalized cumulative $\Delta F/\Delta F_{max}$-$h_{stressed}/h_{max}$ curve depending on the change of mechanical properties are showed in Figure 4.14 The maximum sensing depths of each material were determined by central difference normalized by the slope from origin point from the $\Delta F/\Delta F_{max}$-$h_{stressed}/h_{max}$ normalized curve obtained as in 3.2.2, which was used for defining critical depth in previous research [23]. The criterion to determine the maximum sensing depths, saturating points, follows the Eq. (4-8),

$$\left|\frac{\Delta y}{\Delta x}\frac{x}{y}\right| \leq 0.2$$

when x and y indicate $\Delta F/\Delta F_{max}$ and $h_{stressed}/h_{max}$ from the curves (Figure 4.14). The saturating points were compared with the plastic zone depth by measuring the AC yield depth from the surface through FEA simulations as represented in Figure 4.15. The fitting curve, red line in the figure, has slope of 0.97 passing through the origin point, indicating the saturating depth and plastic zone size is almost identical. The stress distributed down to the depth of plastic zone generates most of the indentation force difference, otherwise, the stress below the depth rarely influences the indentation curve.

Normalization of cumulative $\Delta F/\Delta F_{max}$-$h_{stressed}/h_{max}$ by the plastic zone depth overlaps the curves as one curve with and improved level of error as in Figure 4.16. Estimation of plastic zone depth with yield strain and strain hardening exponent shall be preceded to take appropriate calibration coefficient for the accurate evaluation of through thickness residual stress. The average curve of the overlapped $\Delta F/\Delta F_{max}$ - $h_{stressed}/h_{plastic}$ curves can be used for calculating the cumulative coefficient followed by calibration coefficient. The coefficients (Tables 4.9 and 4.10) can be applied for various materials with information of yield strain and hardening exponent, then, the depth of evaluated stress can be accurately optimized by multiplying the ratio of plastic zone depth and indentation displacement.

4.3.2 Dimensional analysis

FEA simulations with adjustment of two mechanical properties, the yield strain and strain hardness exponent, were performed for dimensional analysis. The depth of plastically deformed zone for 42 kinds of materials were measured from the outputs of simulations using AC yield option. The mechanical properties of materials applied to FEA simulations are summarized in Table 4.1. Dimensional analysis to describe the correlation between the plastic zone depth, strain hardening exponent and yield strain were performed. Firstly, the correlation between plastic zone and n was formulated as in Eqs. (4-9), in linear form based on represented graph in Figure 4.17. Secondly, the correlation of intermediate fitting coefficients (a, b) and yield strain was formulated as in Eqs. (4-10) and (4-11),

$$h_{plastic} = a - b \cdot \mathrm{n} \tag{4-9}$$

$$a = p - q \cdot \varepsilon_y \tag{4-10}$$

$$b = r \cdot (\varepsilon_y)^s \tag{4-11}$$

in linear and power law forms based on represented the form of graph shown in Figure 4.18. The depth of plastic zone with yield strain and strain hardening exponent can be expressed as Eq. (4-7).

$$h_{plastic} = p - q \cdot \varepsilon_y + \left(r \cdot {\varepsilon_y}^s\right) \cdot \mathrm{n} \tag{4-12}$$

The plastic depth and fitting coefficients with material properties obtained from FEA simulations and the dimensional analysis are summarized in Tables from (4.6) to (4.8). The maximum difference between the measured plastic depth from FEA results and estimated depth was less than 2.9% and the mean absolute error was about 1.2 %.

4.4 Computational verification

FEA simulations of C1220 and S420J2 used for computation verification in 3.3.2 were reanalyzed by applying correction methods proposed in 4.2 and 4.3. Red lines drawn in Figures 4.19 and 4.20, corrected results by 4.2, show that the magnitude of stress around initial depths are matched better than as-estimated results. However, the transition trends in stress distribution are not estimated well just by the magnitude correction due to the stress sensing depths of C1220 and S420J2 are far lower than ten times of indentation displacement, 0.70 and 0.81, respectively. The second correction in consideration of stress sensing depth were applied for evaluation results shown as blue lines in Figures 4.19 and 4.20, recalculating the depth of evaluated stress by the ratio of plastic zone depth and indentation displacement. Overall trends and magnitude of stress distribution are matched well.

Table 4.1. Mechanical properties of materials and stress level applied to FEA simulations

Elastic modulus E (GPa)	Poisson's ratio ν	Yield strain $\varepsilon_y=\sigma_y/E$	Strain hardening exponent n	Stress level σ_{RS}/σ_y
200	0.3	0.001	0.0	0
		0.002	0.1	$\pm$0.1
		0.003	0.2	$\pm$0.2
		0.004	0.3	$\pm$0.3
		0.005	0.4	$\pm$0.4
		0.006	0.5	$\pm$0.5
			0.6	$\pm$0.6
				$\pm$0.65
				$\pm$0.7
				$\pm$0.75
				$\pm$0.8
				$\pm$0.85
				$\pm$0.9
				$\pm$0.95

Table 4.2. Correction slopes (S_T) by mechanical properties

n \ ε_y	0.001	0.002	0.003	0.004	0.005	0.006
0.0	2.09155	1.20557	0.93644	0.8175	0.75519	0.71813
0.1	1.28836	0.89263	0.76447	0.70407	0.67196	0.6536
0.2	0.86093	0.68994	0.63163	0.6056	0.59359	0.58861
0.3	0.59653	0.53825	0.52352	0.52162	0.52442	0.52971
0.4	0.42707	0.42972	0.44175	0.45483	0.46814	0.48184
0.5	0.32073	0.35419	0.3808	0.40416	0.42584	0.44663
0.6	0.25309	0.30121	0.33866	0.37181	0.40233	0.43101

Table 4.3. Correction slopes (S_C) by mechanical properties

n \ ε_y	0.001	0.002	0.003	0.004	0.005	0.006
0.0	4.42742	2.35016	1.66095	1.32548	1.12922	1.00941
0.1	2.30074	1.47251	1.16286	1.00954	0.91902	0.86373
0.2	1.35844	1.00842	0.87583	0.80996	0.77386	0.75481
0.3	0.84607	0.7206	0.67723	0.6607	0.65563	0.65718
0.4	0.55263	0.53385	0.53811	0.54882	0.56224	0.57732
0.5	0.38406	0.41358	0.44084	0.46726	0.49314	0.51869
0.6	0.28262	0.33418	0.37677	0.41763	0.45537	0.49155

Table 4.4. Fitting coefficients for considering mechanical property effect

ε_y	a_T	b_T	a_C	b_C
0.001	2.04051	0.01724	4.34386	0.00357
0.002	1.17686	0.0820	2.2794	0.02307
0.003	0.92178	0.16597	1.60382	0.06376
0.004	0.80868	0.24934	1.28318	0.12314
0.005	0.74842	0.32684	1.10021	0.19654
0.006	0.71187	0.39973	0.99030	0.27610

Table 4.5. Fitting coefficients for considering mechanical property effect

Stress state	p	q	r	s
$\sigma_{RS} > 0$	0.02271	-0.64778	428.0341	1.35843
$\sigma_{RS} < 0$	0.01036	-0.87315	11678.65	2.07971

Table 4.6. Plastic zone depth ($h_{plastic}$) by mechanical properties

n \ ε_y	0.001	0.002	0.003	0.004	0.005	0.006
0.0	0.66034	0.64469	0.62903	0.61338	0.59772	0.58205
0.1	0.83636	0.77273	0.72511	0.69347	0.66183	0.64614
0.2	0.99642	0.88483	0.82122	0.76370	0.72601	0.69437
0.3	1.17249	0.99696	0.90140	0.82187	0.77427	0.72671
0.4	1.33260	1.09314	0.98160	0.88611	0.82257	0.77500
0.5	1.54068	1.20532	1.04589	0.96496	0.88685	0.82336
0.6	1.70586	1.31755	1.16041	1.03070	0.93528	0.87178

Table 4.7. Fitting coefficients for considering mechanical property effect

ε_y	a	b
0.001	0.66034	1.7306
0.002	0.64469	1.13179
0.003	0.62904	0.87696
0.004	0.61338	0.69878
0.005	0.59772	0.57371
0.006	0.58205	0.48785

Table 4.8. Fitting coefficients for considering mechanical property effect

p	q	r	s
0.67601	-15.65771	0.01743	-0.66717

Table 4.9. Generalized cumulative coefficient

n \ i	1st	2nd	3rd	4th	5th	6th	7th	8th	9th	10th
1	1									
2	0.684	1								
3	0.498	0.830	1							
4	0.385	0.684	0.889	1						
5	0.310	0.578	0.776	0.9195	1					
6	0.258	0.498	0.684	0.830	0.937	1				
7	0.220	0.435	0.609	0.751	0.865	0.949	1			
8	0.192	0.385	0.549	0.684	0.797	0.889	0.957	1		
9	0.170	0.344	0.498	0.627	0.737	0.830	0.906	0.963	1	
10	0.152	0.310	0.455	0.578	0.684	0.776	0.855	0.919	0.968	1

Table 4.10. Generalized calibration coefficient

n \ i	1st	2nd	3rd	4th	5th	6th	7th	8th	9th	10th
1	1									
2	0.684	0.315								
3	0.498	0.332	0.169							
4	0.385	0.298	0.204	0.110						
5	0.310	0.267	0.198	0.142	0.0804					
6	0.258	0.239	0.185	0.146	0.106	0.062				
7	0.220	0.215	0.174	0.141	0.113	0.083	0.051			
8	0.192	0.193	0.163	0.135	0.112	0.091	0.068	0.042		
9	0.170	0.174	0.153	0.128	0.110	0.093	0.075	0.057	0.036	
10	0.152	0.158	0.144	0.122	0.106	0.092	0.078	0.064	0.048	0.031

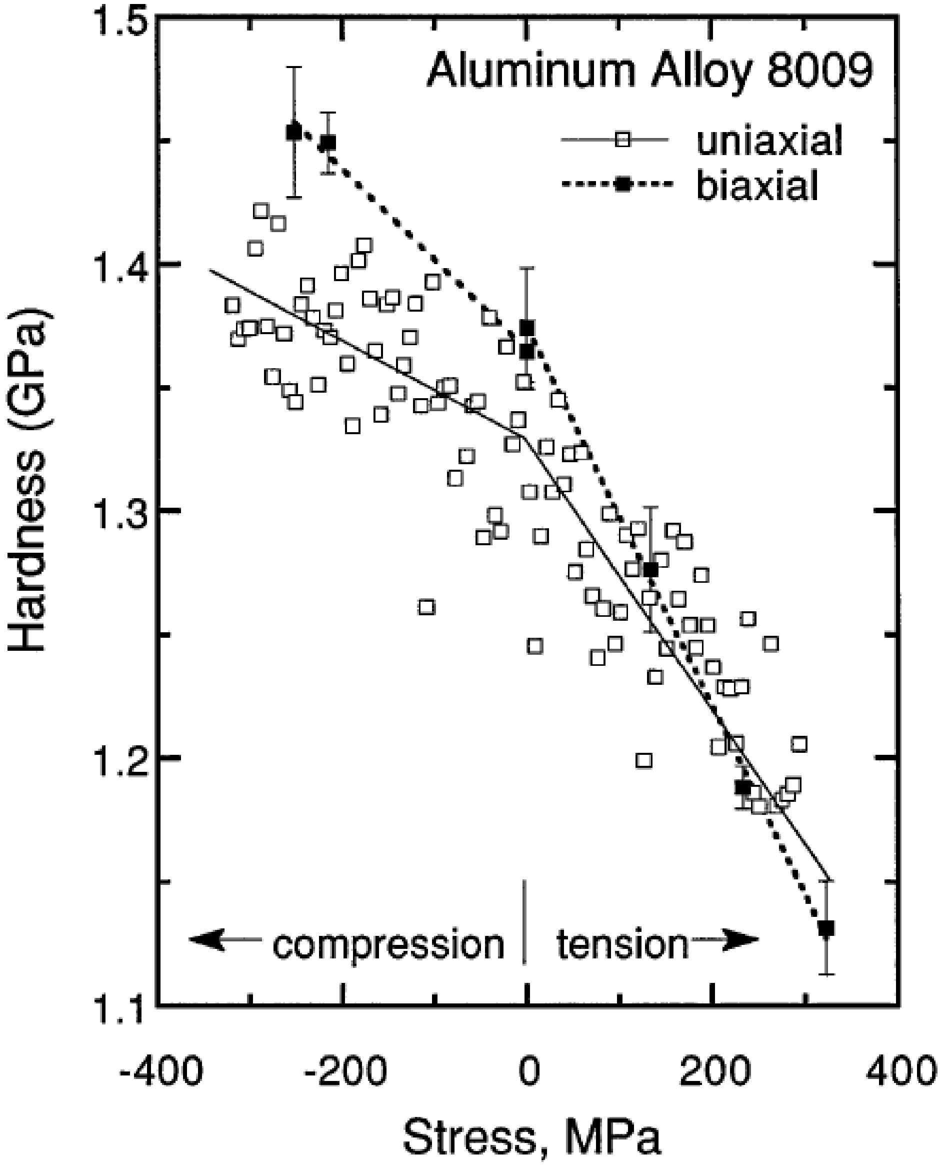

Figure 4.1. Change in hardness depending on the residual stress [1]

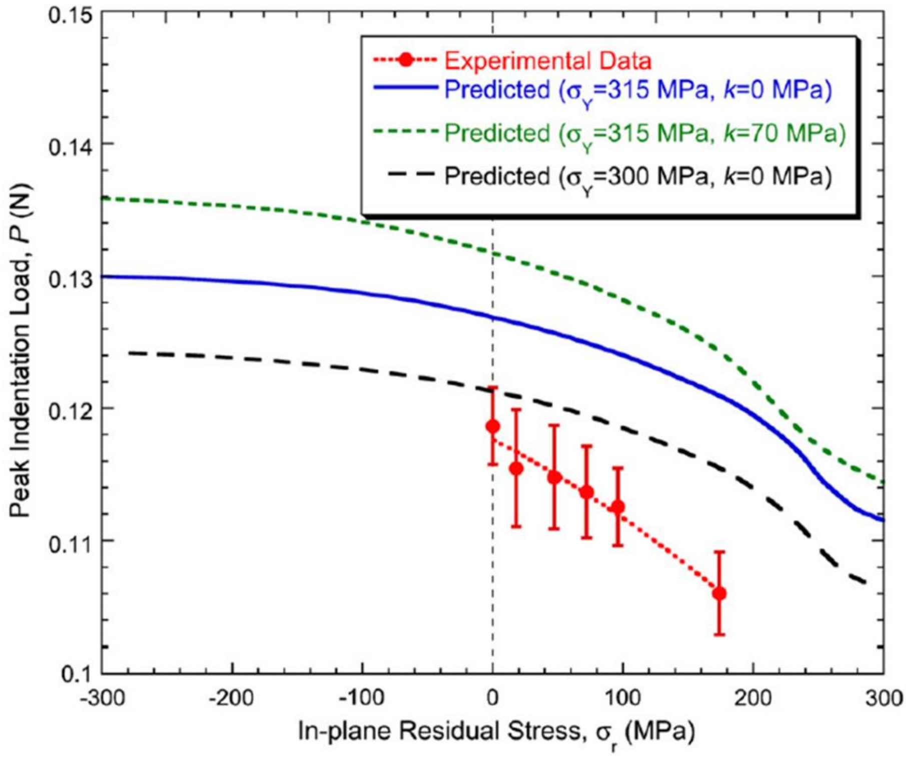

Figure 4.2. Change in peak load of spherical indentation depending on residual stress [14]

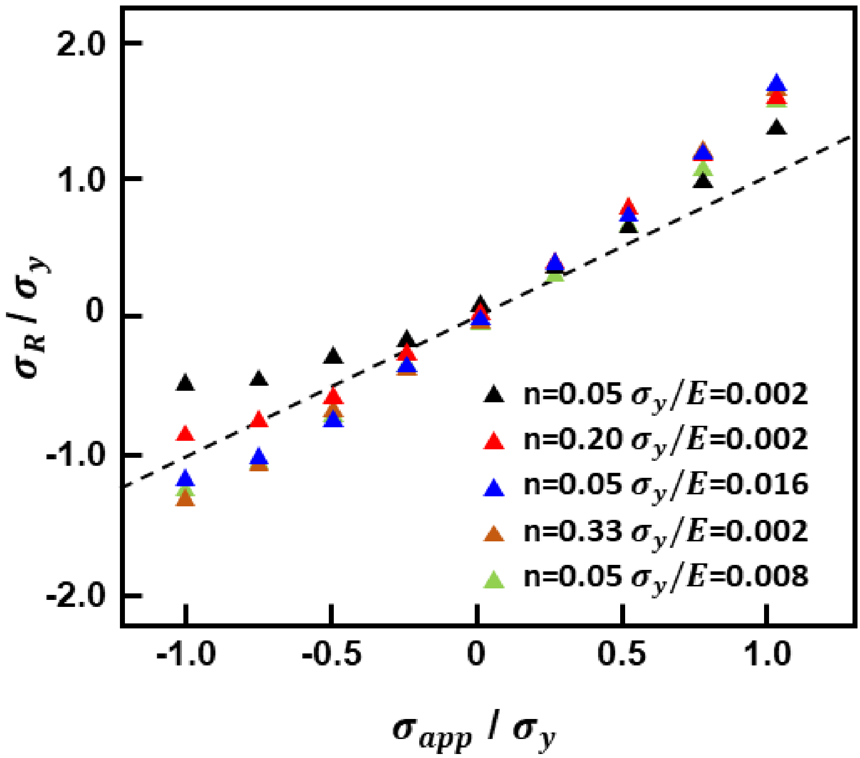

Figure 4.3. Mechanical property dependency of estimated IIT stress using Lee and Kwon's model [11]

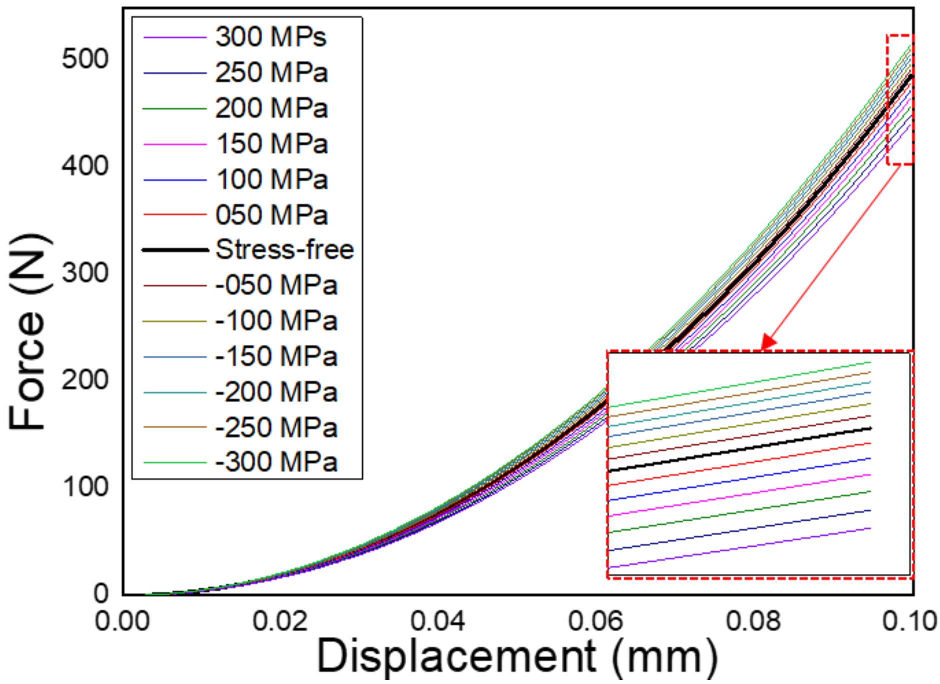

Figure 4.4. Indentation curves from FEA with different stress for the material of E $= 200$ GPa, $\varepsilon_y = 0.0018,\ \nu = 0.3,\ n = 0.05$, inset is enlarged figure around the maximum indentation displacement

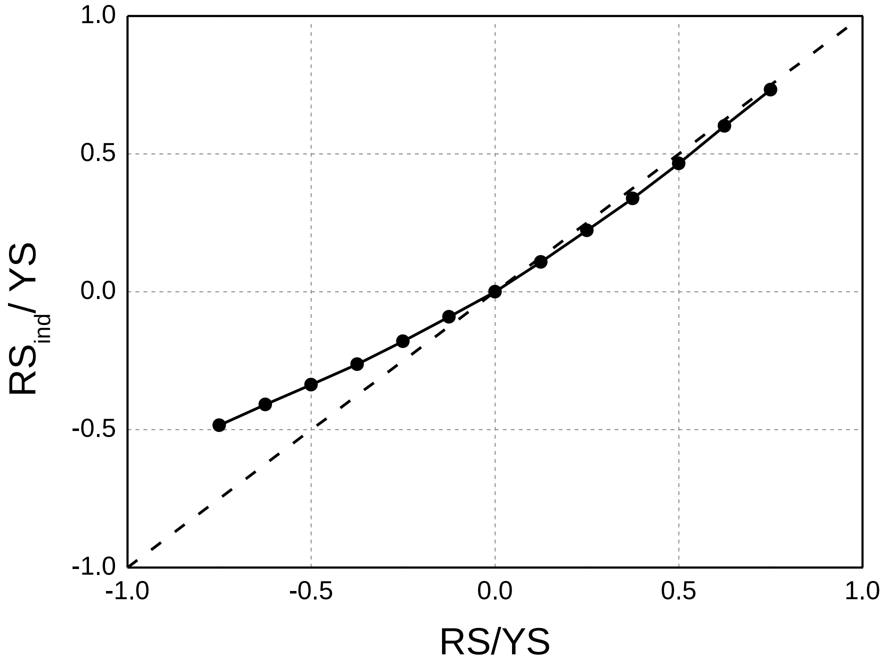

Figure 4.5. Transitional trend of estimated stress by Lee and Kwon's model with applied stress depending on the sign of stress

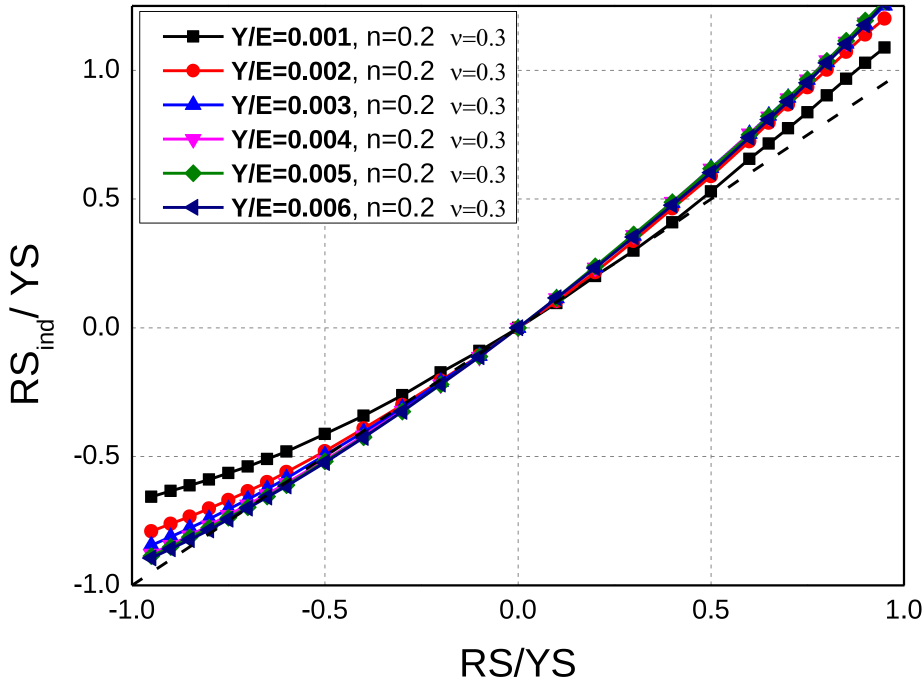

Figure 4.6. Comparison of stress sensitivity on estimated indentation stress with applied stress by change in yield strain

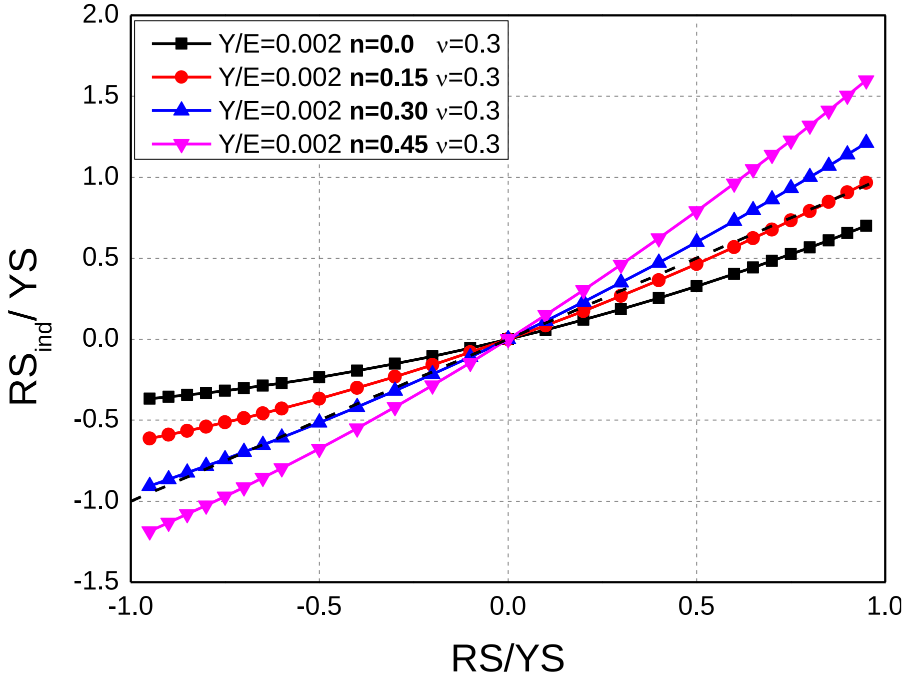

Figure 4.7. Comparison of stress sensitivity on estimated indentation stress with applied stress by change in strain hardening exponent

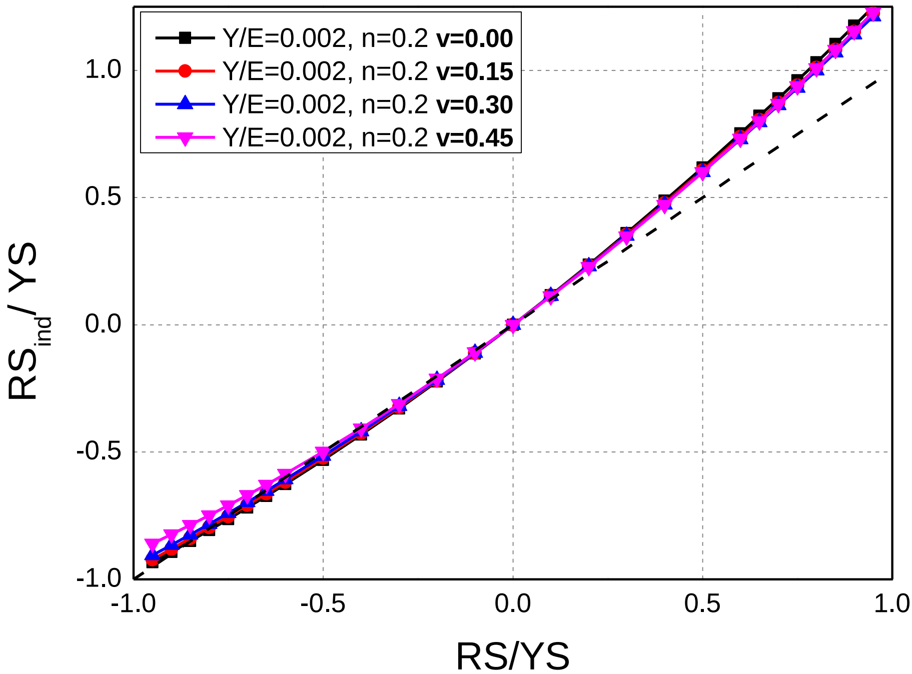

Figure 4.8. Comparison of stress sensitivity on estimated indentation stress with applied stress by change in Poisson's ratio

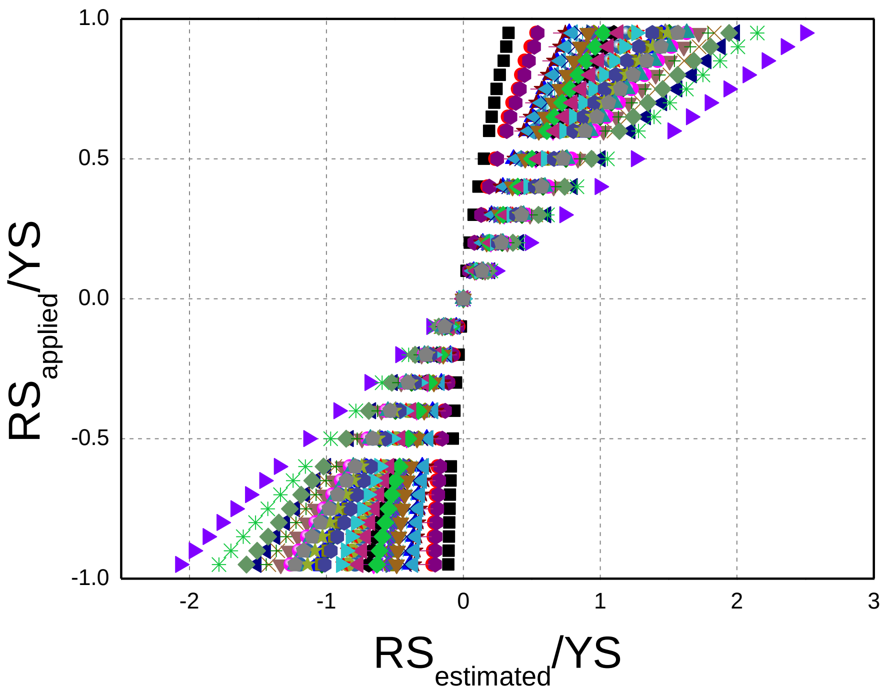

Figure 4.9. Comparison of estimated indentation stress normalized by yield strength with applied stress for the materials in Table 4.1

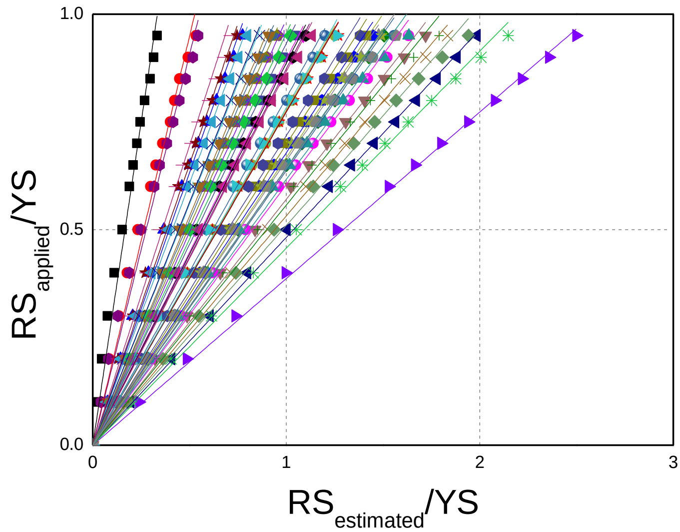

(a) tensile residual stress state

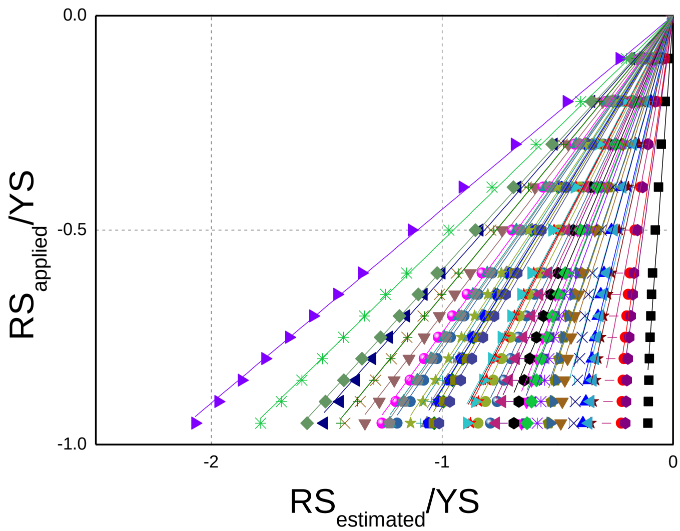

(b) compressive residual stress state

Figure 4.10. Linear relation between estimated indentation stress and applied stress normalized by yield strength

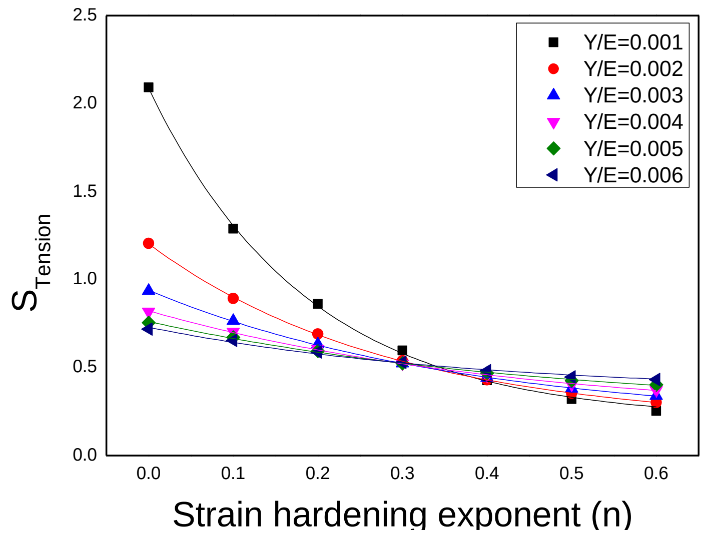

(a) tensile residual stress

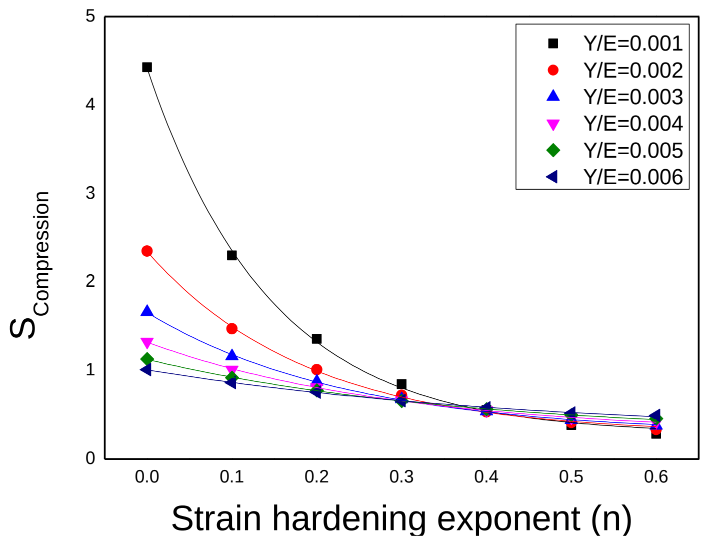

(b) compressive residual stress state

Figure 4.11. Correction slope function of strain hardening exponent

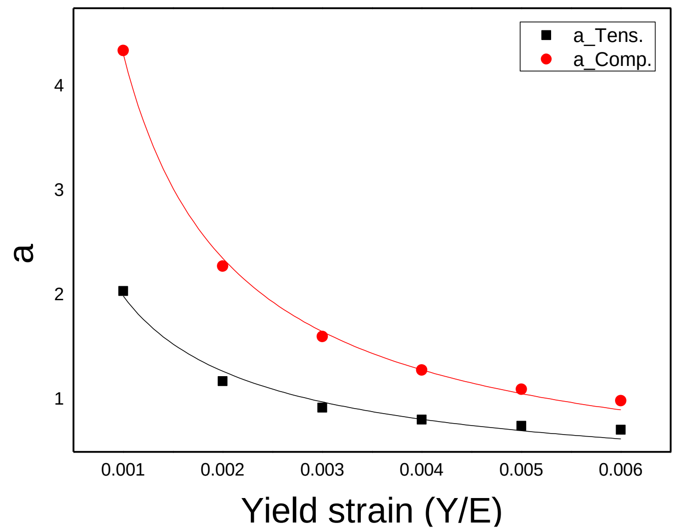

(a) coefficients a

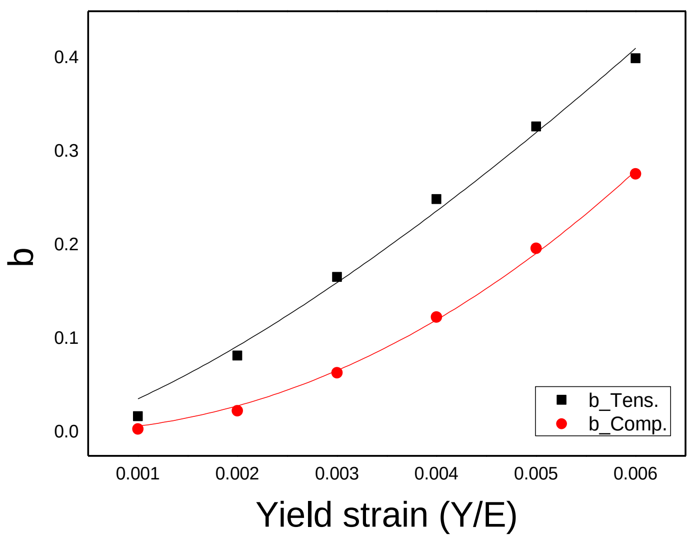

(b) coefficients b

Figure 4.12. Fitting coefficients function of yield strain

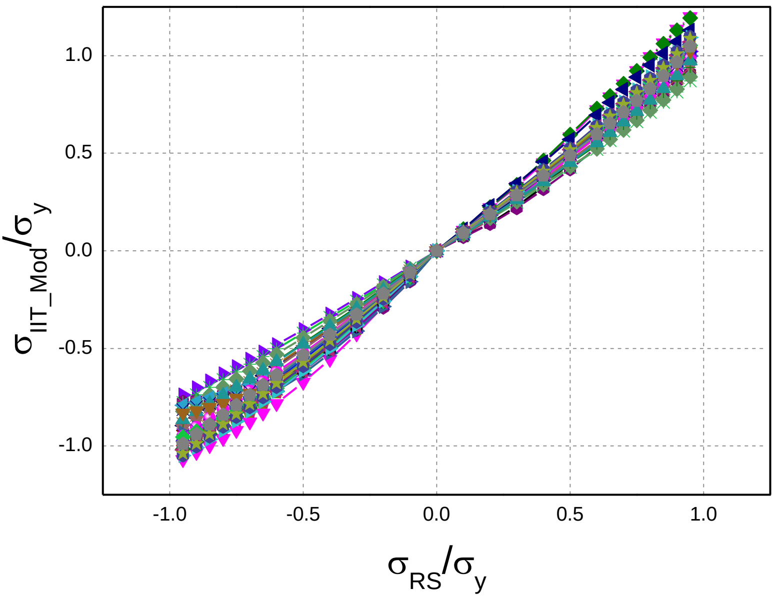

Figure 4.13. Comparison of corrected indentation stress and applied stress normalized by yield strength

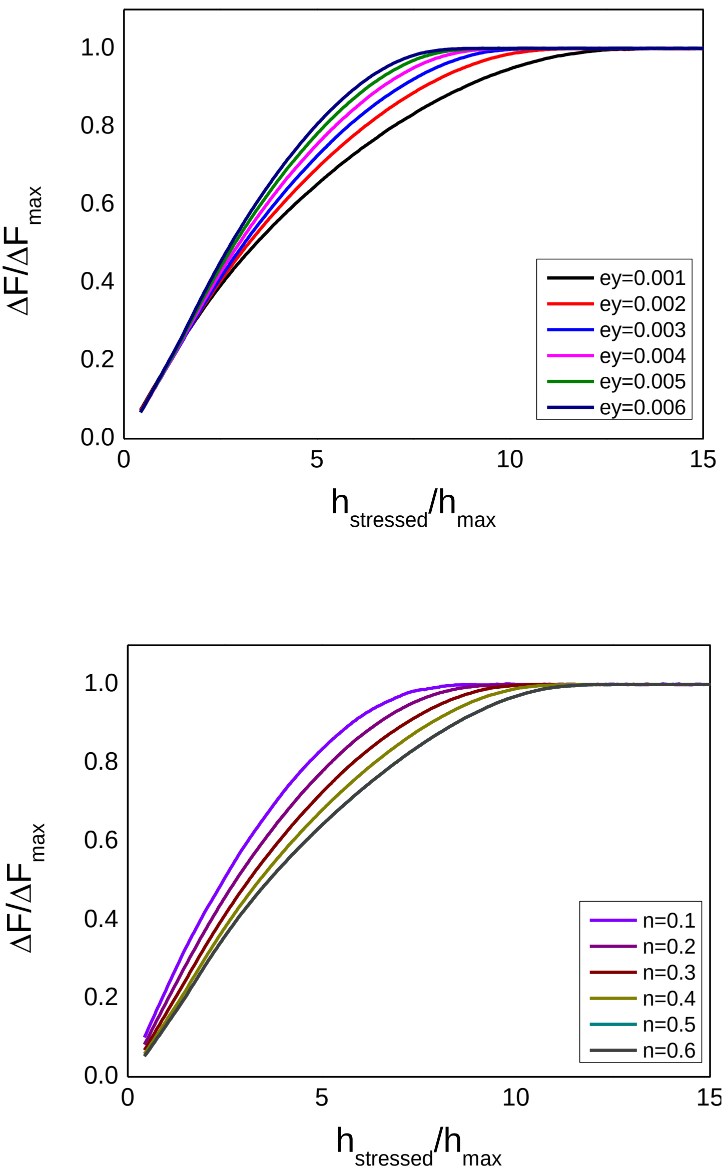

Figure 4.14. Variation of cumulative $\Delta F/\Delta F_{max}$-$h_{stressed}/h_{max}$ curve with (a) yield strain and (b)strain hardening exponent

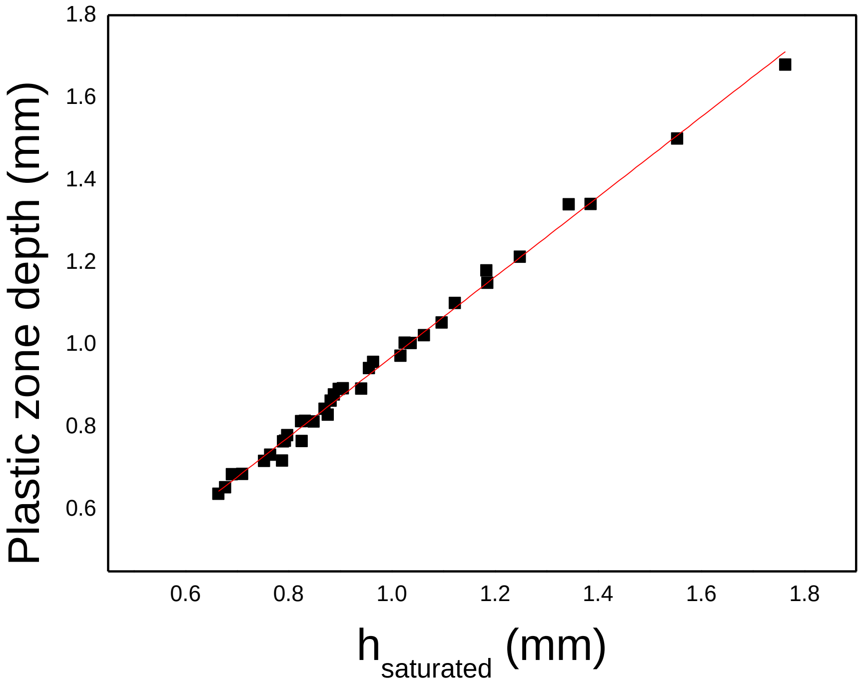

Figure 4.15. Comparison of plastic zone depth and the maximum stress sensing depth when the indentation displacement is 100 μm

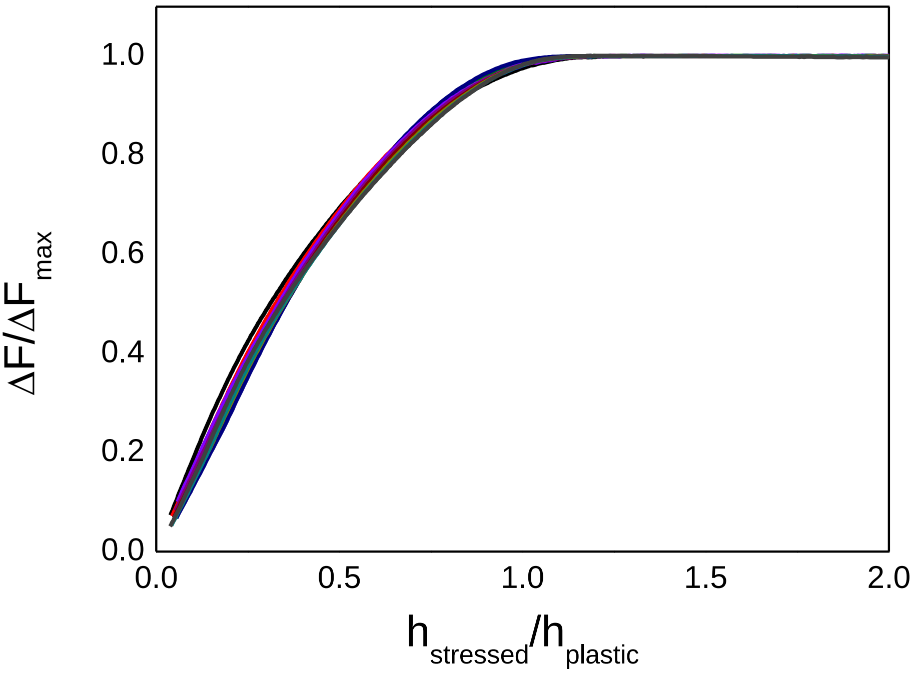

Figure 4.16. $\Delta F/\Delta F_{max}$-$h_{stressed}/h_{max}$ curves of various materials normalized by plastic zone depth

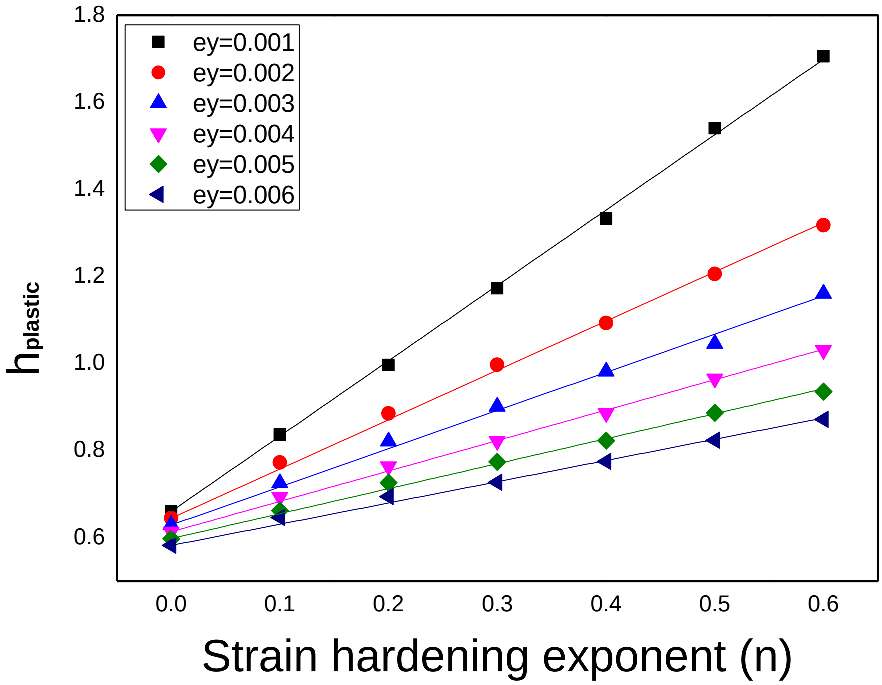

Figure 4.17. Plastic zone depth function of strain hardening exponent

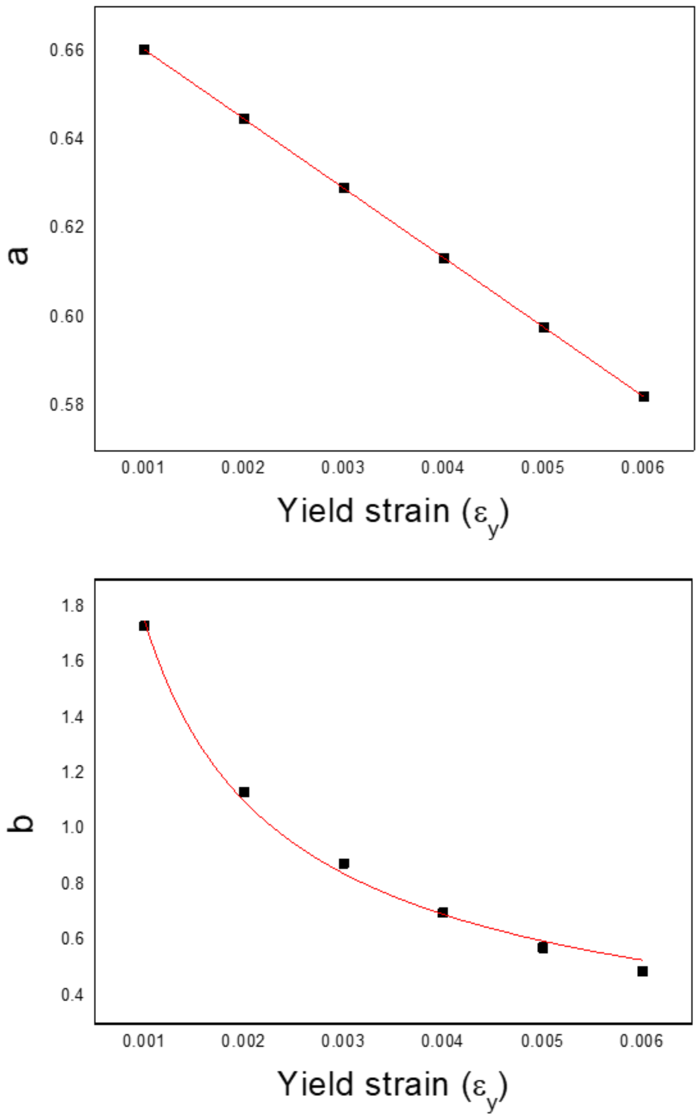

Figure 4.18. Fitting coefficients function of yield strain for (a) a (b) b

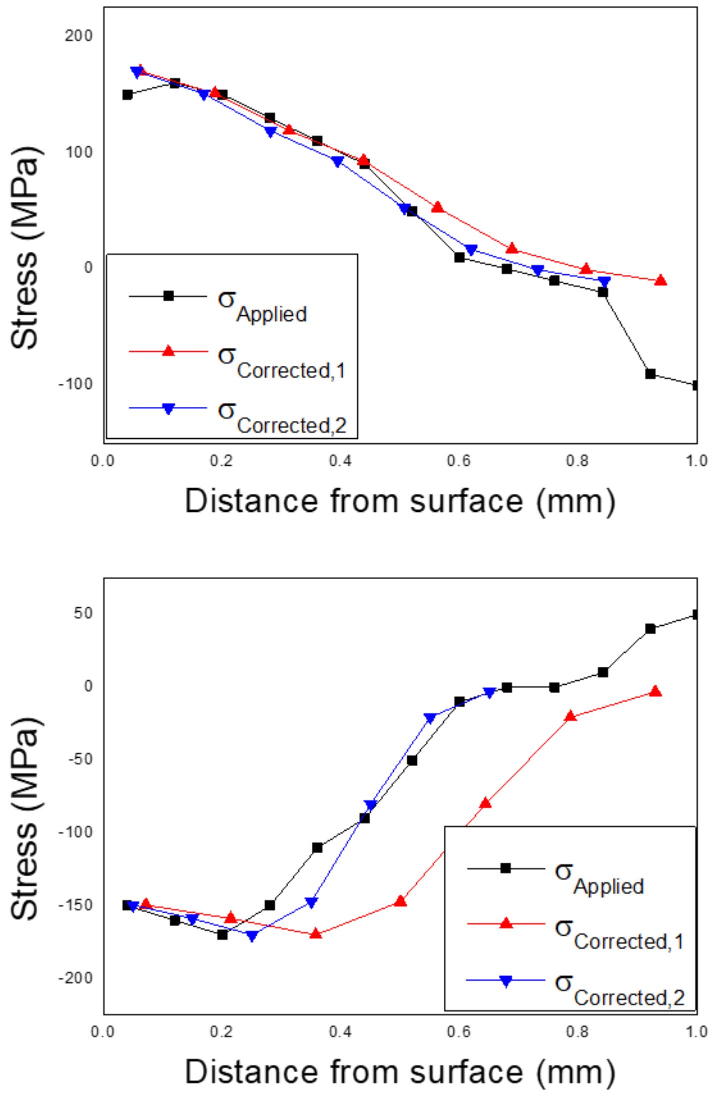

Figure 4.19. Computational verification results of C1220 for

(a) profile #1, (b) profile #2

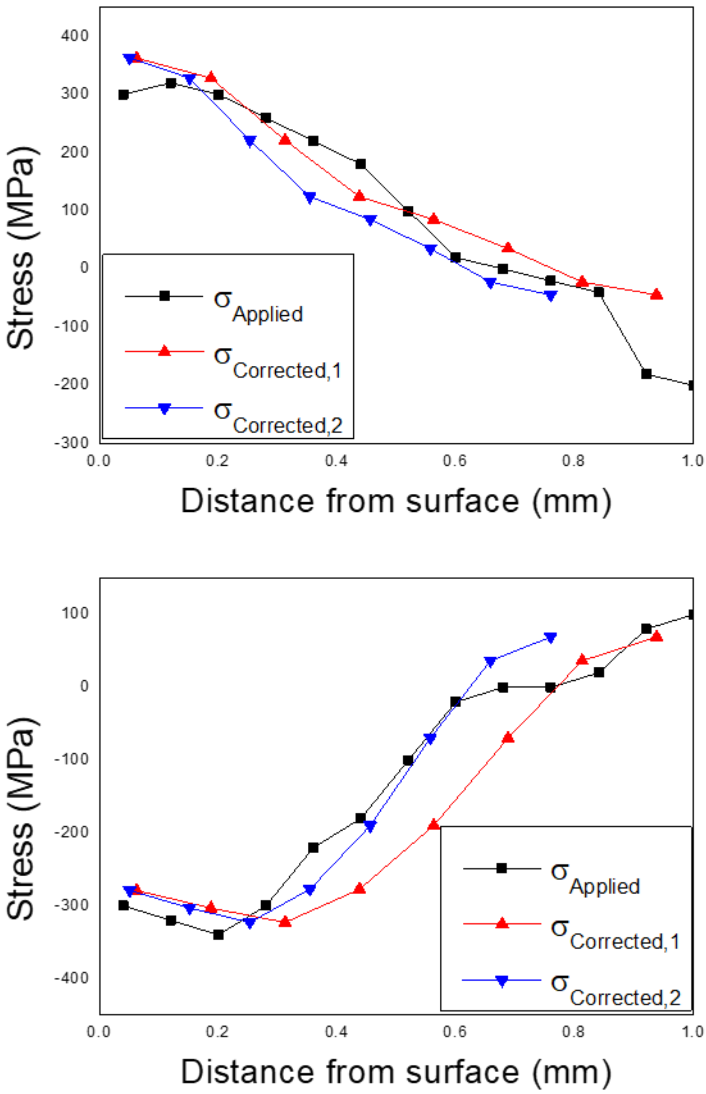

Figure 4.20. Computational verification results of S420J2 for

(a) profile #1, (b) profile #2

References

[1] T.Y. Tsui, W.C. Oliver, G.M. Pharr, Influences of stress on the measurement of mechanical properties using nanoindentation: Part I. Experimental studies in an aluminum alloy, Journal of Materials Research 11(3) (1996) 752-759.

[2] A. Bolshakov, W.C. Oliver, G.M. Pharr, Influences of stress on the measurement of mechanical properties using nanoindentation: Part II. Finite element simulations, Journal of Materials Research 11(3) (1996) 760-768.

[3] S. Suresh, A.E. Giannakopoulos, A new method for estimating residual stresses by instrumented sharp indentation, Acta Materialia 46(16) (1998) 5755-5767.

[4] Q. Wang, K. Ozaki, H. Ishikawa, S. Nakano, H. Ogiso, Indentation method to measure the residual stress induced by ion implantation, Nuclear Instruments and Methods in Physics Research Section B: Beam Interactions with Materials and Atoms 242(1) (2006) 88-92.

[5] Y.-H. Lee, D. Kwon, Estimation of biaxial surface stress by instrumented indentation with sharp indenters, Acta Materialia 52(6) (2004) 1555-1563.

[6] S. Carlsson, P.L. Larsson, On the determination of residual stress and strain fields by sharp indentation testing.: Part I: theoretical and numerical analysis, Acta Materialia 49(12) (2001) 2179-2191.

[7] S. Carlsson, P.L. Larsson, On the determination of residual stress and strain fields by sharp indentation testing.: Part II: experimental investigation, Acta Materialia 49(12) (2001) 2193-2203.

[8] J.I. Jang, Estimation of residual stress by instrumented indentation: A review, Journal of Ceramic Processing Research 10 (2009) 391-400.

[9] H.F. Nadimul, A. Rehan, A Review of Patented Methodologies in Instrumented Indentation Residual Stress Measurements, Recent Patents on Mechanical Engineering 4(2) (2011) 138-152.

[10] R. Moharrami, M. Sanayei, Numerical Study of the Effect of Materials' Plastic Behavior on Equibiaxial Residual Stress Measurement Using Indentation, Iranian Journal of Science and Technology: Transactions of Mechanical Engineering 19 (2018).

[11] L. Xiao, D. Ye, C. Chen, A further study on representative models for calculating the residual stress based on the instrumented indentation technique, Computational Materials Science 82 (2014) 476-482.

[12] C.E.K.M.S.A.R.A.G.G.R.M. Souza, Numerical analysis of different methods to calculate residual stresses in thin films based on instrumented indentation data, (2012).

[13] W.C. Oliver, G.M. Pharr, An improved technique for determining hardness and elastic modulus using load and displacement sensing indentation experiments, Journal of Materials Research 7(6) (1992) 1564-1583.

[14] J. Dean, G. Aldrich-Smith, T.W. Clyne, Use of nanoindentation to measure residual stresses in surface layers, Acta Materialia 59(7) (2011) 2749-2761.

[15] Z.-H. Xu, X. Li, Estimation of residual stresses from elastic recovery of nanoindentation, Philosophical Magazine 86(19) (2006) 2835-2846.

[16] Z. Lu, Y. Feng, G. Peng, R. Yang, Y. Huan, T. Zhang, Estimation of surface equi-biaxial residual stress by using instrumented sharp indentation, Materials Science and Engineering: A 614 (2014) 264-272.
[17] K. Johnson, The correlation of indentation experiments, Journal of the Mechanics and Physics of Solids 18(2) (1970) 115-126.
[18] K. Kug-Hwan, Evaluation of tensile properties of metallic materials using instrumented indentation technique through elastic-plastic stress field analysis, (2011).
[19] M. Mata, O. Casals, J. Alcalá, The plastic zone size in indentation experiments: The analogy with the expansion of a spherical cavity, International Journal of Solids and Structures 43(20) (2006) 5994-6013.
[20] J. Chen, S.J. Bull, On the relationship between plastic zone radius and maximum depth during nanoindentation, Surface and Coatings Technology 201(7) (2006) 4289-4293.
[21] Y. Gao, C.J. Ruestes, D.R. Tramontina, H.M. Urbassek, Comparative simulation study of the structure of the plastic zone produced by nanoindentation, Journal of the Mechanics and Physics of Solids 75 (2015) 58-75.
[22] E. Buckingham, On Physically Similar Systems; Illustrations of the Use of Dimensional Equations, Physical Review 4(4) (1914) 345-376.
[23] M. Zhao, X. Xu, S. Liang, J. Zhang, Characterization method of the layer thickness of surface residual stress based on instrumented indentation testing, AIP Advances 9(9) (2019) 095024.

Chapter 5

EXPERIMENTAL VERIFICATION

Contents

5.1 Materials and methods 147

5.2 Results and discussions 152

5.2.1 Applied stress by four-point bending 152

5.2.2 Peening residual stress 153

5.3 Issues and limitations 154

References 166

5.1 Materials and methods

Stress distributions for the experimental verification test were developed using four-point bending and surface modification by peening process. Applying stress by bending within elastic range develops the through-thickness residual stress distribution without local mechanical property change. The pictures of four-point bending zig used for generating the residual stress distribution are shown in Figure 5.1. Two rods on each side fix the specimen on the top and curved shape block on the bottom is raised by turning the screw.

The specimens of phosphorus deoxidized copper C1220 and martensitic Stainless Steel S420J2 with area of 100*14 were machined by thickness 3 mm and 4 mm followed by heat-treatment for stress relaxation. Plat type uniaxial tensile specimens were fabricated from the same block material for evaluation of tensile properties [1]. Austenitic stainless steels underwent shot peening process were also used for estimation of peening stress distribution. Shot peening process was carried out using 0.7mm cast steel shot with a shot hardness ranged in 55-62 HRC. Tensile properties of the material before peening were used for correction of peening residual stress distribution. Tensile properties of materials obtained from the uniaxial tensile test are summarized as shown in Table 5.1.

Conical indentation tests were performed using AIS3000 instrument (FRONTICS, Republic of Korea) at a maximum indentation displacement of 100 μm within $10 \times 10\ mm^2$ area around the center of the top surface for bending samples. Same instruments and test conditions were applied to the peening samples, and at least 50 indentation tests were performed in consideration of the gradient in local mechanical property. Intervals between the indentations points were 2.5 mm satisfying the requirements proposed in ISO 14577-1 [2]. The projected area was calculated by measuring the diameter of residual indents using optical microscope.

Indentation tests for the stress-free state were carried out before applying stress for the bending samples. For the case of peening samples, samples were cut by electrical discharge machining at a speed of 10 mm/hour with a wire thickness of 100 μm for minimizing the local changes in mechanical properties and microstructures, which affect indentation curve in addition to the relaxation of residual stress. Then, the indentation tests for stress-free state curves were performed near the edge of cut surface, where the stress were confirmed to be relaxed enough by

X-ray diffraction method. Projected area of residual indents was obtained in the same way applied to stressed states.

The stress distribution applied by bending is generally linear through the thickness of material, and comparable level of opposite signed stress is applied on the bottom surface of specimen. The magnitude of the strain applied to the upper surface of bending specimen, area where the tensile stress is applied, was controlled to not exceed the 80% of yield strain by using strain gauges. Three-dimensional FEA simulations were performed for profiling the stress distributions of bending samples as shown in Figure 5.2. The boundary condition of bottom block, moving upward to bend material, was adjusted to match the strain on the upper surface with the strain measured experimentally. The evaluated stress distribution of bending specimens from indentation test were compared with stress distributions measured from FEA simulations of each specimen as shown in Figure 5.3.

The evaluated stress profile of peening specimen using indentation test was compared with hole-drilling method and X-ray diffraction method. Hole drilling was carried out using Micro-measurements RS-200 (Vishay Precision Group, USA) with strain gauge rosettes with 2 mm hole diameter. Depth of 1 mm hole was drilled with 50 μm depth increments. X-ray diffraction methods were applied using μ-X360s (Pulstec Industrial Co., Ltd, Japan) with 50 μm depth increments down to 0.5 mm depth by layer removing.

The flow of the analysis of through-thickness distributing residual stress is represented in Figure 5.4. Force differences by indentation displacements are measured by two indentation curves from different stress states. The plastic depth and correcting slopes are determined from pre-evaluated tensile properties. The force difference generated by layer stress with the depths can be separated using calibration coefficients corrected by the plastic depth. The stress profile by depth can be calculated by dividing force difference by contact area at displacement and correction slopes depending on the sign of force differences.

The area at specific displacement was calculated from the measured projected area at the maximum indentation displacement with assumption that area is proportional to the square of the indentation displacement. The depth of stress can be determined by multiplying the ratio of plastic depth and indentation displacement to the indentation displacements where the force differences were measured. Indentation curves from each specimen were sorted out by hardness value to eliminate the effect of change in local mechanical property on the evaluation results.

Therefore, the data points within 2 % of hardness change were used for the through-thickness residual stress evaluation. Data smoothing, a mathematical procedure to reduce the noise sensitivity, was carried out to improve the data reliability based on the smoothing procedure applied for the other stress relaxation methods [3-5].

5.2 Verification results

5.2.1 Applied stress by four-point bending

Evaluation results of through-thickness bending stress using indentation were matched well with the stress distribution obtained from FEA simulations as represented in Figures 5.5 and 5.6 for C1220 and S420J2, respectively. The stress at the first depth tended to be overestimated, when the area estimated from the maximum projected area is used for stress evaluation under assumption that the areas at each displacement are simply calculated under assumption that hardness is invariant through the thickness. Tip bluntness of the conical indenter used for this verification test was observed as 8.6 μm as in Figure 5.7, which yields the area at the early stage to be underestimated than the real contact area. Therefore, the projected areas at early stage were recalculated in consideration of the bluntness of indenter tip for accurate evaluation of through-thickness stress shown in Figure 5.5 and 5.6.

The stress distribution using indentation for two materials showed more steep decreasing trends compared to the distribution obtained from

FEA. The origin of the difference is inferred to come from the bending compliance of specimens due to the space between the specimens and bottom block as bending is applied. The strain measured during indentation test was decreased to about 97% of initial strain and recovered to initial value after unloading. Therefore, the applied stress through whole depth could be considered to be lowered as indentation is proceeded, however, the stresses evaluated at early depth were assumed to be maintained when calculating the contribution of the stresses on force difference regardless of indentation displacement.

5.2.2 Peening residual stress

Through-thickness stress distribution for peening specimen was evaluated as Figure 5.8. The trend of indentation stress distribution showed comparable to the other methods, however, the magnitudes of stress by depth show some difference. Indentation results are more matched with X-ray diffraction method, rather than hole-drilling method.

5.3 Issues and limitations

All residual stress evaluation methods have clear limitations. Hole-drilling method is known to be a quantitative and capable of stress depth-profiling method, however, it has limitation of measuring the near-surface residual stress. Additionally, the plasticity effect restricts the accuracy of hole-drilling method to be assured, when the stress level is lower than the 60% yield strength [6]. The generation of localized plastic deformation by the drilling distorts the stress estimation, if the stress around hole is high. The overestimated stress from hole-drilling at early depth for peening specimen is considered to be results from plasticity effect.

There are potential origins of error for through-thickness residual stress evaluation using indentation, even setting aside the problems such as spatial resolution and technical issues that arise from the differences between measurement methods. As mentioned in 5.2 the bluntness indenter shall be carefully considered for accurate estimation of contact area at early stage. It is recommended to use indenter with minimal bluntness compared to the unit depth to evaluate near-surface residual stress accurately, or correction shall be followed as performed in this study. Additionally, the calibration coefficients show some amount of variation depending on the magnitude of residual stress depending on the mechanical properties, especially, for high level of tensile residual stress states. Error resulted from stress dependency of calibration coefficients is considered to be corrected by dimensional analysis as done for correcting slope followed by iteration process for determining correct sets of the layer stress appropriately.

Indentation method requires the force difference only by the variation of residual stress, not including the difference by the variation of mechanical properties for accurate stress evaluation. Small changes or differences of local mechanical property could yield the distortion of evaluated results. Careful electrical discharge machining, which is known to be the best way for stress relaxation, need to be used for manufacturing the stress-free specimen. However, indentation test needs to be keep the distance from free-edge to obtain a correct force-displacement curve [2], which means the test shall be proceeded at the location where the stress relaxation rate is not high enough. Thus, proper heat treatment for stress relaxation in a range of temperature that does not change the local mechanical properties is required. Even the stress relaxation process succeeded in any methods, enough number of indentation tests shall be proceeded for obtaining the stressed and stress-free state curves to be matched with similar hardness level; within 2% deviation.

Correction for local mechanical property can be performed by identifying the relation between the contact area and plastic deformation level [7]. However, the relating function shall be obtained previously through the experiment or computational analysis. The gradient in mechanical properties through the thickness of material is another key issue need to be considered, which is ignored from this study. Surface modifications and heat treatment process not only generate the non-uniform stress, but also the non-uniform plastic deformation. Therefore, through thickness gradients in mechanical properties shall be measured for correct stress estimation by cross-sectional indentation, or the variation need to be estimated by analyzing indentation curve from surface of specimen without residual stress.

Table. 5.1. Tensile properties of materials for verification test

Material	Elastic modulus E (GPa)	Poisson's ratio ν	Yield strength Y (MPa)	Hardening exponent n
C1220	105	0.34	228	0.060
S420J2	198	0.29	405	0.184
SUS303	200	0.25	277	0.521
SUS316	226	0.27	273	0.411

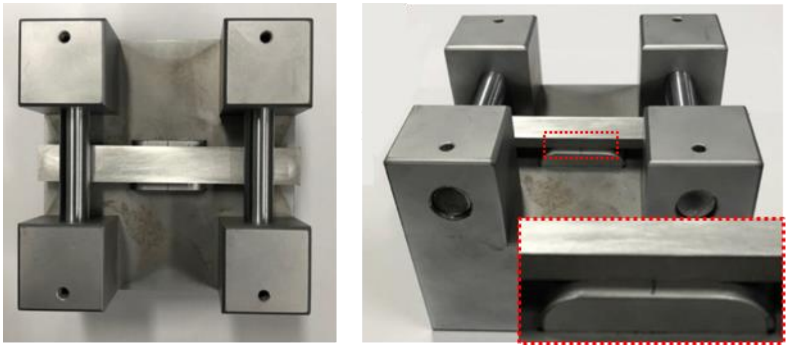

Figure. 5.1. Picture of four-point bending jig for generating through-thickness residual stress distribution

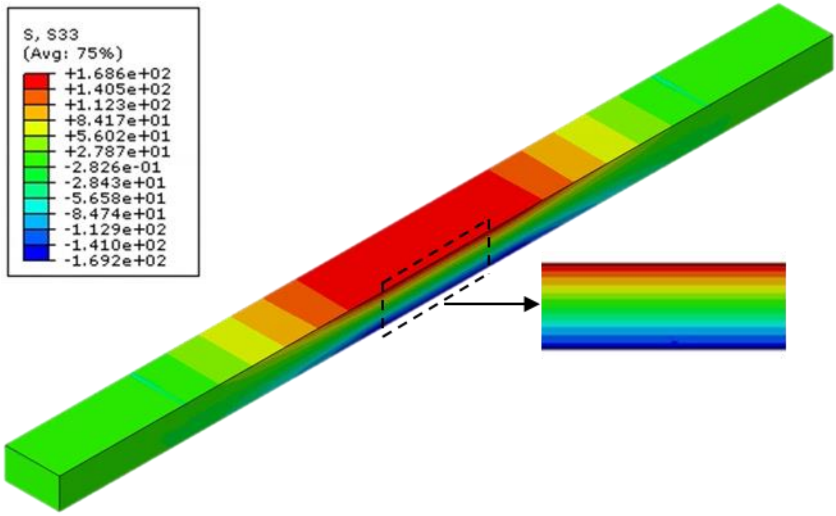

Figure. 5.2. Simulated through-thickness stress distribution by four-point bending of 4 mm C1220

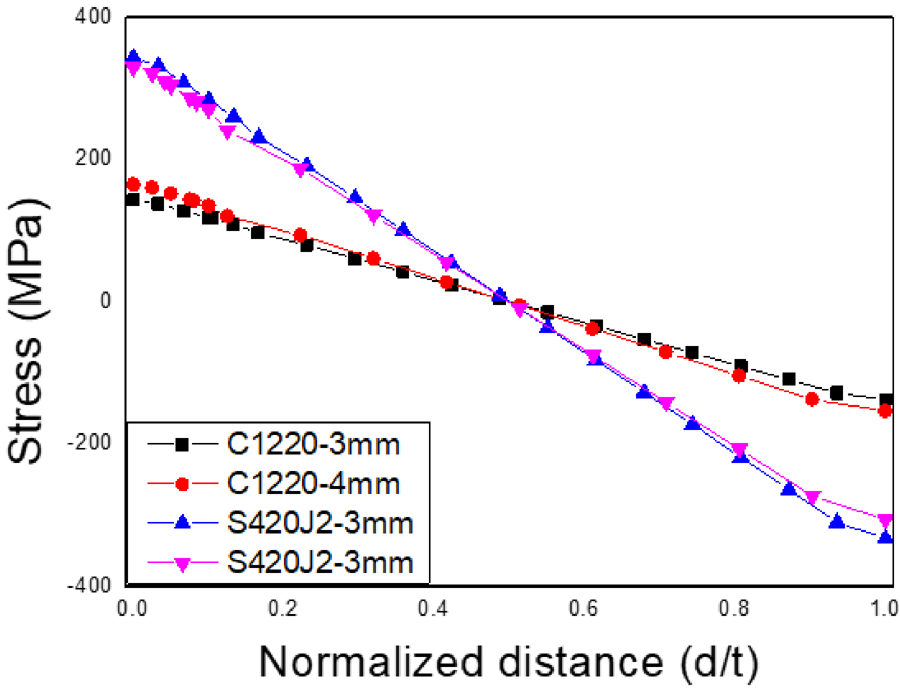

Figure. 5.3. Through-thickness stress distribution with distance normalized by thickness of specimen

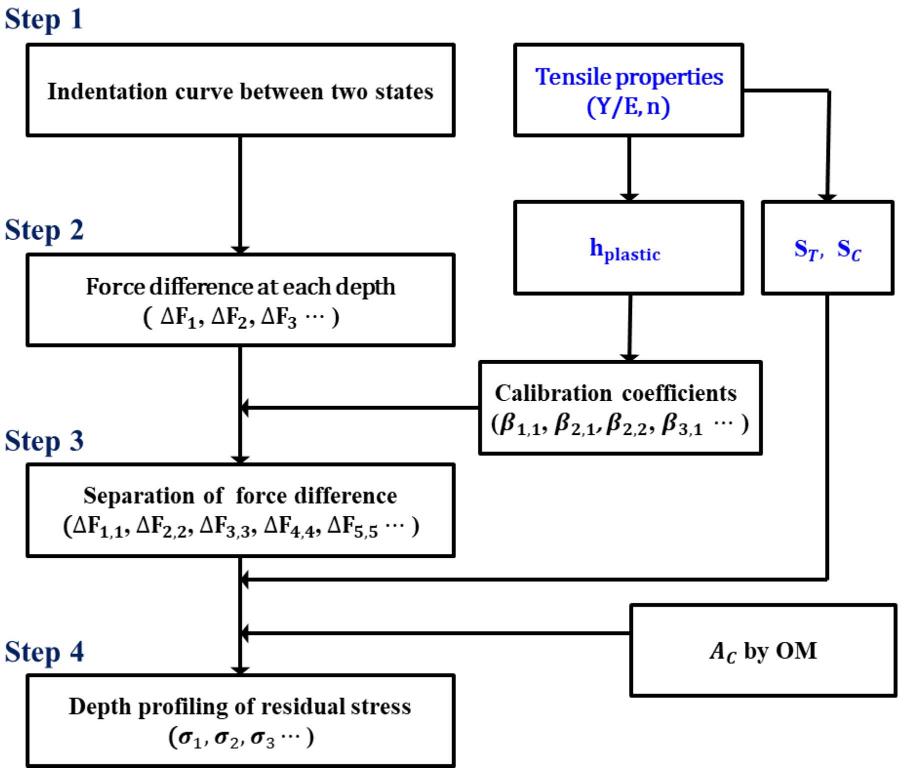

Figure. 5.4. Flow chart of through-thickness residual stress evaluation

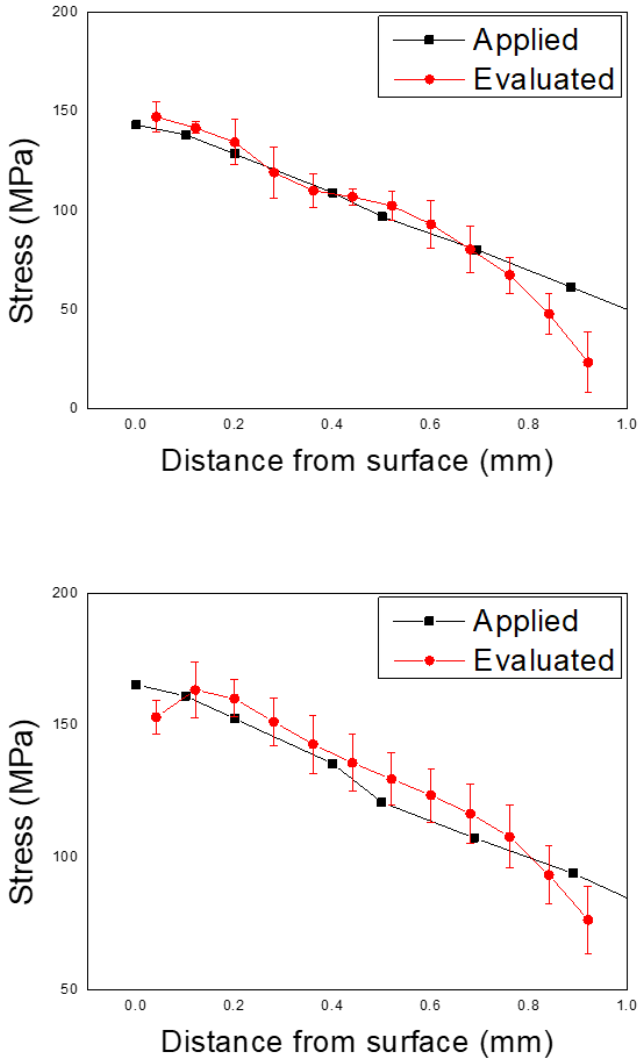

Figure. 5.5 Comparison of bending stress measured by IIT and FEA for C1220 specimen with thickness of (a) 3 mm (b) 4 mm

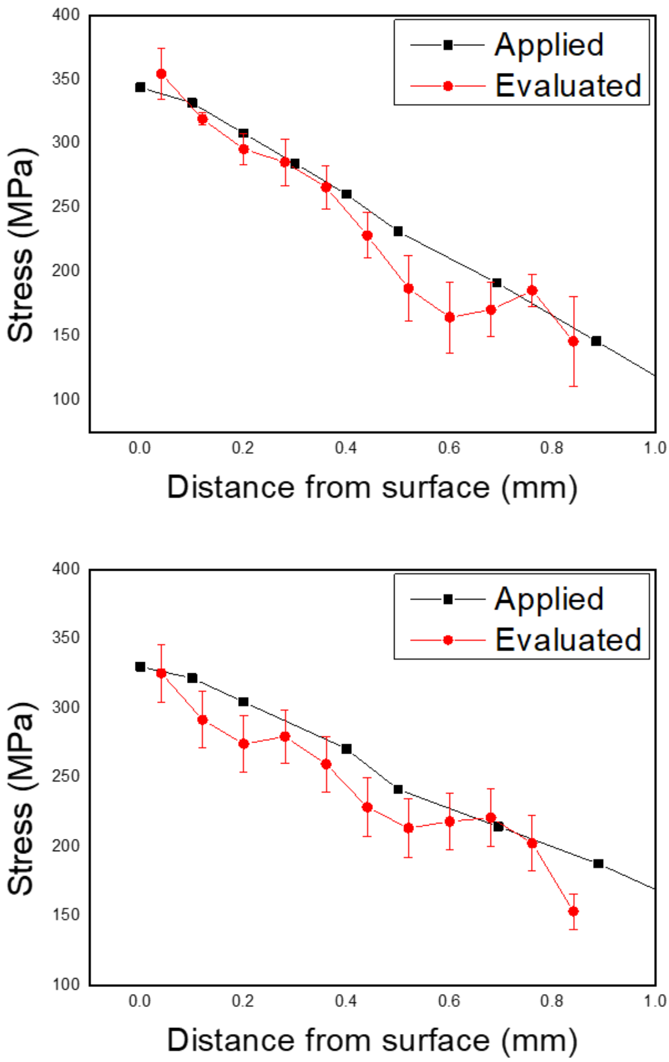

Figure. 5.6 Comparison of bending stress measured by IIT and FEA for S420J2 specimen with thickness of (a) 3 mm (b) 4 mm

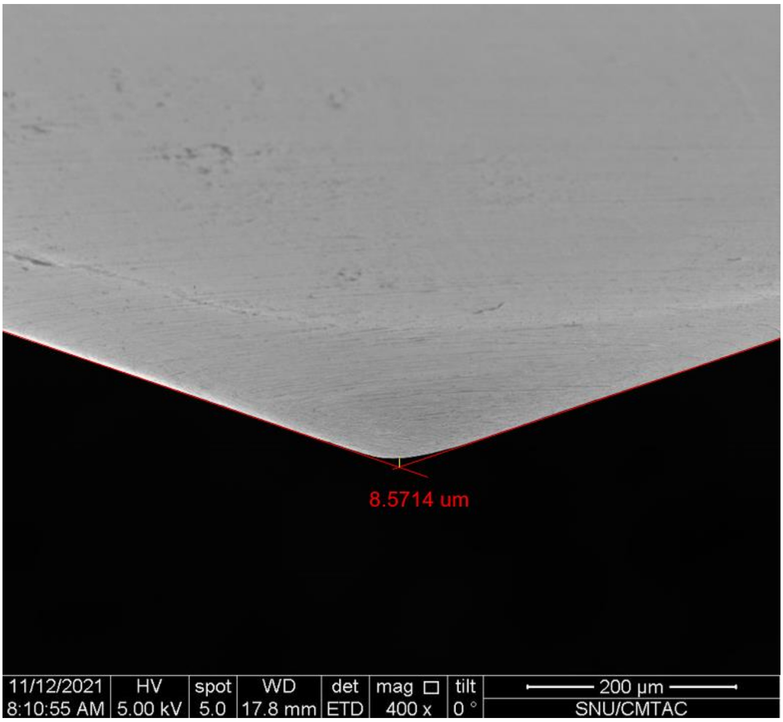

Figure. 5.7 SEM image of conical indenter tip used for verification test

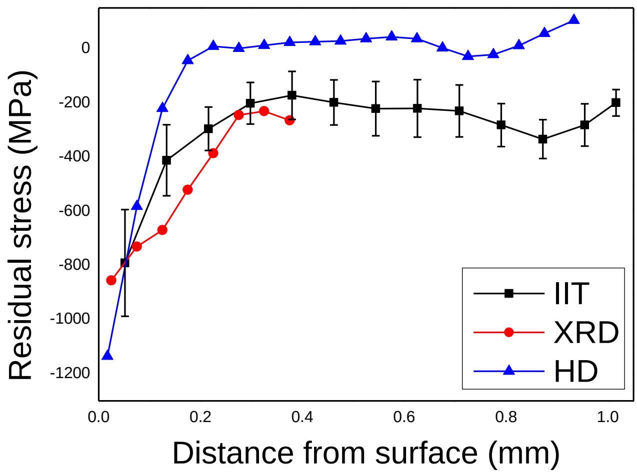

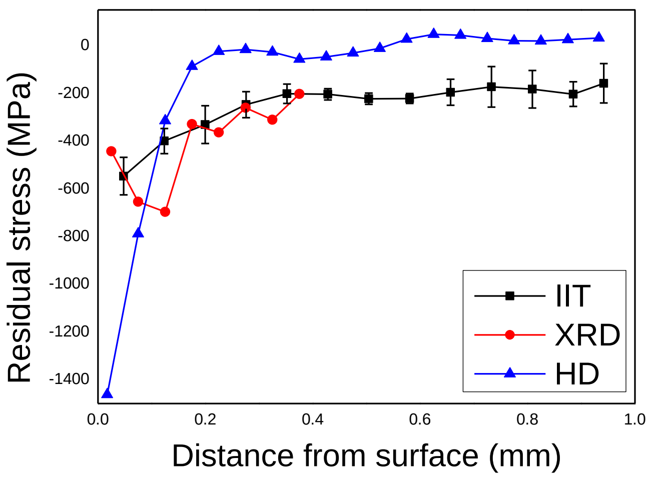

Figure. 5.8 Comparison of peening stress distribution measured by hole-drilling, XRD and indentation methods for (a) SUS303 and (b) SUS316

References

[1] A. E8, Standard Test Methods for Tension Testing of Metallic Materials, 2016.

[2] E.I. 14577-1:, Metallic Materials–Instrumented Indentation Test for Hardness and Materials Parameters–Part 1: Test Method, Polish Committee for Standarization Warsow, Poland, 2013.

[3] G.S. Schajer, Hole-Drilling Residual Stress Profiling With Automated Smoothing, Journal of Engineering Materials and Technology 129(3) (2007) 440-445.

[4] M.B. Prime, R.J. Sebring, J.M. Edwards, D.J. Hughes, P.J. Webster, Laser surface-contouring and spline data-smoothing for residual stress measurement, Experimental Mechanics 44(2) (2004) 176-184.

[5] M.D. Olson, A.T. DeWald, M.B. Prime, M.R. Hill, Estimation of uncertainty for contour method residual stress measurements, Experimental Mechanics 55(3) (2015) 577-585.

[6] G.S. Schajer, Practical residual stress measurement methods, John Wiley & Sons2013.

[7] M.K. Khan, M.E. Fitzpatrick, S.V. Hainsworth, A.D. Evans, L. Edwards, Application of synchrotron X-ray diffraction and nanoindentation for the determination of residual stress fields around scratches, Acta Materialia 59(20) (2011) 7508-7520.

Chapter 6

CONCLUSION

In this study, evaluation method of through-thickness distributing residual stress using instrumented indentation testing with conical indenter was proposed. Finite element analysis was used for developing the step-wise constant stress distribution to measure the force difference generated by layer stress. The maximum stress sensing depth, the depth that influences the indentation force-displacement curve depending on the presence of stress, was estimated by analyzing the variation of force differences by indentation displacement with increasing the stressed depth. Calibration coefficients, the contribution of each layer stress on total force difference, were obtained from cumulative force difference-stressed depth curve. Theoretical modeling for depth-profiling of stress was performed using the calibration coefficients, which can be applicable regardless of indentation displacement based on the geometrical self-similarity of sharp indenter.

Improvement of conventional model for stress magnitude evaluation and generalization of calibration coefficients were carried out in the consideration of mechanical property effect based on dimensional analysis for accurate stress depth profiling. The correcting slopes, ratio of real residual stress and evaluated stress using indentation method, can be estimated by using the information of yield strain and strain hardening exponents, resulting in the significant improvement of evaluated stress accuracy. The maximum sensing depths of material, determining the depth where the evaluated stress exists, are identified to be related with the depth of plastic zone. Dimensional analysis for depth of plastic zone was carried out in the same ways applied to correcting slope.

Computational and experimental verifications were performed with materials of various mechanical properties and through-thickness stress distribution. The verification results reflecting the improvement for conventional model and generalized calibration coefficients were matched well with reference stress distribution which were obtained from finite element analysis and other stress measurement methods. This model facilitates quantitative evaluation of through-thickness residual stress with low damage on target materials, which can be applied to in-service components. Determination of directionality and principle direction of the stress through the thickness can be considered to be available in combination with digital image correlation.

초 록

잔류응력은 외부에서 가해지는 응력이나 하중의 원인을 제거한 후에도 재료에 남아있는 응력을 의미한다. 이는 제조 공정이나 열처리 과정에서 생긴 재료의 불균일한 소성변형과 밀도 및 미세조직의 변화에 의해 발생하며, 재료의 연속성을 유지하기 위해 생기는 탄성 변형의 결과물이다. 잔류응력은 재료의 피로 수명 및 균열 저항성에 영향을 미치므로 정밀한 제어 및 측정이 필요한 중요한 요소로 간주된다. 균열 저항성 향상을 위해 부품 표면부에 압축잔류응력을 인가할 수 있는 다양한 표면처리 및 용접 기술이 발달 하고 있으나, 인가된 잔류응력-깊이 분포를 측정 방식은 제한적이다.

잔류응력-깊이 분포의 측정이 가능한 방식은 파괴적으로 재료의 일부를 제거하여 회복되는 탄성 변형을 측정하는 응력 완화 방식이 주로 활용 되고 있다. 대표적인 예로, hole-drilling method는 재료 표면에 원기둥 현태의 구멍을 만들면서 미리 계산된 표면의 변형률과 구멍 깊이의 관계를 활용하여 깊이 별 응력을 측정한다. Slitting method와 contour method는 부품 절단과정에서 발생한 표면 변형 혹은 변위를 측정하는 방식으로 이뤄져, 가동 중이거나 예정인 부품을 대상으로 활용성이 떨어진다. 비파괴적인 방식인 X-ray

회절법의 경우, 침투 가능 깊이가 대부분의 금속의 경우 100 μm를 넘지 않기 때문에 깊이 별 측정을 위해 파괴적인 방식과 조합되어야 한다. Neutron이나 synchrotron 회절법을 활용할 경우, 침투 깊이가 수 cm정도로 깊이-응력 분포 측정이 가능하나, 낮은 접근성 때문에 사용자들에게 널리 활용되기에 어려움이 있다. 따라서, 부품에 손상을 줄이면서 깊이 별 잔류응력 분포의 측정이 가능한 방식의 개발이 필요하다.

계장화 압입시험은 잔류응력 존재 유무에 따른 힘-변위 곡선의 변화를 통해 잔류응력을 측정할 수 있는 방식으로 활발히 연구되고 있다. 기존에 Vickers, Berkovich, 원뿔 압입자를 활용한 평균 잔류응력의 평가 모델이 개발되어 있으며, Knoop, modified Berkovich 압입자나 디지털 이미지 상관 (DIC) 방법을 활용하여 표면 잔류응력의 방향성 및 주응력 방향의 평가 방식이 제안되어 있다. 압입시험은 최대 압입 변위를 조절하여 실험 후 대상 부품에 남게 되는 손상 정도를 제어할 수 있어 준비파괴적인 방법으로 활발히 연구되고 있다. 하지만, 압입시험을 통해 측정된 잔류응력이 응력이 어느 깊이의 응력을 대표하는지에 대한 연구가 부족한 상태이며, 불균일한 응력분포 하에 압입 힘-변위 곡선의 변화를 통한 깊이 별 잔류응력의 평가 방식은 연구된 바가 없다.

본 연구에서는, 입입시험을 통해 측정한 잔류응력의 분포 깊이를 확인하였으며, 불균일한 잔류응력 분포에서 깊이 별 잔류응력 평가 방식을 제안하였다. 깊이 별 잔류응력을 단계함수 형태로 제어하기 위하여 유한요소해석의 경계조건과 열응력이 활용되었으며, 원뿔 압입자의 기하학적 자기유사성을 기반으로 변위에 상관없이 활용 가능한 “누적 압입 힘의 차이-응력깊이” 곡선을 제안하였다. 깊이 별 잔류응력의 전체 힘의 차이에 대한 기여도를 나타내는 보정 계수가 제안되어 연속적인 압입 곡선을 활용한 표면으로부터 거리에 따른 응력 분포를 측정할 수 있는 모델이 제안되었다.

압입시험은 탄소성 변형이 수반되는 시험 방식이므로, 정확한 깊이-응력 측정을 위해 제안된 모델을 통해 얻은 응력 값과 깊이는 재료의 기계적 물성에 따라 보정 되어야 한다. 본 연구에서는 기존의 잔류응력 크기 평가 모델의 개선과 새로 제안된 깊이-응력 측정 모델을 재료의 기계적 물성을 고려하여 최적화를 위한 모델이 차원해석을 기반으로 제안되었다. 압입시험에 의한 소성역의 깊이와 임계 깊이 간의 관계 확인을 통해 보정계수를 일반화하고 측정된 응력의 깊이를 기계적 물성에 따라 보정하는 모델이 제안되었다. 제안된 모델을 유한요소 해석과 실험을 통해 다양한 기계적 물성의 재료 및 응력 상태에서 검증하였다.